UNIVERSITÁ DEGLI STUDI DI NAPOLI FEDERICO II

Dottorato di ricerca in
Ingegneria Aerospaziale, Navale e della Qualità (XXIV Ciclo)

Canditate
Stefania Stefani

Ph.D. Thesis

Optical properties of gases under planetary conditions: measurements and models

Tutor: Prof. Pasquale Palumbo
Co-Tutor: Dr. Giuseppe Piccioni

PhD Coordinator: Ing. Antonio Moccia

Anno Accademico 2010-2011

Contents

Introduction

This work has been completely carried out in the Planetary Laboratory (PLab) of the Istituto di Astrofisica Spaziale e Fisica cosmica (Cosmic Physics and Space Astrophysics Institute) of the Istituto Nazionale di AstroFisica (Italian National Institute for Astrophysics) of Rome. The scientific goals related to this thesis work are two: implement spectroscopic databases and support the space missions.

Presently a wealth of spectroscopic data are present in several databases, such as HIgh-resolution- TRANsmission (HITRAN [1]), HIgh-TEMPerature (HITEMP) [2] Carbon-Dioxide-Spectroscopy-Databank (CDSD [3]). They provides a suite of parameters of molecular species at typically terrestrial conditions and are routinely used for the retrieval of many parameters concerning the atmosphere of the Earth. On the other hand, they not or contain very limited information on the behavior of gases at extreme conditions, in particular, high pressure and high temperature. These parameters are of major importance for the radiative transfer models of data coming from space mission, such VIRTIS (Visible and InfraRed Thermal Imaging Spectrometer) instrument on board the ESA mission Venus Express [4]. The VIRTIS instrument provides hyperspectral images of Venus, in the spectral range from 0.3 to 5.1 micron. The interpretation of these observations requires sophisticated radiative transfer calculations, based on the spectroscopic knowledge available for

the main absorber, carbon dioxide. In fact, Venus' atmosphere, for instance, is much hotter and denser than the Earth's, and temperatures up to 450°C and pressures up to 92 bar at the surface have to be considered. The composition is also very different, being constituted almost entirely of carbon dioxide (97 %). The CO_2 is a strong absorber in the infrared and near infrared part of the spectrum, and the observation from orbit down to the surface is only possible in the so-called "transparency windows" in between the strong absorption bands. Despite these needs, till this moment, accurate experimental and theoretical data for the absorption by carbon dioxide at high pressure was still missing. For example, in the work [5], in order to determine the volume mixing ratio profiles of several species in Venus atmosphere from spectra recorded by VIRTIS instrument, a constant was used for the CO_2 continuum through a wide spectral range.

Laboratory studies of high pressure carbon dioxide absorption are complicated by different phenomena. Firstly, the widely used Lorentzian line shape strongly overestimates the absorption in the band wing regions, while it underestimates the absorption near band centers at elevated pressure. The second difficulty is linked to absorption due to the transient dipole moment induced during collisions and/or due to dimers [or larger $(CO_2)_N$ clusters] formed in the dense gas. The deviation of the measured absorption (due to the 3 permanent dipolar moment) with respect to the Lorentz shape at high pressure is essentially due to collision-induced intensity transfer between transitions (line-mixing effects) and to the finite duration of intermolecular collisions. Several laboratory experimental and theoretical studies were devoted to high pressure allowed spectra of pure CO_2 [6]- [7]. They all point out the strong discrepancy between the Lorentzian profile and experimental spectra for the studied spectral region.

Thank to the thesis work, numerous data at several temperature, from 294 to 600 K, and pressures, from 1 up to 30 bar, are now available.

This thesis is organized as following: in chapter 1 a brief description of the remote sensing technique and instrumentation employed are reported. You can find also an extensive analysis of the VIRTIS spectrometer, which has recorded many images and spectra of the Venus atmosphere since its orbital insertion, on April 11 2006.

The characteristics of the twin planet of the Earth for dimensions and mass, but from the behavior a lot different, will be given in chapter 2. Some notions of spectroscopy, that gives us a remote access to most of the important information carried by the radiation which directly interact with the planet, will be introduced in the second part.

The CO_2 absorption coefficients have been measured by a Fourier Transform InfraRed (FT-IR) interferometer integrated with a special gas cell. Thanks to this experimental set-up we can cover a wide spectral range, from 750 to 25000 cm^{-1} (0.4-29 μm), with a relatively high spectra resolution, from 10 to 0.07 cm^{-1}. Indeed, the gas cell is designed to support pressure up to 350 bar and temperature up to 650K. A detailed description is reported in the chapter 3.

The measurements have been compared with synthetic spectra obtained using three different models: one implementing a line by line calculation; the second one taking into account the line mixing effect in the strong collision approximation and the last one using a different approach to the line mixing effect. A discussion about this theoretical model is reported in the chapter 4.

Finally, in the last chapter (5) a detailed discussion on the measurements obtained using a real vertical venusian profile and the comparison between data and simulations are reported.

Chapter 1

Remote Sensing data analysis and instrumentation employed

Undoubtedly, much of what we know about the Solar System comes from direct exploration. Since the early 1960's, many robotic spacecrafts have been sent out into our Solar System to explore and return knowledge and images of distant worlds. Instrumented probes have descended through the atmosphere of Venus and Mars. The Mariner, Pioneer, Venera, Viking and Voyager space flight programs have provided opportunities to study the planets from Mercury to Neptune and most of their satellites. During this space age, missions of exploration into all the Solar System have revolutionized our view about the nature of it. Today, we are only at the beginning of this exploration, and even if we have some information, misunderstandings of many physical phenomena involved are still innumerable. Remote sensing investigations have been conduced with unprecedented spatial and spectral resolution, permitting detailed examinations of atmospheres and surfaces. Even for the Earth, space-borne observations, obtained with global coverage and high spatial, spectral

and temporal resolution, have revolutionized weather forecasting, climate research and exploration of the natural resources.

The collective study of the various atmospheres and surface in the Solar System constitutes the field of comparative planetology. Wide ranges in surface gravity, solar flux, internal heat, obliquity, rotation rate, mass and composition provide a broad spectrum of boundary conditions for atmospheric systems. Analysis of data within this context lead to an understanding of physical processes applicable to all planets. Once the general physical principles are identified, the evolution of planetary system can be explored. Some of the data needed to address the boarder questions have already been collected. Infrared spectra, images and many other types of data are available in varying amounts for Mercury, Venus, Earth, Mars, Jupiter, Saturn, Uranus, Neptune and many of their satellites. It in now appropriate to review and assess the techniques used in obtaining the existing information. This will not only provide a summary of our present capabilities, but will also suggest ways of extending our knowledge to better address the issues of comparative planetology and Solar System evolution.

The purpose of this chapter is to describe some characteristic of the remote sensing technique and of the instrumentations employed.

1.1 Introduction to the remote sensing technique

The *remote sensing technique*, also called *remote sounding*, employs electromagnetic radiation reflected, scattered or emitted from the planets or earth atmosphere at a distance from the observing station. This technique is a powerful tool for investigating the atmospheric structure and composition or surface [8].

We can distinguish:

- active remote sensing: which employs a transmitter at the observing site (see figure 1.1)
- passive remote sensing: which relies on the radiation emitted from the atmosphere or on solar radiation scattered or reflected by towards the observer (see figure 1.1).

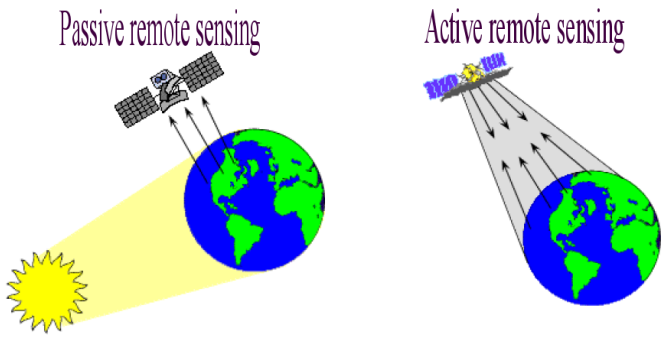

Figure 1.1: *Schematic picture to show the two different remote sensing techniques*

The radiation from earth or planets atmosphere system reaches an orbiting satellite over a wide spectral range. In the UV, visible and near-IR range (typically, wavelength below 4 μm) solar radiation is scattered and reflected from the surface, from the clouds, from the aerosol[1] and from the molecules. The planetary spectrum corresponds to the reflected solar black-body, peaking at 0.5 μm, over which planetary absorption features can be observed. These signatures allow us to determine the nature and the column density [2] of the different atmospheric constituents, the clouds, the aerosol and the characteristics of the surface, if any. In the infrared and microwaves regions, radiation is emitted from the surface, clouds and molecules. In

[1] small particles suspended in the atmosphere
[2] the number of molecules integrated along the line of sight

this case, the planetary spectrum corresponds to its thermal emission. Its maximum depends upon the effective temperature of the planet and it can give information on surface and atmospheric temperature profile. Over this wide range of wavelengths a great deal of information is contained about the surface and composition of the atmosphere below.

The first examples of the remote sounding are those of the structure and composition of the high atmosphere made by observer on the ground. It was observations of meteor trails by Lindemann and Dobson in 1923 which first demonstrated the high temperature near the stratopause. Observations of the ultraviolet light scattered from the sky by Dobson in 1926 which provided the first measurements of stratospheric ozone and its distribution with height.

A revolution to this technique began with the development of space satellite. In fact the great advantage of a satellite as a measurement platform is that it provides observations over a very large area in a short time. For example, from a satellite in geostationary orbit, continuous observation of about a quarter of the atmosphere is possible. A satellite in near-polar orbit makes about 14 orbits for day and can view all parts of the atmosphere at least twice for day.

Interpretation of these remote sounding observations is often complex and difficult, but they possess the great advantage, compared with conventional and in situ observations, that a satellite can provide observations over a large area and in a short time. The first weather satellite was lunched in 1960 and carried television cameras for viewing clouds. For the first time complete pictures were seen of the patterns of clouds associated with large weather systems. Such information is now produced from large number of satellites and provides valuable information for short range weather forecasting.

Detailed cloud pictures of Mars, Venus and Jupiter from space probe have also provided a surprisingly large amount of information about the circulation of their atmosphere.

In order to create images of the planet or earth from satellite instruments it is convenient to employ simple scanning systems that use the motion of satellite itself to perform some of the scanning. Generally, in front of a telescope, which focuses radiation onto detectors sensitive to different wavelength, a rotating mirror is mounted at 45° to its axis of rotation (refer to figure 1.3 in section 1.2).This scans continuously across the direction of the satellite motion. As the satellite and the swath of observation moves forward images of different parts of the spectrum are generated. Most geostationary satellites for meteorological observation are spin-stabilized with the axis of spin parallel to the earth's axis. They carry imaging instruments called *spin-scan cameras*. Scanning in longitude is achieved by the satellite's spin, a tilting mirror at the front of the instrument arranges for scanning in latitude. In these instruments, channels sensitive to visible radiation create images of sunlight reflected from the planet and its atmosphere. Images of radiation in the infrared emitted by the surface or the atmosphere also provide important information. The most obvious information of this kind is the temperature of the planet's surface or the cloud top below the satellite. In atmospheric windows [3], the radiance received correspond quite closely to the Planck black body function at the surface or cloud top temperature. By combining measurements at different wavelengths at which the properties of the surface or of the clouds differ slightly, more detailed information can be retrieved. Measurements at higher spectral resolution in the infrared or microwave spectral range, provide more precise information about the atmosphere's

[3]The regions of the electromagnetic spectrum that are relatively free from the effects of atmospheric attenuation.

temperature structure and composition.

Given knowledge of the atmospheric temperature provide from remote observations on the bands of carbon dioxe or oxygen, observations of the spectrum of radiance from other emitting gases can provide information about their atmospheric distribution. Of especial importance is the distribution of the water vapour, information about which is available from both infrared and microwave emission bands.

To study the optical properties of minor constituents that are present in small concentration, one can observe the radiation emitted from the atmosphere in the limb configuration. This provides a long absorbing path or a long emitting path against the cold background of space. A schematic presentation of this configuration is shown in figure 1.2

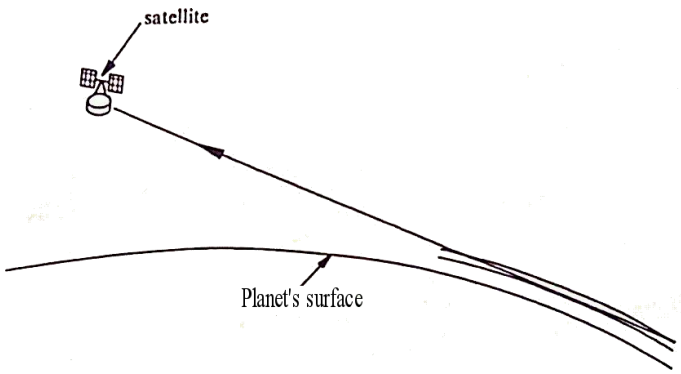

Figure 1.2: *Limb sounding of the planet's atmosphere. Measurements of the emission from the atmosphere's limb have the advantages of a very long emitting path so that constituents present in very small concentrations can be studied and near-zero radiation background beyond the limb.*

1.2 Remote sensing instruments

Instruments designed to measure infrared radiation are called radiometers, photometers or photopolarimeters [9]. The term spectrometer refer to a class of instruments

which measure the intensity as a continuous function of wavenumber or wavelenght; if they generate a two-dimensional display of the radiation field, they are called imaging systems or cameras. However, there is not fundamental difference between radiometers, spectrometers or cameras; in fact all radiometric instruments must have detectors, that is, elements that absorb infrared radiation and convert it to another form of energy, which can then be recorded by electronics means. In general, radiometric instruments include optical components to focus radiation from planetary area onto one or several detectors and circuitry to amplify/record the signal. In addition, choppers, shutters, scanning mirrors, image motion compensators, calibration sources and other components may also be part of fully functional remote sensing device. Each task-imaging, spectral separation and detection- can be implemented by a lot of techniques. For example, to create the image of the planet from satellite it's convenient to employ simple scanning systems that generally use the motion of the satellite itself. Besides the scientific requirements, physical size, weight, power consumption, cryogenic demands, data rates and others often sub-requirements set further boundaries to the design. The essential elements of an infrared radiometer with which to make radiance measurements for remote sensing are illustrated in figure 1.3. They are a telescope to focus the radiation into a detector, a filter to isolate the spectral region required, a means to calibrate the instrument with observations of space away from the earth and with observations of a black body at known temperature. A mechanical chopper may be added to interrupt rapidly the incoming signal so that it can be more easily amplified and effective signal to noise increased. For an instrument operating at microwave frequencies the elements are essentially the same with the differences that the fine spectral filtering is electronic rather than optical.

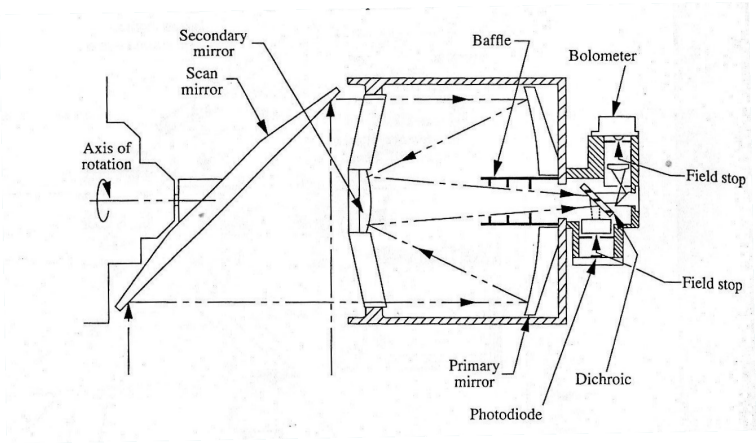

Figure 1.3: *Optical schematic of a typical radiometer, showing the elements of a simple filter, a telescope and two spectral channels separated by a dichroic plate. This configuration include also a scan mirror which can be pointed at the atmosphere, cold space or a black body at known temperature for calibration purposes.*

An instrument which collects radiant energy in a particularly efficient way while at the same time achieving high spectral resolution is the Michelson Interferometer (see figure 1.4).

The essential part of the instrument is the beamsplitter, which divides the incoming radiation into two beams of nearly equal intensity [9]. After reflection from the stationary and movable mirrors, the beams recombins at the beamsplitter. The phase difference between both beams is proportional to their optical path difference, including a phase shift due to the difference between internal and external reflections at the beamsplitter. Suppose a collimated beam of monochromatic radiation strikes the interferometer while the movable mirror is set at the balanced position where both arms have equal length. In a non-absorbing beamsplitter the phase difference between internal and external reflection is 180°. Consequently, both beams interfere destructively as seen from the detector, the central fringe is dark. At the same time, the interference is constructive as seen from the entrance port. The incom-

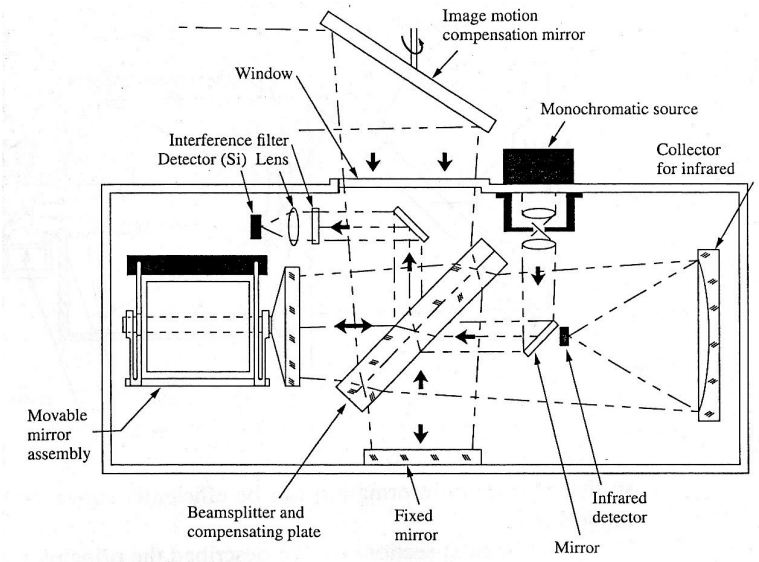

Figure 1.4: *Optical schematic of infrared interferometer, showing the servo-controlled moving mirror drive and the secondary interferometer receiving light from a monochromatic source for reference purposes.*

ing energy is reflected back towards the source, the interferometer acts as mirror. Now suppose the moveable mirror is displaced by a quarter of a wavelength. The phase of the beamsplitter from that mirror changes by half a wavelength or 180°. Detector and source sides experience now constructive and destructive interference respectively. The interferometer as a whole becomes transparent at that wavelength and incoming radiation strikes the detector. The interferometer may be viewed as a sinusoidal modulator, which alternately switches the arriving beam between detector and source, depending on the position of the movable mirror. Emission from the detector experiences the same fate, since the interferometer is symmetric as far as source and detector are concerned. Michelson interferometers can operate in two different modes. In one mode the movable mirror, sometime called *Michelson mirror*, is stepped in small, equal increments. Sampling theory requires an optical step size of less than one half of the shortest wavelength to be measured, otherwise

aliasing may occur. However, if we know that the signal consists only of a narrow band of frequencies, sampling may occur at larger intervals without risking confusion due to aliasing. the number of sampling points can be reduced considerably by this technique. Alternatively, in a method sometime employed in the continuous mode, the interferometer may be oversampled and the reduction to the minimum number of necessary data points may be accomplished by numerically filtering after digitalization. In the stepping mode, the signal is integrated at each rest position for a certain time, the dwell time. After that, the Michelson mirror moves to the following position and the next point is recorded. In the continuous mode the mirror advances at constant speed and the signal is sampled at small, equal intervals. At one time the misconception existed that this mode is less efficient than the discrete step mode because the time spent in taking the sample is small in comparison with the time between sample, but this is not the case. Integration between samples takes place in the electrical filter used to limit the frequency range before the sampling process. On the contrary, the stepping mode is slightly less efficient, because the time spent while moving the mirror between measurement points is loss.

As the whole spectrum is observed all the time, the Michelson Interferometer possesses what is called the *multiplex* advantage; observation from many spectral channels can be made simultaneously.

In the case of planetary atmospheres, the radiation measured by the instrumentation on board of spacescraft, consists of many spectral line and radiation continuum. To resolve each single line it's convenient to use a *grating spectrometer*. The diffraction grating is of considerable importance in spectroscopy, due to its ability to separate (disperse) polychromatic light into its constituent monochromatic components. A grating consists of a series of equally separated, parallel slits or apertures, the width

of each being comparable to the wavelength of radiation to be separated. It may be thought of as a collection of diffracting elements, such as a pattern of transparent slits in an opaque screen, or a collection of reflecting grooves on a substrate (also called a blank). The slits may be supported on a material which transmits or reflects the radiation and the grating is then called a transmission or a reflection grating, respectively. The fundamental physical characteristic of a diffraction grating is the spatial modulation of the refractive index. If a beam of radiation, such as white light in the visible region, falls normally on to the surface of a reflection grating, as shown in fig 1.5, the radiation is dispersed and reflected [10]. In the dispersion process there is not just one spectrum produced, as with a prism for example, but several. There are two spectra, each extending from red to violet, produced for each order of diffraction by the grating, one on each side the normal. The resolving power

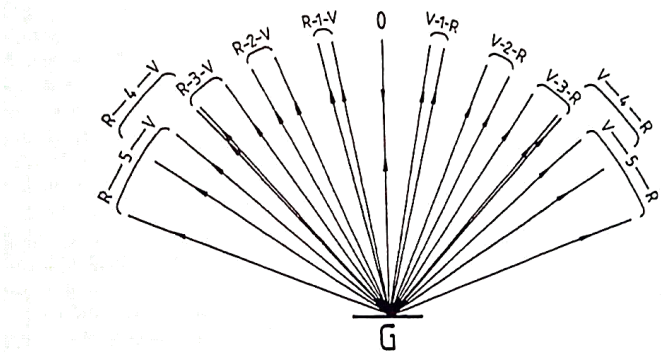

Figure 1.5: *Dispersion by a reflection grating*

is function of the total number N of grooves and can be achieved in practice only if the beam of radiation covers all the groves, otherwise N is effectively reduced. For high resolving power, we require N to be large and it is unaffected by having the grooves closely spaced on a small grating or widely spaced on a large grating. Other considerations, however, make a small grating preferable. The first is that the angular dispersion, increases as the separation of adjacent grooves d decreases and it

is no good having a grating with high resolving power if the dispersion is so low that the detector is unable to distinguish wavelengths which the grating has resolved. The second consideration favouring a small grating is that a large on required large lens, large mirrors and so on in order to fill it with radiation and this again increases the size of the instrument.

The possible modes to illuminating a grating and gathering the light reflected from it, not only in the far infrared but also in the mid and near infrared, visible and violet regions, are numerous. The most famuose configuration is the Ebert-Fasties mounting, as shown in figure 1.6. Radiation from the source S enters the spectrometer at the slit S_1 which is separeted from the mirror M by its focal lenght f so that the grating G recevies a parallel beam from M. The grating reflects and desperses the radiation which is focused by M on to the slit S_2 and pass to the detector D. The required wavenumber range is scanned across S_2 by smooth rotation of the grating. An important property of this configuration is that the aberrations produced by using the mirror off-axis at the first reflection are cancelled by the aberration on the second reflection.

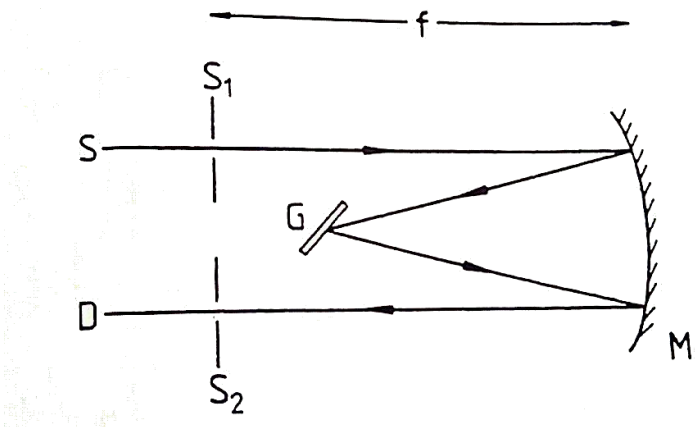

Figure 1.6: *The Ebert-Fastie mounting of a diffraction grating.*

A sophisticated spectrometer designed to collect images and spectroscopic data of the Venus's atmosphere is VIRTIS. The acronym stands for Visible and InfraRed Thermal Imaging Spectrometer and is an instrument which covers the wavelength range from 0.3 to 5 μm. In the section 1.4, you can find a detailed description of this instrument on board of the European Space Agengy (ESA) Venus Express mission (VEX).

1.3 Radiative transfer processes

Various physical processes modify a radiation field as it propagates through an atmosphere. The rate at which the atmosphere emits depends on its composition and thermal structure, while its absorption and scattering properties are defined by the pravailing molecular opacity and cloud staructure.

To describe the extinction of a beam of radiation crossing a homogeneous atmospheric layer dl with an incidence angle $\cos\theta$, we defined the optical depth. Once divided for $\cos\theta$, this quantity can be interpreted as the average number of interactions with matter of a photon with wavenumber ν crossing the depth dl. The expression for a single uniform gas cell of length dl is:

$$d\tau_\nu = k_\nu^l(l)q(l)dl \tag{1.1}$$

In formula, optical depth is the integral of k_ν^l times the mixing ratio [4] q(l) along the vertical axis or the line of sight depending on the particular consideration. One of the main assumptions in atmospheric science is to consider for sake of simplicity the

[4]The mixing ratio is the molar concentration over the total amount of atmospheric gas for each point. It is defined as the ratio between the number of molecules of the generic gas and the total number of molecules of all the atmosphere.

atmosphere as composed of a finite number of plane and parallel layers each with uniform temperature and pressure in its interior.

At the radiation crossing between the levels $l_0 = 0$ and $l_1 = z_1$ is associated an optical depth of:

$$\tau_\nu = \int_{l_0}^{l_1} k_\nu^l(l) q(l) dl \tag{1.2}$$

Therefore optical depth is the integral calculated along the line of sight of absorption coefficient k_ν^l multiplied by the mixing ratio q(l). In our case, the optical path is equal to the length of the gas cell, i.e. 2 cm.

It is now possible to calculate the attenuation of the radiation. Transmittance, along the line of sight, is simply the exponent of the optical depth:

$$t_\nu = exp - \left(\frac{\tau_\nu}{\cos\theta}\right) \tag{1.3}$$

In the solar region, we often deal with the total transmittance of the atmosphere from the space to the surface and back:

$$t_\nu = exp - \left[\tau_\nu \left(\frac{1}{\cos\theta_0} + \frac{1}{\cos\theta}\right)\right] \tag{1.4}$$

where τ_ν is the total optical depth in the nadir (strictly vertical) direction, θ_0 is the sun zenith angle and θ is the line of sight zenith angle.

For the pourpuse of this work, we consider only the case of the **radiative Ttransfer without scattering**, i.e. whene the effect of aerosols is negligible. The Radiative Transfer Equation is calculated as the integral of the Planck function on transmittance (which depends on altitude) from the bottom level (or a reference altitude) to the top of the atmosphere, plus an additional term taking into account the surface

emission.

A nadir viewing instrument would see the upward monochromatic radiation intensity as:

$$I_\nu = \epsilon_\nu B_\nu(T_0) t_{\nu,0} + \int_0^{t_0} B_\nu(T(\tau_\nu)) dt_\nu \tag{1.5}$$

This expression can be seen as composed by two terms: the emission from the bottom level (surface or equivalent altitude) ϵ_ν, attenuated by all the layers above it (first term) and the total contribution of all the other layers (second term). The integral over the transmittance of all the atmosphere, means that every layer emits thermal radiation absorbed by all the overlying layers. In the near infrared, where the solar radiation dominates, the radiance is simply the solar radiation flux F_ν^0 outside the atmosphere (divided by π) times total atmosphere transmission, with account for the surface albedo a_ν.

$$I_\nu = \frac{F_\nu^0 \cos\theta}{\pi} a_\nu exp - \left[\tau_\nu \left(\frac{1}{\cos\theta_0} + \frac{1}{\cos\theta}\right)\right] \tag{1.6}$$

In principle, it is possible to obtain the atmospheric outgoing radiation from the direct integration of the previous relations if the thermal and the species concentration profiles as function of altitude are known.

For completeness, it should be remembered that in the presence of aerosols, have some added terms due to: the contribute to the field of the photons which are emitted at the surface in any direction and then send towards the observer after a single interaction with the particles. The contribute of photons which went towards multiple scattering events or diffusion of photons emitted by the atmosphere. These inputs contain the intensity of the field, whose presence in both the left and right terms of the radiative transport equation makes impossible to achieve an analytic

solution of equation 1.3.

1.4 The Visible and InfraRed Thermal Imaging Spectrometer

The Visible and InfraRed Thermal Imaging Spectrometer (VIRTIS) is a complex instrument developed for remote sensing study of Venus atmosphere at wavelengths from 0.3 to 5 μm. It is an imaging spectrometer that combines three data channels in one compact instrument:

- a mapping channel, VIRTIS M (named -M), which provides images at multiple wavelengths in the band 0.25-5 μm. It comprises two channels which are committed to spectral mapping and are housed in the Mapper (-M) optical subsystem. One frame records a spectral image in one dimension, while the second dimension is obtained through a scanning mirror. One channel is devoted to acquire infrared radiation in the range 1-5 μm while the other observes the visible radiance from 0.3 to 1 μm. This channel has a moderate spectral resolution (R $\sim$ 200) and high spatial resolution of 0.25 mrad (25 m @ 100 Km altitude). VIRTIS-M obtains hyperspectral images of the planet; an example at one wavelenght is shown in Figure 1.7;

- a high-resolution channel, VIRTIS H (named -H), devoted to spectroscopy, providing high resolution spectra in the wavelength range 2-5 μm and housed in the High resolution (-H) optical subsystem. This channel is characterized by a resolving power of about 1000 $\div$ 2000 (R). VIRTIS-H data are subdivided in 8 orders which overlap in a part of the spectral range. In figure 1.8 an

example of VIRTIS-H spectrum with all orders is shown. Order 0 starts at 5 micron, till order 7 up to 2 micron. The resolution is higher in the spectral region at lower wavelengths of each order, but due to some residual stray light on should infer, case by case, the best order for the specific study.

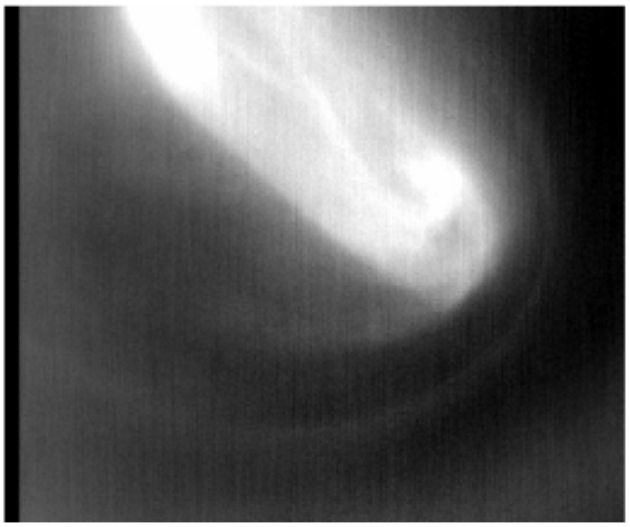

Figure 1.7: *A suggestive image of the Venus polar region acquired by VIRTIS-M @ 5 μm. We can observe the polar vortex called dipole for its shape.*

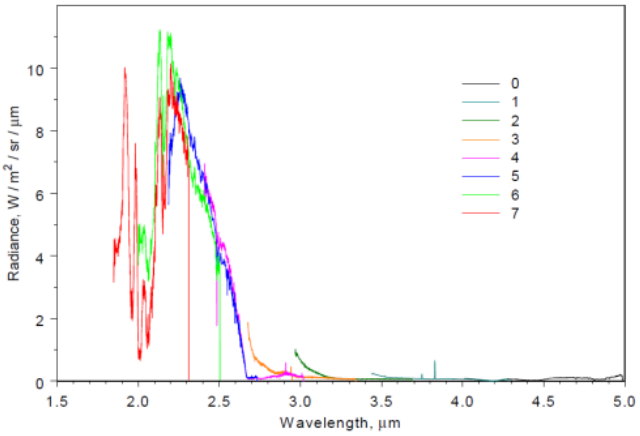

Figure 1.8: *Venus spectra acquired by VIRTIS-H in the dayside of Venus, with all 8 orders shown in the figure.*

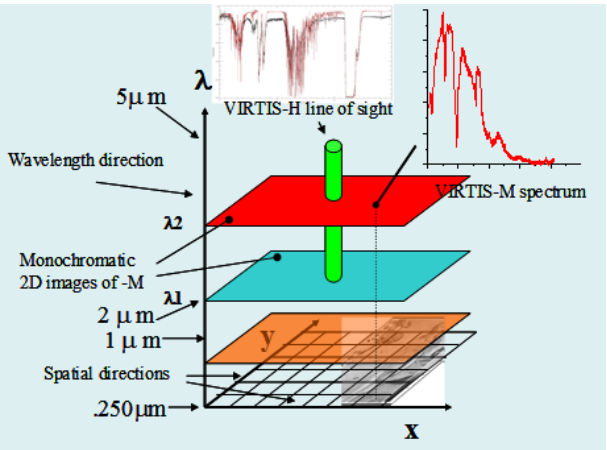

Figure 1.9: *The output from VIRTIS-M can be considered to be a large set of stacked monochromatic two-dimensional images in the range between 0.25 to 5 µm, at moderate spectral resolution. The field of view of VIRTIS-H centered in the middle of the M channel image provides spectra at high spectral resolution in this small portion of the frame.*

The focal planes, with Charge Coupled Device (CCD) and infrared detectors achieve high sensitivity for low intensity sources. Due to the high flexibility of the operational modes of VIRTIS, these performances are ideally adapted for the study of Venus atmosphere, both on night and day sides. In fact, VIRTIS provides a 4-dimensional study of Venus atmosphere (2D imaging + spectral dimension + temporal variations), the spectral variations permitting a sounding at different levels of the atmosphere, from the ground up to the lower thermosphere. The infrared capability of VIRTIS is especially well fitted to the thermal sounding of the night side atmosphere which gives a tomography of the atmosphere down to the surface; information about the clouds can also be retrieved from dayside observations and in both InfraRed and visible range.
In Figure 1.9 a simple graphic representation of the output data is given.

1.4.1 VIRTIS M

Telescope

The Shafer-type telescope is the combination of an inverted Burch telescope and an Offner relay. The Offner relay takes the curved, anastigmatic virtual image of the inverted telescope and makes it flat and real without losing the anastigmatic quality. Coma optical aberration is eliminated by putting the aperture stop near the center of curvature of the primary mirror, thus making the telescope monocentric. The result is a telescope system that relies only on spherical mirrors yet remains diffraction-limited over an appreciable spectrum and all the vertical field (slit direction). At ± 1.8 degrees the spot diameters are less than 6 μm in diameter, which is 7 times

smaller than the slit width. More information about the optical design for the VIRTIS-M instrument can be found in [4].

The horizontal field is realized by rotating the mirror of the Shafer telescope around an axis parallel to the Y-axis of the spacecraft. The optical system is not diffraction-limited over the overall field but the optical quality is still sufficient. An image of the optical configuration is shown in figure 1.10.

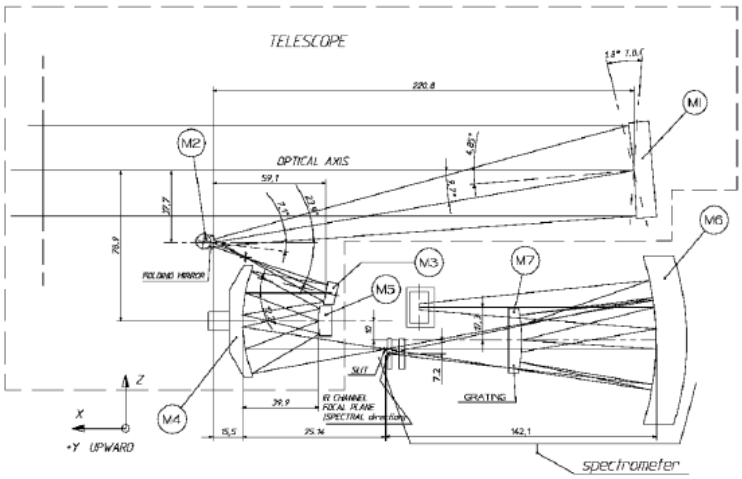

Figure 1.10: *Virtis-M optical design: Shafer telescope and Offner spectrometer*

Spectrometer

The VIRTIS-M Offner spectrometer not only does away with redundant optical systems, but also eliminates the need for collimators, camera objectives and beam splitters, thereby simplifying fabrication and minimizing volume and mass. However, a grating spectrometer that does not rely on a collimator and camera objective requires perfect matching with its collecting telescope. Not only must they have matching F♯, but the telescope must be telecentric or have its exit pupil positioned on the grating. The Shafer telescope is matched to the Offner spectrometer because both are telecentric. This means that the entrance pupil is positioned in the front

focal length of the optical system 750 mm in front of the primary mirror. The VIRTIS-M spectrometer grating does away with the beam splitter by realising two different groove densities [11] on a single substrate. An image is shown in figure 1.11. Since the pupil optics conjugate is on the grating, the same spectral beam

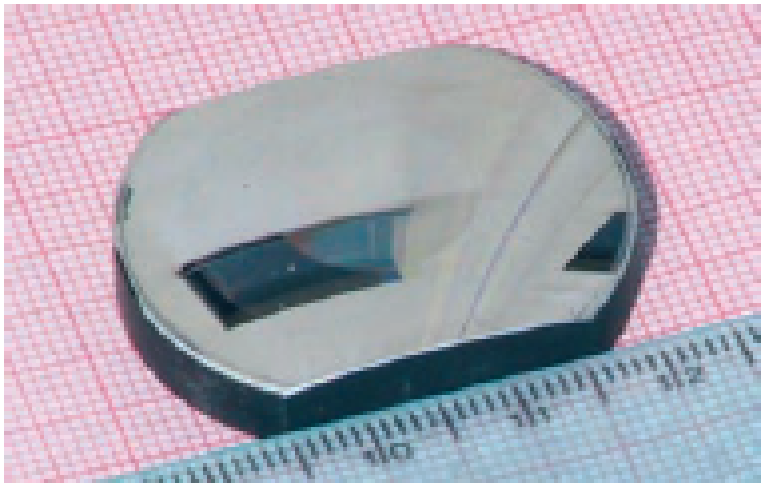

Figure 1.11: *The VIRTIS-M grating used for the development model. The two inner regions are for the visible range, the external one is for IR. The dispersion axis is roughly along the ruler. The surface geometry is convex.*

splitting is performed for each Field Of View (FOV) angle. The grating profiles are holographically recorded into a photoresist coating and then etched with an ion beam. Using various masks, the grating surface can be separated into different zones with different groove densities and different groove depths.

The visible Focal Plane Array (FPA) is based on the Thomson-CSF TH7896 CCD detector. It uses a buried channel design and two poly-silicon N-MOS technology to achieve good electro-optical performance. It includes a multi-pinned phase boron implant to operate fully inverted and to reduce substantially the surface dark current, residual images after strong exposure and other effects due to ionizing radiation. In order to generate the required information (to meet the instantaneous FOV of 250 μrad and to have the same pixel size in the IR and visible detectors), 2 x

2 binning is implemented at the detector level. This approach achieves the required pixel size with a less expensive solution; a 38 μm pixel size is feasible but would require a custom design. The detector is also equipped with two ordering filters with a boundary at band 215 (680 nm) in order to attenuate the higher orders of the visible grating region.

The IR detectors used in VIRTIS-H and VIRTIS-M are based on a 2-D array of IR-sensitive photovoltaic mercury-cadmium-tellurium (HgCdTe). These devices have the potential to operate at a higher temperature than the more established indium antimonide (InSb) detectors owing to dark current reduction by a factor of 10 or more. The array is formed through hybridisation of mercury-cadmium-telluride (MCT) material with dedicated Si CMOS. The device is a MCT-Si hybrid array of 270(w) x 436(h) 38 μm MCT photodiodes with line and column spacing of 38 μm between diode centres, a spectral wavelength range from 0.95 μm up to 5 μm and an operating temperature of 80K. The detector is packaged into a housing which includes an optical window and provides mechanical, thermal and electrical interfaces for its integration on the VIRTIS-H and -M FPAs. The VIRTIS-M filter window is used to stop the superimposition of higher diffraction orders from the grating and also to eliminate/reduce the background thermal radiation due to the temperature of the instrument housing.

The possible modes for VIRTIS-M are summarized in Table 1.1. The overall data rate and volume depend essentially on the selected modes for -M because -H does not much affect the rate (unless special testing modes are used, involving the transfer of the full frame).

	Number of Pixels		Binning		Detectors
	Spectral	spatial	Spectral	Spatial	
Nominal 3x4 Full win	144	64	3	4	vis+IR
VIS only 1x4	288	64	1	4	VIS
IR only 1x4	288	64	1	4	IR
High Spectral 1x4 full win	432	64	1	4	VIS+ IR
High Spatial 3x1 full win	144	256	3	1	VIE+IR
All Pix Full Win	432	256	1	1	VIS+IR
Reduced Slit 3x1	144	64	3	1	VIS+IR
Alter IR only 1x4	288	64	1	4	IR

Table 1.1: *Main modes of the three VIRTIS channels.*

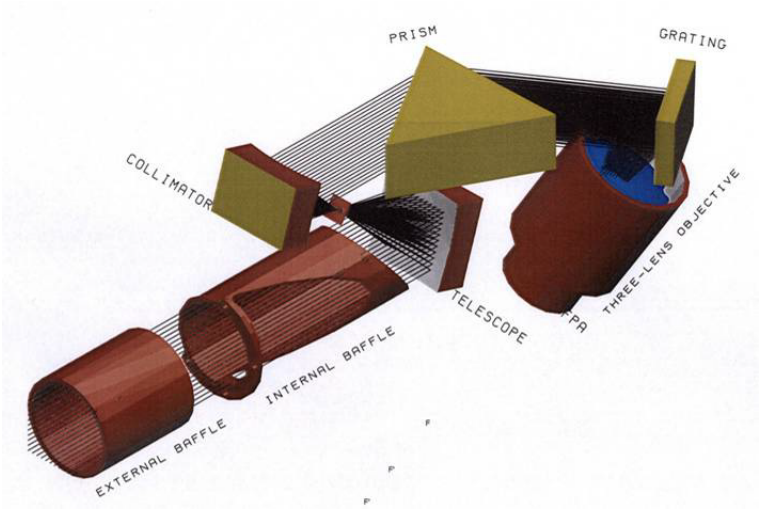

Figure 1.12: *A simplified view of the VIRTIS-H optical scheme.*

1.4.2 VIRTIS-H

In VIRTIS-H the light is collected by an off-axis parabola and then collimated by another off-axis parabola before entering a cross-dispersing prism made of Lithium Fluoride. After exiting the prism the light is diffracted by a flat reflection grating, and is dispersed in a direction perpendicular to the prism (see figure 1.12).

The prism allows the high resolution by separating orders 7 through 16 across a twodimensional detector array. The spectral density grating, which is the echelle

element of the spectrometer, to achieve very high spec resolution, λ $\Delta\lambda$, varies in each order between 1200 and 3500. Since -H is not an imaging channel, it is only required to achieve good optical performance at the zero field position. The focal length of the objective is set by the required IFOV and the number of pixels allowed for summing. While the telescope is f/1.6, the objective is f/1.67 and requires five pixels to be summed in the spatial direction to achieve a 1 mrad^2 IFOV (5 x .45 mrad x .45 mrad). VIRTIS-H uses the same IR detector as VIRTIS-M however, due to the different design of the two channels, the detector is used rather differently. VIRTIS-H is a high resolution spectrometer and does not perform imaging; the H-IR detector is used to acquire spectra spread over its surface, thus only a portion of the pixels contains useful scientific data. The 8 spectral orders are spread over the entire surface matrix. In each spectral order the spectrum covers 432x5 pixels (where 5 pixels represent the image of the slit size when imaged on the detector). Thus overall only 15% of the 438x270 pixels matrix surface is used. To reduce the overall data rate and volume, H uses the so called Pixel Map which gives the exact location of the spectra over the H-IR detector. The ME calculates the location of the pixels to be downloaded and passes it to PEM-H (Proximity Electronics Module-H) which then downloads them accordingly. The downloaded data are the H-SPECTRUM, a set of 432x8x5. One H-Spectrum can be defined as a composition of the 8 orders imaged on the H-IR detector, the H-Spectrum is extracted from the two-dimensional detector by using a map of the lighted pixels based on 8 spectral orders of 432 elements and a width of 5 pixels for each order. The 5 pixels are reduced to 1 pixel by averaging. As H has no spatial resolution the 5 pixels are averaged together, thus the final end-product in the H-Nominal acquisition mode is a 3456 (or 432x8) pixels spectrum representing the full spectral range of the instrument from 1.88 through 5.03 μm.

The main characteristics of the two instruments are summarized in table 1.2.

	VIRTIS-M (Visible)	VIRTIS-M (InfraRed)	VIRTIS-H
Spectral range (μm)	0.3-1.1	1.0 - 5.1	Or0 4.01206-4.98496 Or1 3.44270-4.28568 Or2 3.01190-3.75586 Or3 2.67698-3.33965 Or4 2.40859-3.00570 Or5 2.18903-2.73220 Or6 2.00565-2.50468 Or7 1.85100-2.31194
Spectral resolution $\lambda/\ \Delta\lambda$	100-380	70-360	1300-3000
Spectral Sampling (nm)	1.89	9.44	0.6
Field of View (mrad x mrad)	63.6 (slit) x 64.2 (scan)		0.567 x 1.73
Spatial Resolution (μrad)	250 (slit) x 250(scan)		
Full FOV high resolution Image size (pixels)	256 x 256		
Noise equivalent Spectral radiance ($Wm^{-2}sr^{-1}\mu m^{-1}$)	$1.4x10^{-1}$	$1.2x10^{-4}$	$1.2x10^{-4}$
Telescope	Shafer Telescope	Shafer Telescope	Off-axis parabolic mirror
pupil diameter (mm)	47.5		32
Imaging F$\sharp$	5.6	3.2	2.04
Etendue (m^2sr)	$4.6x10^{-11}$	$7.5x10^{-11}$	$0.8x10^{-09}$
Slit dimension (mm)	0.038x9.53		0.029 x 0.089
Spectrometer	Offner Relay	Offner Relay	Echelle spectrometer
Detectors	Thomson TH7896 CCD	HgCdTe	HgCdTe
Sensitivity area format	508 x 1024	270 x 436	270 x436
Pixel pitch (mm)	19	38	38
Operating Temperature (K)	150-190	65-90	65-90
Spectral range (μm)	0.25-1.05	0.95-5.0	0.95-5.0
Mean dark current	$< e/s$	<2 fA @ 90K	< 2 fA @ 90 K

Table 1.2: *Main characteristics of the three VIRTIS channels.*

1.5 Scientific goals of VIRTIS

VIRTIS is able to produce day and nightside IR and visible spectra. The whole atmosphere is being observed from the mesospheric levels down to the surface ([12]), and the surface itself is accessible to VIRTIS IR observations on the nightside. The main topics for VIRTIS science observations are [13]:

★ study of the lower atmosphere composition below the clouds and its variations (CO, OCS, SO_2, H_2O) from nightside observations [14]. The 2.3 μm window gives access to accurate measurement of minor species. At shorter wavelengths, H_2O is measurable with VIRTIS-M for mapping H_2O variations, as done by NIMS/Galileo [15]. From these observations, correlation with volcanic or meteorological activity is being sought [16](some signatures of volcanic outgassing are related to minor-species variations, in particular for sulphur compounds).

★ study of the cloud structure, composition and scattering properties (dayside and nightside)[17]. The different geometries of cloud reflections along with the spectral range of VIRTIS will constrain the cloud structure. The average structure is known from previous missions, but the temporal and spatial variabilities are less well documented. VIRTIS can sound the different layers and measure their optical thickness in the IR, and measure the upper layer on the dayside.

★ cloud tracking in the UV [18]($\sim$ 70 km altitude, dayside) and IR (45° km altitude, nightside). The correlation of UV and IR observations at different times, along with the 4-day cloud rotation period, gives access to the vertical variation of the wind field up to 70 km altitude.

★ measurements of the temperature field with subsequent determination of the zonal wind in the altitude range 65-100 km (nightside)[19]. The 4-5 μm range is

sensitive to thermal structure, which can be retrieved (on the nightside) and compared with models [20]. Such retrieval gives access to the vertical wind variations through cyclostrophic approximation.

★ lightning search (nightside). Although tentative (there is no reliable information on the frequency of lightning on Venus), observations of transient lightning illumination are of high scientific interest, and is an 'open search' option for VIRTIS observations.

★ mesospheric sounding. Understanding the transition region between troposphere and thermosphere: - non-local thermodynamic equilibrium (non-LTE) O_2 emission (night/dayside) at 1.27 μm (95-110 km; [15]). As observed from the ground and NIMS/Galileo, these emissions have spatial and temporal variabilities, which make them of high interest for accurate spatial mapping by VIRTIS.

★ CO_2 fluorescence (dayside). Non-LTE emissions at 4.3 μm (>80 km; [21] on limb scans by Galileo provide important information on the physics of the upper atmosphere through the collisional/radiative equilibrium sounded through the CO2 band.

★ limb observations (CO, CO_2)[22]: atmospheric vertical structure (>60 km) (day/nightside).

★ search for variations related to surface/atmosphere interaction, dynamics, meteorology and volcanism. Global observation or partial observations at a regional scale on a temporal scale of one Venusian day is allowing the search for correlations between different physical processes.

★ temperature mapping of the surface and searching for hot spots related to volcanic activity. NIMS/Galileo observations of Io showed that lava lakes are easily detected on a planet by imaging spectroscopy. Even if the atmosphere of Venus precludes the clear detection of free lava, a temperature anomaly could be a signature

of some volcanic activity. This has never been attempted with the spatial/temporal performance of an instrument like VIRTIS.

★ search for seismic waves from the propagation of acoustic waves amplified in the mesosphere by looking for high-altitude variations of pressure/ temperature in the CO_2 4.3 μm band [23]. Although clearly a challenge, it is one of the tentative science objectives that would be of primary scientific importance if detected. Gravity waves also have signatures in the IR mesospheric emissions accessible to VIRTIS. Very little is known about wave activity in the upper atmosphere of Venus.

Chapter 2

Planetary atmospheres and notions of spectroscopy

In the previous chapter the remote sensing techniques and the instrumentation employed have been described. A lot of importance has been given to the VIRTIS, the complex spectrometer devoted to study of the Venus atmosphere. In this chapter, we'll give a brief description of the planet considered Earth's twin of size and mass. Besides, in the second part of the chapter we will introduce notions of spectroscopy, a powerful tools of investigation in the field of planetary science. Infrared spectroscopy and present-day high resolution spectrometers have demonstrated to be one of the most powerful remote sensing tools in the context of planetary observation, for atmospheric as well as for surface studies: they give together a remote access to most of the important information carried by the radiation which directly interacted with the planet.

2.1 Venus

Venus, the "Morning Star", is Earth's closest neighbor, the second planet from the Sun and belongs to the family of terrestrial planets, alongside Earth, Mars and Mercury [12]. Its small rotation axis obliquity and orbital eccentricity ensures that no seasons affect its rocky surface where the temperatures rise close to 500°C with a pressure 90 times the Earth's one. Known since ancient times due to its brilliant color, brightness and unusual appearances in the sky, Venus is a planet similar to the Earth in mass and radius but has no moon and no magnetic field shielding it from cosmic rays and solar winds. Venus' obliquity is only 2.6°, compared to 24° of the Earth and Mars and orbits in the prograde direction about the Sun in a nearly circular orbit every 224.7 earth days. Its rotation relative to the stars, the sidereal motion, is retrograde every 243.01 earth days. If the Sun could be seen from the surface of the planet, it would make roughly one complete circuit of the Venusian sky in half a Venus year. Hence, the length of the Venus day, also known as the solar day, is 116.75 Earth days. Since Venus is closer to the Sun than the Earth, the planet shows phases when viewed with a telescope: sometimes it appears as a crescent, others half-illuminated and others nearly full. Galileo Galilei's (1564-1642) astounding observation of this phenomenon in late 1610 was the first 19 irrevocable piece of important evidence in favor of Copernicus's heliocentric theory of the solar system. As an inferior planet Venus revolves around the Sun faster than the Earth; and as the two planets are moving in the same direction around the Sun, Venus appears for a few months in the early morning, some hours before sunrise, then disappears only to be seen as a bright moon-like object emerging after sunset for a further few months before disappearing again. The main orbital and solid body

characteristics of Venus and Earth are given in table 2.1 for easy comparison, while in table 2.2 the Venusian observational parameters are presented.

Venus was explored by a fleet of American and Soviet spacecraft starting with Mariner 2 in 1962, the first successful spacecraft to fly-by Venus, up to the Magellan orbiter in 1990, which produced global detailed maps of Venus' surface using radar mapping, altimetry and radiometry techniques with a resolution of about 100 m. In between, more than twenty missions have explored Venus, including the Soviet Venera 7 in 1970 which was the first spacecraft to land on another planet, Venera 9 in 1975 which returned the first photographs of the surface and the American Pioneer Venus Orbiter in 1978 which carried several atmospheric environment experiments and four entry probes. Magellan's observations further revealed that the surface of Venus is mostly covered by volcanic materials. Volcanic surface features, such as vast lava plains, fields of small lava domes and large volcanoes are common. A color-coded composite of these observations is shown in figure 2.1.

Venus has two major continents, Aphrodite Terra and Ishtar Terra, which occupy only a few percent of the total surface area. Aphrodite Terra, seen figure 2.1, is a long, narrow area which stretches over 150° in longitude and contains a few peaks higher than 8 km. The planetary elevation is calculated over the mean radius of the planet, 6050 km. Ishtar Terra contains the highest elevation region, Maxwell Montes, around 65° N which rises to altitudes of 10.5 km above mean planetary radius. The remainder of the surface of Venus is covered mostly by volcanic materials .
Although Venus has a dense atmosphere, the surface shows no evidence of substantial wind erosion, and there has been only slight evidence of limited wind transport of dust. On Venus we cannot find evidence of plate tectonics (trenches, ridges), as the absence of water in the surface, which evaporated and went lost with the increase

	VENUS	EARTH	VENUS/ EARTH
Bulkparameters			
Mass (1024 Kg)	4.8685	5.9736	0.815
Volume (1010 km^3)	92.843	108.321	0.857
Equatorial radius (km)	6051.8	6378.1	0.949
Polar Radius (Km)	6051.8	6356.8	0.952
Volumetric mean radius (Km)	6051.8	6371.0	0.950
Ellipticity (polar flattening)	0.000	0.00335	0.0
Mean density (Kg/m^3)	5243	5515	0.951
Surface gravity at equator (m/s^2)	8.87	9.80	0.905
Escape velocity (km/s)	10.36	11.19	0.926
Bond albedo	0.76	0.30	2.53
Visual geometric albedo	0.65	0.367	1.77
Solar irradiance (W/m^2)	2613.9	1367.6	1.911
Equivalent BlackBody Temperature (K)	231.7	254.3	0.911
Topographic range (Km)	15	20	0.750
Orbitalparameters			
Semi major axis (106 Km)	108.21	149.60	0.723
Sideral orbit period (days)	224.701	365.256	0.615
Tropical orbit period (days)	224.695	365.242	0.615
Perihelion (106 Km)	107.48	147.09	0.731
Aphelion (106 Km)	108.94	152.10	0.716
Synodicnvelocity (days)	583.92	-	-
Mean orbital velocity (km/s)	35.02	29.78	1.176
Max. orbital velocity (km/s)	35.26	30.29	1.164
Min orbital velocity (km/s)	34.79	29.29	1.188
Orbit inclination (deg)	3.39	0.00	-
Orbit eccentricity	0.0067	0.0167	0.401
Sideral rotation period (h)	5832	523.9345	243.686
Length pf day (h)	2802.0	24.0000	116.750
Obliquity (deg)	177.36	23.45	0.113

Table 2.1: *Venus/ Earth comparison (after Williams,2005).*

Distance from the earth	
Minimum (10^6Km)	38.2
Maximum (10^6 Km)	261.0
Apparent diameter from Earth Maximum (seconds of arc) Minimum (seconds of arc)	 66.0 9.7
Means value at inferior conjunction with the Earth	
Apparent diameter (seconds of arc)	60.2

Table 2.2: *Observational parameters.*

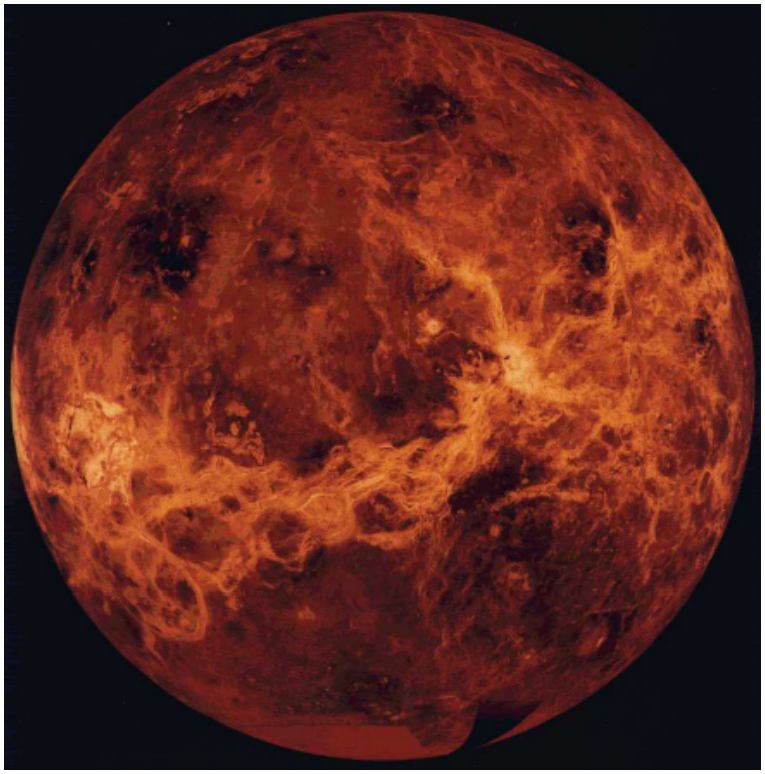

Figure 2.1: *Colour-coded topographic map of Venus from Magellan radar observations. Aphrodite Terra appears as the bright feature along the equator with an area the size of South America (NASA).*

of greenhouse effect, did not help the subduction of the crust; this on the contrary induced an increase of heat which produced diffuse volcanism [24]. Moreover on the Venus surface there is no clear distinction between basaltic (ocean) crust from

continental granitic crations, as observed on our planet. The absence of craters on Venus is an indication of a young surface, which is dated no more than 1 Gy.

2.1.1 Venus's atmosphere

The atmospheric composition of Venus is dominated by CO_2 (96.5%), with a few percent of N_2 (3.5%) and a number of trace gases like H_20, CO and SO_2 in the parts per million scale [25]. This composition resembles the atmosphere of Mars which is also made of $C0_2$ and N_2 and is instead very different from the terrestrial atmosphere where N_2 and O_2 play the leading part. The high surface temperature of Venus (750 K) is significantly above its effective temperature, that is, the equilibrium temperature expected from its heliocentric distance. Indeed, the surface and the lower atmosphere of Venus have been heated by a runaway greenhouse effect, mostly to be ascribed to the large amounts of gaseous CO_2 and H_2O which were most likely present in the primordial atmosphere and, in lesser part, to its cloud coverage.Venus is covered by a thick cloud deck of sulfuric acid H_2SO_4, at an altitude of 40-70 km, which prevents the visible observation of the surface. The atmosphere of Venus may be divided into three natural regions, a troposphere (surface to 60 km), a mesosphere (60 to 90 km) and a thermosphere (above 90 km). On Earth we find a troposphere (surface to 12 km), a stratosphere (12 to 45 km), mesosphere (45 to 85 km) and, as on Venus, a thermosphere (above 85 km). A scheme of the Venus' atmosphere composition is shown in the figure 2.2

Vertical profiles of temperatures on Venus and Earth as a function of pressure at 30° latitude, as measured by the Pioneer Venus OIR and Nimbus 7 spacecraft respectively, are presented in figure 2.3 on the left. Throughout the troposphere and mesosphere the temperature decreases with height, from around 740 K to 100

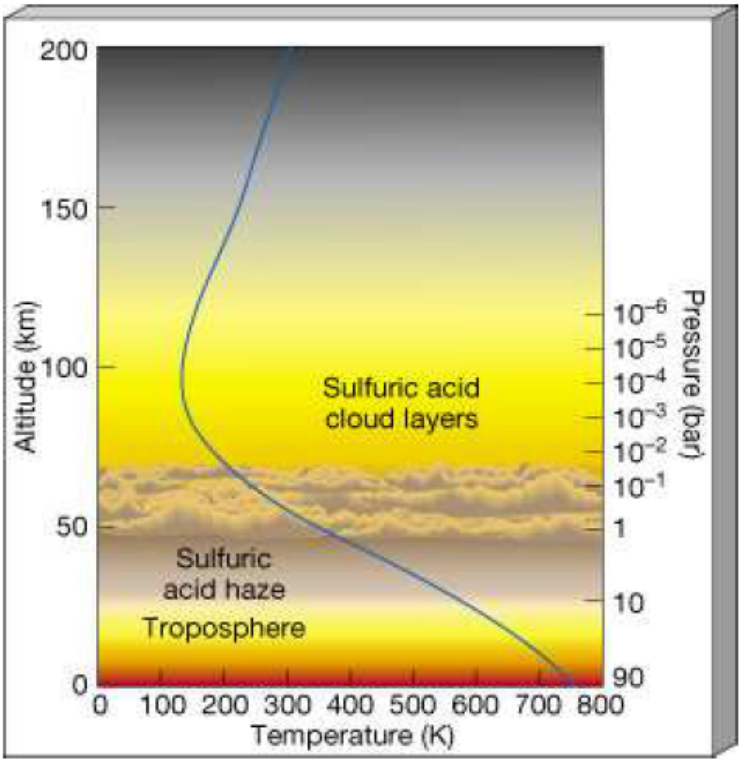

Figure 2.2: *The structure of Venus's atmosphere showing the main cloud layer and also how temperature (blu curve) varied with height.*

K on Venus and from 280 K to 210 K on Earth. No temperature inversions can be seen since UV absorbing ozone that cause the Earth's stratosphere do not exist in the Venus' CO_2 dominated atmosphere. On Venus' dayside the temperature above 85-90 km rises to an exospheric value of around 300 K due to solar EUV absorption and therefore behaves like the thermosphere on Earth, where temperatures rise from $\sim$ 180 K to $\sim$ 1000 K. The nightside upper atmosphere on Venus differs from that on Earth because Venus' slow rotation period causes solar heating to be absent for far too long to maintain the high temperatures found on the dayside. Night side temperatures on Venus' thermosphere above 85-90 km in fact do not rise above 100 K, justifying the name of "cryosphere" ("sphere of cold" in Greek). The Venus temperature structure above the clouds and the thermosphere/cryosphere region is

shown in Figure 2.3 on the right, as observed by three Pioneer probes and Venera 11 and 12.

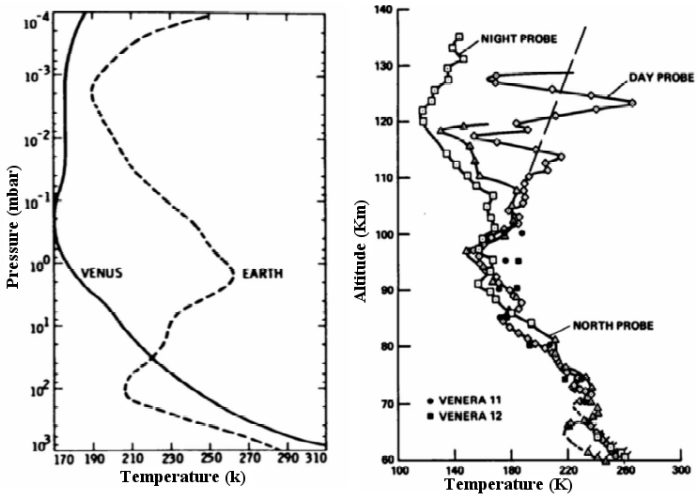

Figure 2.3: *Vertical profile of pressure vs temperature at 30° of latitude North, as measured on Venus by PV OIR and on Earth by Nimbus 7 (on left) [26]. Temperatures above the main cloud regions derived from the Pioneer probes and Venera 11 and 12 (on right) [27].*

Due to its slow rotation rate and its obliquity, the troposphere of Venus is almost isothermal in equatorial and middle latitudes. Near the poles of Venus, starting at 60° N, a long-lived dramatic instability occurs, known as the "polar collar" (or cold collar), which takes the form of a ribbon of very cold air about 10 km deep and 1000 km in radius, centered on the pole and situated at about 64 km of altitude. Inside the polar collar temperatures are about 40 K cooler than outside the feature. Poleward of the inner region of the collar lies at about 65 km the "polar dipole", a feature consisting of two well-defined warm regions circulating rapidly around the pole with a period of 2.7 days.

2.2 Notions of molecular spectroscopy

Spectroscopy is an extremely powerful tool in the study of atoms and molecules. It is well known that when an electromagnetic radiation falls on a gaseous, liquid or solid material, which may be atomic or molecular in nature, the radiation may be: *transmitted*, *scattered* and *absorbed*. The process of absorption by an atom or molecule, is illustrated by (a) in figure 2.4 where m and n are stationary states.

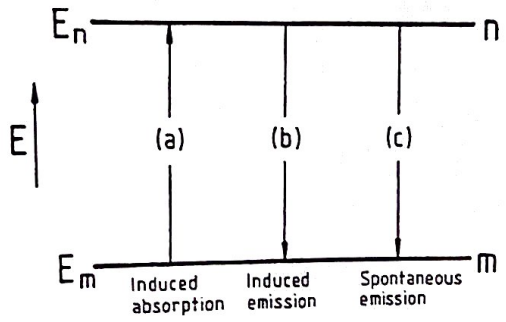

Figure 2.4: *Illustration of the absorption and emission process which may take place between two stationary states m and n.*

Although this state is independent of time, the absorption process is not instantaneous and it take a period of time t_1 given by:

$$t_1 = \nu^{-1} = (c\tilde{\nu})^{-1} \tag{2.1}$$

where the frequency ν or wavenumber $\tilde{\nu}$, is related to the energy separation of the state ΔE by

$$\Delta E = E_n - E_m = h\nu = hc\tilde{\nu} \tag{2.2}$$

These internal molecular energies are all quantized and can be separated into

electronic, vibrational and rotational. The first type of energy is typically associated with the absorption or the emission in the visible part of the electromagnetic spectrum, the vibrational and rotational are typical of the infrared and microwave regions, respectively. A molecule consisting of two (or more) nuclei is held together by valence binding forces of electrons and balanced by internal repulsion forces. The molecule is in ground state when the outer electronic configuration is in equilibrium and has potential energy in electronic form when the configuration is unstable due to acquisition of energy either via absorption or collision. Since the internuclear spacing is large compared to the diameters of the nuclei, which act as point masses, the molecule possesses moments of inertia about certain axes and can therefore rotate about them. Small changes in energy levels can produce changes in kinetic energy of rotation and thus angular velocity of rotation. The valence bond holding the nuclei together is not rigid, thus it can be stretched and compressed slightly, creating changes in intermolecular distance. This elastic bond allows the nuclei to vibrate about their equilibrium positions; however transitions between vibrational energy levels require much more energy than those of rotation. Even more energy is needed for the energy change associated with electronic arrangement. However, vibration and rotation do not occur separately in nature and observed spectra show both types of transitions simultaneously in their line structure. The vibration-rotation combination gives rise to a rotational line structure around each vibrational line. Quantum mechanics explains the quantized energy states available to an electron in orbit about a nucleus. Additional consideration of elliptical orbits, relativistic effects, and magnetic spin orbit interaction was needed to explain the observed emission spectra in more detail, including the line structure observed. Explanation of molecular emission lines is still more complicated. Gaseous emission spectra are

found to have atomic spectral lines with many additional molecular emission lines superimposed. The spectra structure is due to the state of the matter and three major types of molecular excitation are observed:

- line spectra: is a discrete sequence of separated spectral lines at different frequencies and represents the electronic excitation when the orbital states of the electrons change in the individual atoms.
- band spectra: is when the lines are condensed in a specific region of frequencies, forming bands separated each other. It represents the vibrational excitation when the individual atoms vibrate with respect to the combined molecular center of mass.
- continuous spectra: is many frequencies in a relatively wide spectral region. The rotational excitation when the molecule rotates about the center of mass.

2.2.1 Line shape

If a spectrometer was infinitely perfect, the absorption process of a photon by an atom would show an infinitely narrow feature, a zero width line centered at only one absolute frequency. For the real instruments, a line is not monochromatic and always appears spread over a finite wavenumber range with a definite and reproducible line shape [10]. The instrumentation used for observing a spectrum in fact, is itself one of the major limiting factor in the observed line shape. But not the only factor. There are several factors, other than instrumental ones, which contribute to the observed line shapes. Different physical processes are involved in the absorption and emission of radiation by atoms or molecules, all contributing to the lines spread. The most important are the *natural line broadening*, related to quantum effects, the *pressure*

broadening and *doppler broadening*, more related to the physical state of the gas. The main parameters identyfying a line are the central frequency ν_0 where the absorption or emission occurs, the line intensity S and the shape or profile.

Natural line broadening

According to Heisenberg's Uncertainty Principle, the Natural line broadening arises from the finite lifetime Δt of spontaneous decay transitions. It is a phenomenon of quantum mechanical nature and implies that the energy levels are not precisely defined but have spread of values ΔE. This indetermination is reflected to the times and the frequencies through the famous relation:

$$\Delta E \Delta t = \hbar \tag{2.3}$$

where $\hbar$= h/2π with h Planck's constant.

Being $\Delta t \propto (2\pi\Delta\nu)^{-1}$, to each transition is associated a range of frequencies with a certain probability of interacting with the molecule. The line broadening due to the natural line width is small relative to most other contributions but is contributed to in an identical way by each atom or molecule and so is an example of homogeneous broadening. The natural line broadening is much larger at visible and ultraviolet wavelengths than at infrared wavelengths and is usually much smaller than the broadening seen in planetary spectra. The broadening of lines due to the loss of energy in emission (natural broadening) is practically negligible as compared with that caused by collisions and the Doppler effect.

Pressure (or Collision) broadening

The second reason of the line width is due to the inevitable interactions between atoms or molecules. This broadening arises from the fact that collisions between

molecules, during a spontaneous state transition, diminish the natural lifetime of the transition Δt to the mean time between collisions. If τ is the mean time between collisions in a gaseous sample and each collision results in a transition between two different states there is a line broadening $\Delta\nu$, coming from:

$$\Delta\nu = (2\pi\tau)^{-1} \tag{2.4}$$

The relation between pressure and line shape was obtained by Lorentz and has become known as the Lorentzian line shape:

$$\Phi_L(\nu - \nu_0) = \frac{\alpha_L/\pi}{(\nu - \nu_0)^2 + \alpha_l^2} \tag{2.5}$$

where α_L is the Half Width at Half Maximum (HWHM) that, if we use the kinetic gases theory, is equal to:

$$\alpha_L = \alpha_{L0}\frac{p}{p_0}\sqrt{T_0}T \tag{2.6}$$

where $p_0 = 1000$ mb, $T_0 = 273$K and α_{L0} is the HWHM value at temperature and pressure standard conditions. In predicting the line shape due to collisions, Lorentz assumed that, on collision, the oscillation in the atom or molecule is halted and, after collision, starts again with a phase completely unrelated to that before collision. Because α_L is proportional to the pressure and being the expression normalized, for high values of pressure, the contribution of the wings of the function become important. We mention other two important aspects of the HWHM: α_{self} and α_{air}. The first one is due to the effect of the pressure of a molecule by all the other molecules of the same specie, the second one is due to all the other molecules in the gas. If a specie is only in trace in the atmosphere, the first one is often negligible.

Doppler broadening

It's well known that the relative motion between an observer and an emitting source produces the Doppler effect. In a similar way the frequency of the radiation absorbed during a transition in an atom or molecule differs according to the direction of motion relative to the source of radiation. The shape of the Doppler line is given by:

$$\Phi_D = \frac{1}{\sqrt{\pi}\alpha_D} exp - \left(\frac{(\nu - \nu_0)^2}{\alpha_D^2} \right) \tag{2.7}$$

with

$$\alpha_D = \frac{v_0 \nu_0}{c} \nu_0 = \sqrt{\frac{2k_b T}{m}} \tag{2.8}$$

where ν_0 is the frequency of the photon, v_0 is the velocity obtained from the Maxwell distribution and m is the mass. If for the pressure broadening the pressure is responsible for the line width, in this case is the temperature. Being α_D proportional to the temperature in fact, heavy molecules give low broadening and vice versa.
In most gas phase spectroscopy, line broadening is due to Doppler (inhomogeneous) and pressure (homogeneous) broadening, but only a low frequencies is difficult to reduce pressure broadening to such an extent that Doppler dominates. For example, in microwave and millimeter wave spectroscopy a typical HWHM intensity is 1-10 KHz due to pressure broadening at pressure of only few bar compared to about 10 KHz due to Doppler. Under these conditions of comparable to inhomogeneous and homogeneous line broadening, the line shape is a combination of Gaussian and Lorentzian and is called a Voigt profile.

Voigt line shape

The composite line profile, which must now include the effects of both, is obtained from the convolution of the two profiles. The Voigt line shape approaches the Lorentz

line shape at high pressures and the Doppler line shape at low pressures. Skipping all the calculations, the final expression of the shape is:

$$\Phi_V(\nu) = \frac{r_{l/D}}{\sqrt{\pi}^3 \alpha_D} \int_{-\infty}^{\infty} \frac{e^{-y^2} dy}{(v-y)^2 + r_{L/D}^2} \tag{2.9}$$

where $r_{L/D} = \alpha_L/\alpha_D$, $v = (\nu - \nu_0)/\alpha_D$ and $y = v_x/v_0$ with v_x velocity of the particle along the x axis. The expression 2.9 is called Voigt profile and if normalized, describes both the Natural-Pressure and Doppler broadenings. In particular:

- for $r_{L/D} \longrightarrow 0$ gives Doppler profile
- for $r_{L/D} >> 1$ follows Lorentzian profile;
- for values of $r_{L/D}$ between the two previous ones shows a Doppler shape like near the center of the line and a Lorentz shape like on the wings.

The Voigt line has no analytical expression but can be computed numerically. However, once the line shape $\Phi(\nu)$ is known, in order to obtain a complete spectral information we have to consider the product of the line shape and the intensity of the absorption or emission process:

$$\sigma(\nu) = S\Phi(\nu - \nu_0) \tag{2.10}$$

where S is defined as the line strength expressed in m^2/s units.

2.2.2 Rules to build up a spectrum

In this section the interaction of radiation with the gas will be treated. We will list some basic rules that allow us to reconstruct the absorption spectrum. For a more

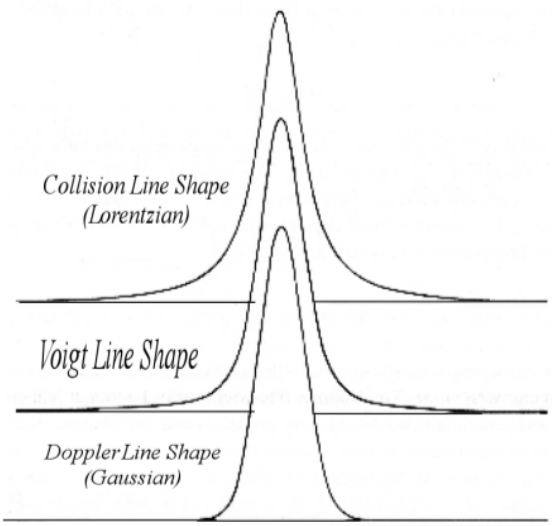

Figure 2.5: *Voigt line profile compared with a Lorentz and Doppler line profiles. All three profiles have the same maximum and half width amplitude for an easy comparison.*

detailed description refer to [10] and [9]. Infrared photons can excite rotational and vibrational modes of the molecules. They are insufficiently energetic to excite the electronic transitions in atoms, which occur mostly in the visible and ultraviolet. As mentioned above, gas molecules can alter their states of vibration and rotation by exchanging energy with the radiation field. This exchange occurs in discrete quantities, resulting in modifications to the field at specific frequency or wavenumber associated with resonance in the molecular structure. As a consequence, molecules absorb and emit radiation in a complex pattern of discrete lines that coincide with the discrete energy difference and frequency as shown in equation 2.2. A molecule can be see as an aggregate of atoms bound together by a balance of mutually attractive and repulsive forces. Individual atoms vibrate with respect to one another while the molecule as whole rotes about any spatial axis. Both types of motion occur simultaneously and transition between pairs of vibration-rotation states create the

characteristic patterns of infrared spectra. The overall vibration of the molecule is a linear combination of several fundamental, or 'normal' modes of vibration, each having a well defined vibration frequency.

Vibration

We can see the molecule as a harmonic oscillator. Resolving the time-independent Schrödinger equation [9], we obtain that the energies E(ν) have discrete values and correspond to :

$$E(\nu) = \frac{h}{2\pi}\omega(\nu + \frac{1}{2}) \tag{2.11}$$

where ω corresponds to the classical oscillation frequency of the vibration (rad*sec) and ν **the vibrational quantum number**. This can only be zero or a positive integer. The energy levels form a series of lines whose position is given by:

$\frac{1}{4\pi}$hω, $\frac{3}{4\pi}$hω,$\frac{5}{4\pi}$hω,.....

The zero point energy at ν=0 is not zero but $\frac{1}{4\pi}$hω.

Under this approximation, the selection rule is

$\Delta\nu = \pm 1$.

Experimental measurements of diatomic molecules have shown that in addition to the strong fundamental transition (at ν_0), there are some line of minor intensity. This transition, named *overtone transitions*, are strictly forbidden in the harmonic oscillator approximation but they are allowed in the *anharmonic* case because small transition probabilities exist between any two states. This transition follow the rule

$\Delta\nu = \pm 2$.

Finally, the selection rule becomes

$\Delta\nu = \pm1, \pm2, \pm3, ...$

Rotation

The rotation of a diatomic molecule can be see as two masses rotating around an axis perpendicular to the line joining the nuclei. Under this approximation, the energy equation is:

$$E = \frac{L^2}{2I} \tag{2.12}$$

where I is the momentum of inertia and L=Iω is the angular momentum. Also in this case, resolving the time-independent Schrödinger equation [9], we obtain that the corresponding energies of the rotating molecule are:

$$E = \frac{h^2}{8\pi^2\mu r^2} J(J+1) \quad J = 0, 1, 2, ... \tag{2.13}$$

$$E(J) = \frac{E}{hc} = BJ(J+1) \tag{2.14}$$

where μ is the reduce mass and r is the distance between nuclei. The second equation refer to the energy in units of cm^{-1} and B is called the rotational constant.

The comparison with equation 2.12, lead us to conclude that L, increases approximately as **J**, which can be identified as **the quantum number**. Therefore we can say that L takes the following expression:

$$L = \frac{h}{2\pi}[J(J+1)]^{\frac{1}{2}} \sim \frac{h}{2\pi} J \tag{2.15}$$

The selection rule for a transition between one state J' and J" is:

ΔJ=$\pm$1

This means that the angular momentum can only change in units of h/2π. Applying

this rule, we obtain a spectrum formed by a series of lines equally spaced and begins with a transition at 2B. The intensity increases up to a maximum and then decreases gradually to zero as J becomes large, as shown in figure 2.6. The B constant can be estimated and in general, heavier molecules will have smaller values and smaller line spacings. Really, the diatomic molecules are not perfectly rigid but stretches

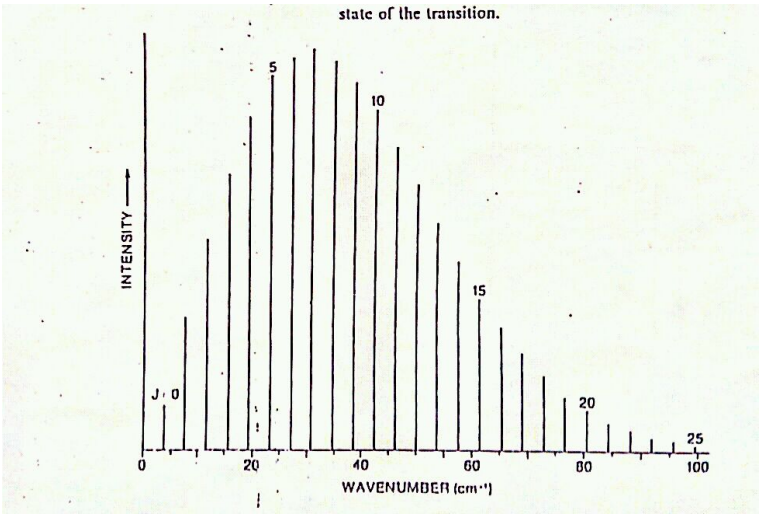

Figure 2.6: *Simulation of a rotational spectrum of a diatomic molecule.*

slightly in response to a centrifugal forces and the rotational energy levels results as a combination of rotation and centrifugal effect. The following equation takes into account both effects:

$$F(J) = \frac{E}{hc} = BJ(J+1) - DJ^2(J+1)^2 \tag{2.16}$$

where D is the centrifugal constant and the minus sign is conventionally written to yield positive value of D.

Vibration and rotation

So far we have treated the rotation and vibration as two indistinctly modes, really they occur simultaneously and transition between energy levels can involve changes

in both modes. The spectrum consist of vibration transitions plus rotational fine structure around each of the vibrational wavenumbers. As a first approximation the rotational energy is given by a combination of rotation plus vibration plus centrifugal distortion, as shown bellow:

$$F(\nu, J) = \nu_0(\nu + \frac{1}{2}) - \nu_0 a(\nu + \frac{1}{2})^2 + BJ(J+1) - DJ^2(J+1)^2 \tag{2.17}$$

where $\nu_0 = \frac{\omega}{2\pi c}$ is the classical vibration wavenumber. The frequency of vibration states is typically much higher than that of rotation, so that the B value results from an average molecular configuration and moment of inertia, as the dimensions change during vibration. B is a function of vibrational state and decreases as ν increases. When the molecule rotates the stretching distortion of the internuclear separation is characterized by D and this effect will change from one vibrational state to another. We have an interaction between vibration and rotation states and, for this reason, the D is also function of the quantum number ν.

Finally, we obtain a complex expression of the energy that takes into account all effects and following shown:

$$\begin{aligned} F(\nu, J) = \nu_0(\nu + \frac{1}{2}) - \nu_0 a(\nu + \frac{1}{2})^2 \\ +B_0 J(J+1) - \alpha(\nu + \frac{1}{2})J(J+1) \\ -D_0 J^2(J+1)^2 - \beta(\nu + \frac{1}{2})J^2(J+1)^2 \end{aligned} \tag{2.18}$$

The rotational energy level structure in each vibrational state (see last two terms in equation 2.18), is similar to the form of the equation 2.16, except that the rotational coefficients are now D(ν) and B(ν), i.e. function of the quantum number ν. A transition between two vibration-rotation energy levels will be accompanied by

emission or absorption of a photon at wavenumber:

$$\nu = \frac{E'}{hc} - \frac{E"}{hc} = F(\nu', J) - F(\nu", J) \tag{2.19}$$

where F(ν,J) is given by equation 2.16. Each transition appears in the spectrum as a band, or set of lines corresponding to the many rotational transitions that may accompany a vibrational transition. The separation between rotational lines are much smaller than the separation between vibrational bands. Each band is centered at its vibrational wavenumber and is composed of two series of rotational lines, called R and P branch. The first extends to higher wavenumbers and described by

$\nu=\nu_0$+2B(J+1) $\Rightarrow$ for ΔJ=+1

The second one, extends toward lower wavenumber and described by

$\nu=\nu_0$-2B(J+1) $\Rightarrow$ for ΔJ=-1

Lines in P and R branches are separated by approximately by 2B; an example of spectrum are reported in figure 2.7.

Polyatomic molecules

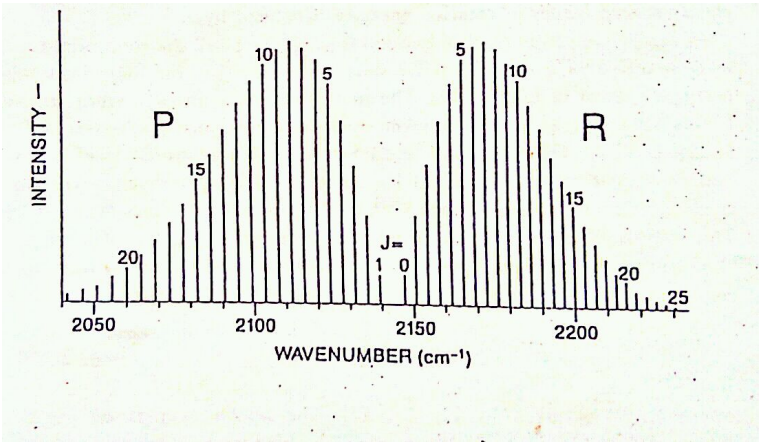

Figure 2.7: *Simulation of ν=1-0 transition of the CO. The band center is at 2143 cm^{-1} and the P and R branches extend toward lower and higher wavenumbers.*

Everything has been said so far can be extended to the polyatomic molecules, taking into account that in this case the molecule vibrates in several modes each with a different frequency and can rotate around any axis. For the roto-vibrational transitions, we assume that the overall energy is approximately the sum of the vibration and rotation energies.

Rather than describing in detail the various processes , as we did in the previous pages,we will report in the following table the main selection rules.

Vibrational mode	
Total energy	**Vibration selection rule**
$E(\nu_1,\nu_2,...)=\frac{h}{2\pi}\sum_i \omega(\nu_i+\frac{1}{2})$	$\Delta\nu=\pm1$ (harmonicities approximation)
	$\Delta\nu=\pm2, \pm3,...$ (hanarmonicities approximation)
Rotational mode	
Total angular momentum	**Angular momentum along a symmetry axis**
$L^2=\frac{h^2}{4\pi^2}J(J+1)$	$L_\alpha=\frac{h}{2\pi}K$
J and K can have integral values 0,1,2,... with both $\pm$ K allowed	
The energy levels	
$\frac{E(J,K)}{hc}=BJ(J+1)+(A-B)K^2-D_J J^2(J+1)^2-D_{JK}J(J+1)K^2-D_K K^2$	
where B and A are constants and are function of momentum of inertia of the molecule	
D takes into account centrifugal effects	
Vibrational-Rotational modes	
Total Energy	
$F(\nu,J,K)=F_{vib}(\nu)+F_{rot}(J,K)$	
Transitions between two vibration-rotation levels	
$\nu=F(\nu',J',K')-F(\nu'',J'',K'')$	
Selection rules	
$\Delta J=0, \pm1$	$\Delta_{\nu_i}= 0,\pm1, \pm2,...$
$+1 \rightarrow$ R Branch $-1 \rightarrow$ P Branch $0 \rightarrow$ Q Branch	

Table 2.3: *Selection rules to build up an absorption or emission spectra for the polyatomic molecules*

Collision-Induced-Absorption

Homonuclear diatomic molecules, such as H_2, N_2, O_2 and so on, have no permanent dipole moment, and therefore no electric dipole transitions. However, at high pressure and long path length, electric dipole absorption is observed, as we will show in the chapter 5. This absorption results from a short-time collisional interaction between molecules. Radiative transitions among rotational, vibrational and translations states of colliding pairs of molecules can take place, even though they are not allowed in the isolated molecules. This process is especially important in the atmospheres of planets, as Venus and Jupiter. In the latter case, the collision-induced absorption by molecular hydrogen dominates the far infrared spectrum. During a collision, a transient dipole moment aries as the electron distribution is distorted by long-range forces or overlapping charge densities. The shape and intensity of observed spectra are determined by the induced dipole moment μ(R,r_1,r_2) and the interaction potential V(R,r_1,r_2). R represents the intermolecular separation and r are the vibrational coordinates of molecule; both μ and V depend on the orientations of the molecules. The induced dipole moment can arise in collisions between two molecules (CO_2-CO_2, as in our case), a molecule and an atom (H_2-He) or two dissimilar atoms (He-Ar). Collision-induced absorption from free pairs of molecules appear as broad lines or bands located at wavenumbers of the pure rotation or vibration-rotation transitions in the participating individual molecules.

The absorption in the collision induced features, both free pairs and dimers, grows in proportion to both the numbers of molecules per volume element and the number of collision partners. Therefore, collision-induced absorption depends on the product of the densities of the partners. When the molecules are the same, CO_2-CO_2 for example, the absorption depends on the square of the density. The absorption

strength also increases at lower temperatures, since this corresponds to higher densities at a given pressure, and because the molecules are thermally distributed over fewer energy levels.

This behavior is in agreement with the collision-induced-absorption bands observed in our spectra, as will discussed in section 5.3.

For a detailed description of this phenomenon, refer to [28]

Chapter 3

Experimental setup

The reasons that led us to assemble an experimental setup have already been explained in the introduction and will be evident in the course of this work. Therefore, in this chapter a detailed description of the Fourier Transformer InfraRed (FT-IR) spectrometer and the gas cell that allowed us to recreate in our laboratory the same conditions found in the deep atmosphere of Venus are given.

3.1 FT-IR interferometer

The CO_2 absorption spectra have been recorded with a Bruker-Vertex 80 Fourier Transform InfraRed (FT-IR) interferometer; an image is shown in figure 3.1.
The technical specifications described in this section are taken from the Vertex 80 user manual [29].

The instrument is equipped with a Tungsten lamp, air-cooled which emits Visible/Near-InfraRed light and a Globar source that emits Mid-InfraRed light. All external sources can be connected to one of the two inlet ports, as shown in the figure 3.2.

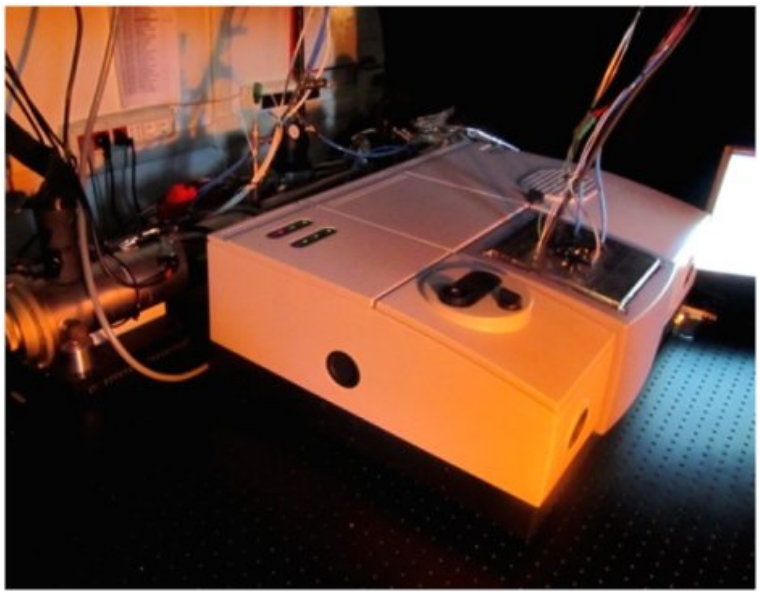

Figure 3.1: *Image of the Fourier Transformer InfraRed (FT-IR) interferometer installed in our laboratory*

The basic spectrometer configuration is equipped with a DigiTec DLaTGS detector with integrated amplifier. This detector package contains an analog-to-digital-converter that converts the analog signal from the detector directly into a digital signal. This digital signal is transmitted to the data processing electronics unit of the spectrometer. The DTGS covers a spectral range from 12000 to 250 cm^{-1}, operating at room temperature and has a sensitivity of D*>2x10^8 $cmHz^{1/2}W^{-1}$. Apart from the standard detector we have also a MCT narrow band, with ZnSe window and liquid N_2 cooled. This detector work from 12000 to 600 cm^{-1} with a sensitivity of D*>2x10^{10} $cmHz^{1/2}W^{-1}$. For the Near-InfraRed spectral range we use a InGaAs Diode detector characterized by a NEP[1]< 2x10^{14} $WHz^{-1/2}$, and operate at room temperature. Finally, for the Visible and UV spectral range we use the Silicon Diode detector with a NEP < 10^{14} $WHz^{-1/2}$ operated at room temperature. The

[1]Noise Equivalent Power

essential part of the interferometer is the beamsplitter which divides the incoming radiation into two beams of nearly intensity. We have two different beamsplitters: a KBr which covers a spectral range from 8000 to 350 cm^{-1} and a CaF_2 broad band for the NIR/VIS and UV regions.

The combination of sources, detectors, beamsplitter and sample compartment window material defines the InfraRed measurement range. The interferometer is equipped with a HeNe laser that emits red light with a wavelength of 632.8 nm and the rated power output is 5 mW. The laser controls the position of the moving interferometer mirrors, also called *scanner*, and is used to determine the data sampling positions. The monochromatic beam produced by the HeNe laser is modulated by the interferometer to generate a sinusoidal signal.

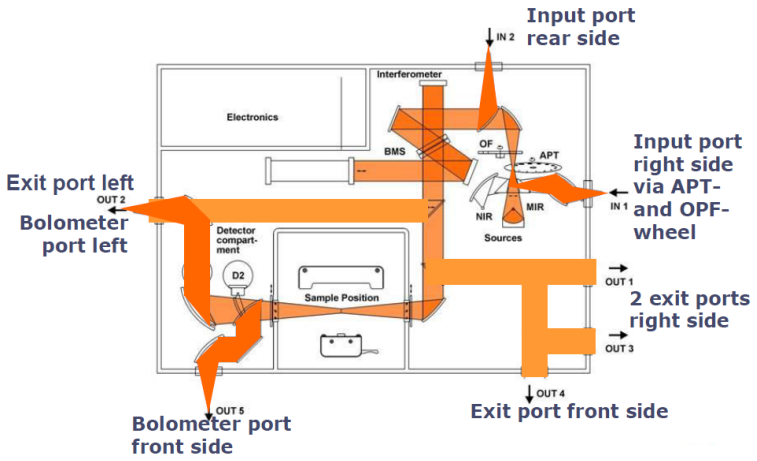

Figure 3.2: *Optical Path configuration of the FT-IR interferometer*

Before describing the optimized procedure that we used for all measurements, it is necessary to know how our FT-IR works.

Referring to figure 3.3, the radiation emitted by the lamps (MIR or NIR), falls the beam-splitter and is divided in two beams, reflected and transmitted respectively.

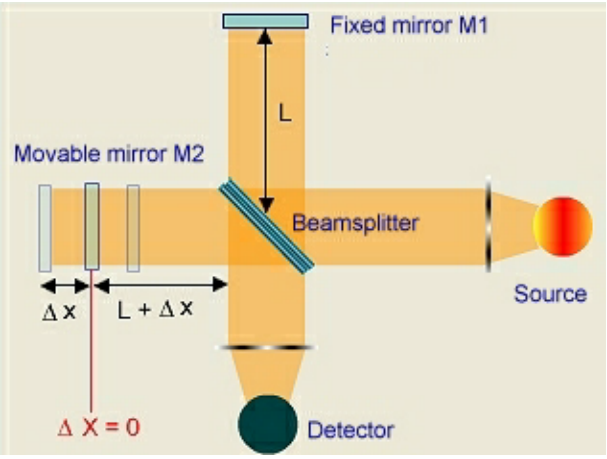

Figure 3.3: *Simplified schematization of an Fourier interferometer*

The reflected beam falls a plane fixed mirror M1, at a distance L, and back towards the beam splitter. The total optical path that the beam travels is 2L. The transmitted beam falls a movable plane mirror M2. As this mirror moves back and forth around L by a distance Δx, the total path is 2(L+ΔX) long. The beams, returning from the two mirrors, are recombined at the beam splitter and, when reach the detector, they have traversed different optical paths with a *path difference* δ=2Δx. The beams are spatially coherent and interfere with each other when recombined. The FT-IR splits and recombined the two beams with relative phase difference that depends on the mirror displacement, or optical retardation.

If δ =0, λ, 2λ,. ... the two beams interfere constructively at the detector yielding a maximum signal.

If δ=$\frac{\lambda}{2}$, $\frac{3\lambda}{2}$, $\frac{5\lambda}{2}$,....the two beams interfere destructively yielding a minimum signal.

The complete functional relationship between the intensity I and the path difference Δx is

$$I(\Delta(x)) = S(\nu) * \cos(2\pi\nu\delta x) \tag{3.1}$$

where ν is the wave number and S(ν) is the intensity of a monochromatic spectral

line at ν. Intensity shown as a function of the frequency is called spectrum, and can be obtained by Fourier transformation of the signal that is a function of the optical retardation.

If we consider a no-monochromatic source, the interference already mentioned occurs at each wavelength. The interference patterns produced are summed to get the resulting interferogram, as shown in figure 3.4.

At the zero path difference of the moving mirror (Δx), all wavelengths have a

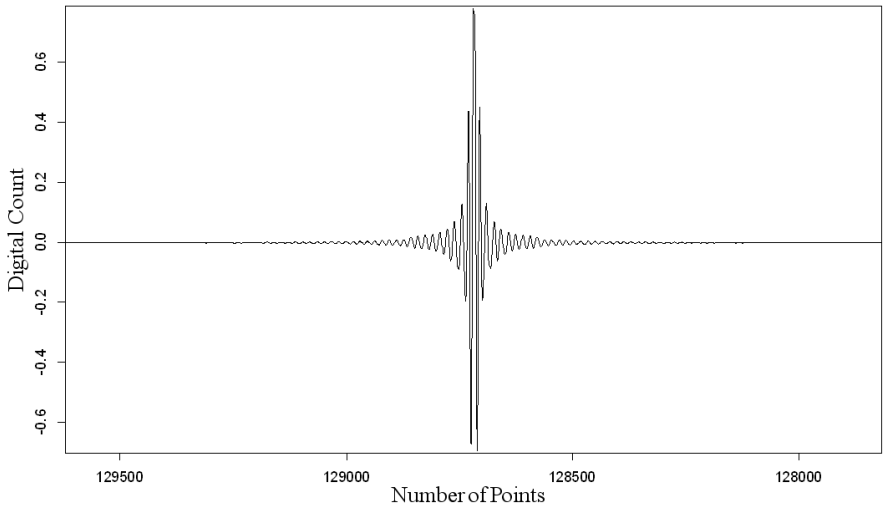

Figure 3.4: *Interferogram recorded by the FT-IR with a resolution of 2 cm^{-1}*

phase difference of zero, undergo constructive interference and sum to a maximum signal. As the optical retardation increases, each wavelength undergoes constructive and destructive interference at different mirror positions and the intensity changes with the retardation. For a broadband source, however, all the interference patterns will never simultaneously be in phase except at the point of zero path difference and the maximum signal occurs only at this point. Data acquisition results in a digitized interferogram, I(x), which is converted into a spectrum by means of the mathematical operation called a Fourier Transform (FT). The general equation for

the FT is applicable to a continuous signal. If the interferogram is digitized, and consist of N discrete, equidistant points, the equation 3.1 becomes:

$$S(K\Delta\nu) = \sum I(n\Delta x) exp\left(\frac{i2\pi nK}{N}\right) \tag{3.2}$$

where n is the discrete interferogram points and K the discrete spectrum points. The fact that we now have a discrete, rather than continuous, function and that it's only calculated for a limited range of n, leads to important effects, named *Picket-fence* effect and *leakage*. This effect occurs if the interferogram contains frequency components which do not exactly coincide with the data point position k*ν in the spectrum. This can be reduced by adding zeros to the end of the interferogram before the FT is performed. This manipulation increases the number of points per wavenumber and reduces the error caused by the *picket-fence effect*. In our case, the original interferogram size should always be at least doubled by zero filling, i.e. zero filling factor of two is chosen.

In a real measurement, the interferogram can only be measured for a finite distance of mirror travel. The resulting can be thought as an infinite length interferogram multiplied by a *rectangular* function, i.e. a function that is equal 1 in the range of measurement and 0 elsewhere. The solution to the *leakage* problem is to truncate the interferogram less abruptly. This can be achieved by multiplying the interferogram by a function that is 1 at the zero path difference and close to 0 at the end of this. This is called apodization function and in the specific case, we used a Blackman-Harris [30] function whose expression is given by:

$$\omega(n) = a_0 - a_1 \cos\left(\frac{2\pi n}{N-1}\right) + a_2 \cos\left(\frac{4\pi n}{N-1}\right) - a_3 \cos\left(\frac{6\pi n}{N-1}\right) \tag{3.3}$$

where a_0=0.35875, a_1=0.48829, a_2=0.14128, a_3=0.01168.

Both optical and electronic effects, can produce a shift of the interferogram phase because the sinusoidal interference patterns of different wavelengths are slightly shifted with respect to each other. These phase shift lead to asymmetry in the interferogram, which is corrected during the Fourier Transform using a Mertz [31] phase correction.

There are many advantages for using an interferometer, the main ones are:

- The sampling interval of the interferogram, δx, is the distance between zero crossing of the HeNe laser, and is therefore precisely determined by the laser wavelength. Since the point spacing in the resulting spectrum, $\delta\nu$, is inversely proportional to δx, FT-IR spectrometers have an intrinsic highly precise wavenumber scale. This advantage is known as *Connes' advantage*.

- The Jacquinot advantage aries from the fact that the circular apertures used in the FT-IR spectrometers have a large area than the slits used in grating spectrometer, thus enabling higher throughput of radiation.

- In the grating spectrometers the spectrum S(ν) is measured directly by recording the intensity at successive, narrow, wavelength ranges. In FT-IR all wavelengths from the sources impinge simultaneously on the detector. This leads to the multiplex, or *Fellgett's*, advantage.

The last statement, does not apply to VIRTIS, because the different wavelengths come and are sampled simultaneously at the focal plane.

The combination of the Jacquinot and Fellgett advantages means that the signal to

noise ratio of the FT-IR spectrometer can be more than 10 times that of a dispersive spectrometer.

3.2 Gas cell

The FT-IR has been integrated with a special customized high pressure-high temperature (HP-HT) gas cell. In figure 3.5, you can see a picture of the cell and a diagram showing the breakdown of the cell into three parts connected by a special viton [2] O-rings.

The technical specifications described in this section are taken from the AABSPEC ♯ 2T-AWT user manual [32]

[2]Fluorocarbon elastomers are highly fluorinated carbon-based polymers used in applications to resist harsh chemical and ozone attack. The working temperature range is considered to be -26°C to +205°/230°C

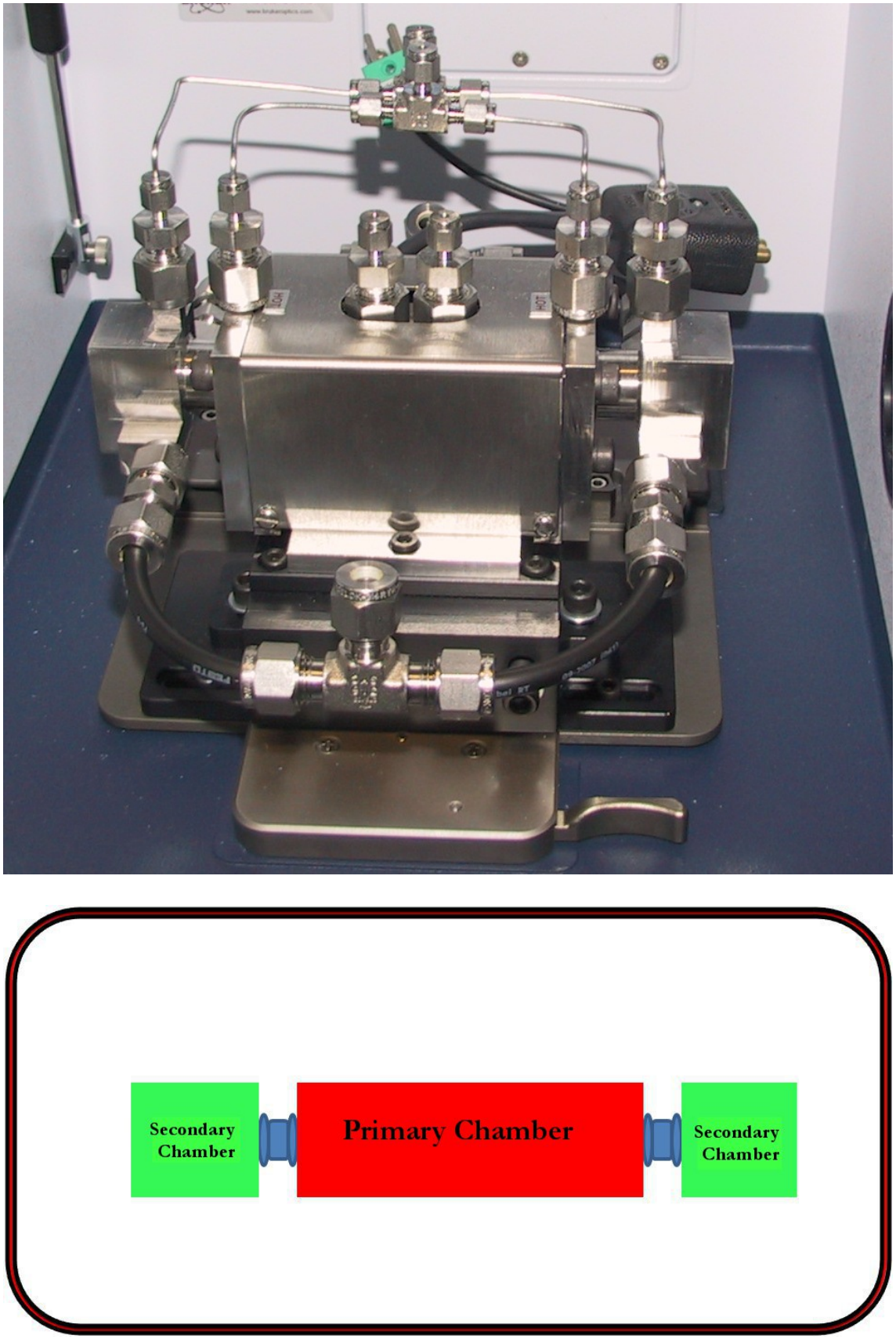

Figure 3.5: *Image of the gas cell integrated inside the sample compartment of the FT-IR (on top) and a diagram showing the three boxes (on bottom)*

The cell is about 2 cm of optical path and designed to support pressure up to 350 bar and temperature up to 650 K. The cell body is formed in a single piece of 316 grade stainless steel with excellent flow-through characteristics. The experimental chamber has four windows of 3 mm in diameter and 5 mm in thickness. Each window is made of zinc sulphide (ZnS), a material which can provide full NIR and MIR spectral range access for gases under combined high temperature and high pressure conditions. Viton O-rings are used to provide a gas tight seal as standard. The O-rings are installed outside the window and are compressed by the special window screw. The window assembly sequence is illustrated in figure 3.6.

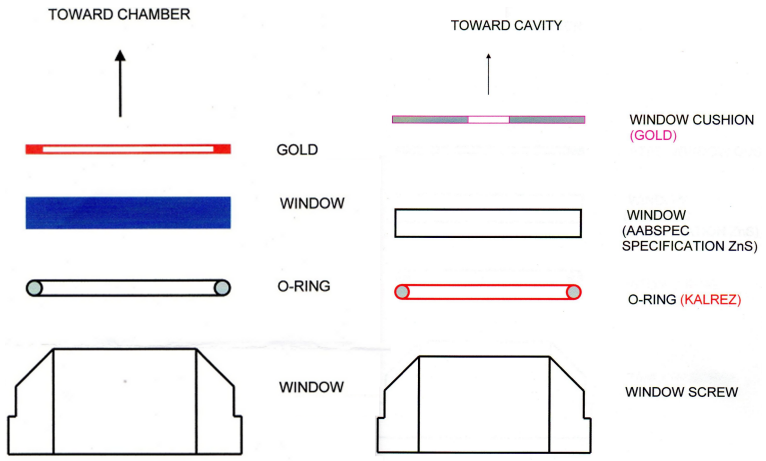

Figure 3.6: *Schematic of the assembly window sequence, for primary cell (on left) and for the secondary chambers on right*

Excessive force should not be used to tighten the window as the design is such that the seal improves as the gas pressure within the cell increases and forces the window back against the O-ring. The maximum pressure to which the cell can be operated depends on the window material used in the secondary chamber. In our case, we have a ZnS window that can support a pressure up to 350 bar.

With this gas cell we can reach high pressure and high temperature because while the primary chamber windows operate at the system temperature and pressure, it is possible by pressuring the secondary chamber to arrange a near zero pressure drop across the primary windows. The pressure differential is then handled by secondary windows which are maintained at near ambient temperature by the cooling system in the secondary window region. The latter have their full mechanical strength as they are maintained in the temperature range from 294K to 330K. The secondary chambers should be pressurized using a low thermal conductivity inert gas, such as Argon. The gas should enter through the port furthest away from the primary chamber. If we are flushing the secondary box during high temperature operation of the gas cell, then we can be sure the gas is cooled before entering the second secondary chamber. The double chamber design also provides inherently greater safety for hazardous sample materials.

The gas cell must be powered from a stable source of 120V, 60Hz supply voltage, which should be stable better than $\pm 1\%$. Unstable supply voltage may significantly shorten the operational life of the heater.

To control the temperature of the primary cell we use an "AABSPEC" Digital Temperature Controllers and Programmers, see the figure 3.7. The technical specifications described in this section are taken from the AABSPEC ♯ DTC-1 user manual [33].

Power is controlled by "time proportional control" with a one second (nominal) cycle, switching at zero crossover with so-called *fail-safe circuitry*. The controller takes its control temperature reading from a type K chromel-alumel thermocouple through a non-reversible connector. AABSPEC Controllers and Programs contain an additional safety feature to give an audible warning in the event of a failure in the

Figure 3.7: *Digital Temperature Controller provides isothermal temperature control in the range from 24 °C to 399 °C.*

final solid state power relay. It's possible for this relay to fail in a closed condition so that it continues to deliver power even when it is instructed by the circuit to go OFF. In this case, an audible warning buzzer will sound continuously and the Controller or Programmer should be switched OFF.

The ON/OFF power switch is to the left of the front panel and illuminates in red when ON (see the figure 3.7). The thumbwheel switch on the right hand side allows us set the temperature in single degree steps; first select °C or K range using the switch on the extreme right hand side of the front panel. When the controller is connect to the device, the temperature selected and the power is switched ON, the red LED indicator will come on if the device temperature is bellow the set point, indicating that power is begin fed to the heater. Once the device temperature is closed to the set point, the red LED will start to flash, the duration of the on interval indicating how much power is being fed to the device. Generally the temperature will initially overshoot and the red LED may go out entirely, then it will come back on again indicating control is being established. Note that the control temperature is being read at a point close to the heater assembly, the device will lag in its

temperature response to the control temperature reading. For this reason, many AABSPEC device provide us with the facility to install a read-out thermocouple to monitor actual device temperature.
The temperature stability will be affected by the stability of the electrical supply voltage which should be stable better than ± 1 %. Other factors which will affect temperature stability include heat loss, for example stability of the cooling fluid temperature and circulation rate.

3.2.1 Connections and calibrations of the set up

As with all control systems, the actual sample temperature is weakly different from the set point and we had to calibrate our experimental setup.
To do this, we installed a type-K thermocouple inside the central box of the gas cell, to read the exact gas temperature. The thermocouple consists of two different conductors (usually metal alloys) that produce a voltage proportional to a temperature difference between either end of the pair of conductor. This sensor has been connected to a Data Acquisition (DAQ), a particular device able to measure an electrical or physical phenomenon such as voltage, current, temperature, pressure, or sound. In figure 3.8 you can see a schematic electrical connection between thermocouple, Data Acquisition and display.

By a program written in LabView (Laboratory Virtual Instrumentation Engineering Workbench) language we read and save the values of gas temperature.
LabView is a graphical programming environment used by engineers and scientists to develop sophisticated measurement, test and control systems. It offers unrivaled integration with thousands of hardware devices and provides hundreds of built-in libraries for advanced analysis and data visualization - all for creating virtual in-

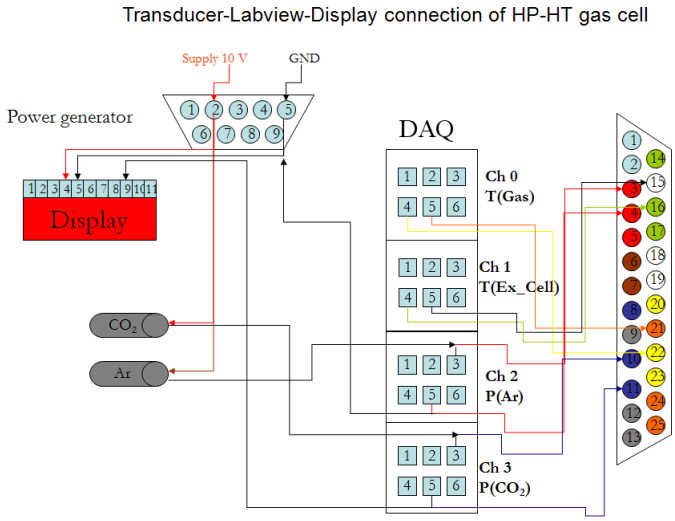

Figure 3.8: *Connections between high pressure high temperature gas cell, Data Acquisition and the display.*

strumentation. Using intuitive graphical icons connected by wires, we design a data structure or algorithm according to a flowchart. This language is defined "data flow" because the execution sequence is defined and represented by the flow of data through the wires that connect one-way function blocks. Since the data can also flow in parallel through consecutive blocks and wires, the language creates spontaneously without explicit multithreading management. The front panel is the user interface and it's realized by controls and indicators, which are the interactive terminal input and output, respectively. The controls are arrays, knobs, buttons, dials and many others, these simulate instrument input devices and provide data to the block diagram. Indicators are graphs, tables, LED, thermometers and many others, these simulating the output and displaying data.

The control panel of our program is shown in figure 3.9.

The first step to calibrate our experimental set up consist of to select a set point, for example 300 K, and to fill the cell with the gas. When the LED in front of view of

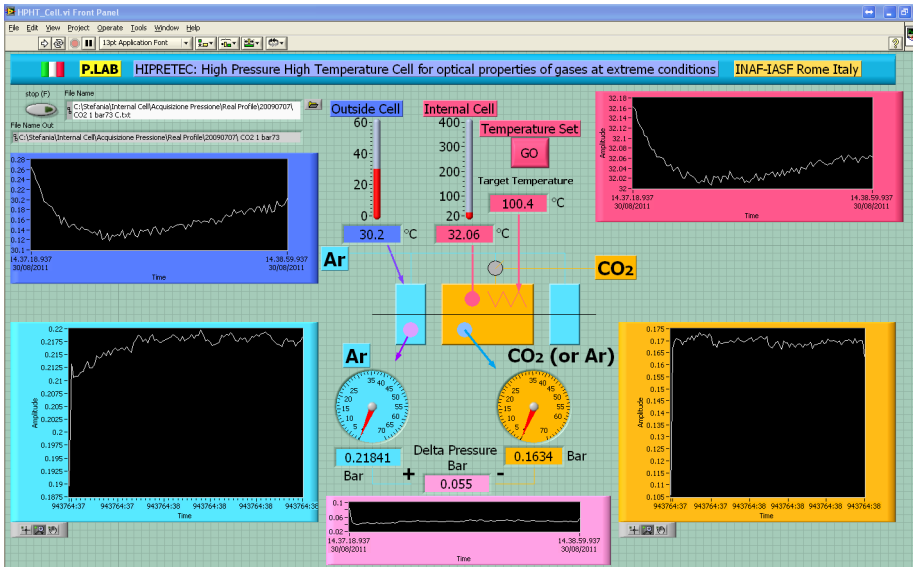

Figure 3.9: *Panel of control of the program written in LabView to acquire pressure and temperature values.*

the controller (see the figure 3.7) start to flash, we are sure that the cell reached the set point temperature. To obtain a calibration curve of our sensor, we varied the set point value from 294 to 600 K with a step of 10 K. For each point of this calibration curve, we record the temperature read by the thermocouple. The calibration curve has been implemented within the acquisition program and it's used automatically to determine the correct set point. For example, in order to have a gas temperature of 370 K we push the Go button (see figure 3.9) and a second window appears, as shown in figure 3.10. Once the temperature value in the "Desired Gas Temperature" is set, we obtain the adjusted temperature to set in the controller (Set T control @) and the final gas temperature (Goal Gas Temperature) is correctly reached.

A second thermocouple has been installed outside the cell to monitor the temperature in order to check that it is always at room temperature. This value is also recorded, as shown in figure 3.9 (outside cell), and for each measurement this temperature is typically less than 30°C.

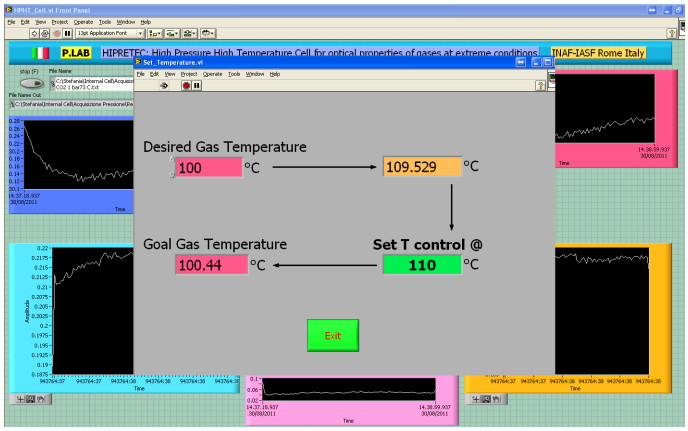

Figure 3.10: *Panel of control to select the temperature of the gas.*

To insert the CO_2 and Argon gases inside the gas cell, we built up a pipes system connecting the gas bottles with the cell. This system consists of seamless tubing of 1/16" in diameter and 0.014" in thickness, valves and reducing union. Along the line we insert two gauges, EPXT-PO type, which measure the pressure of gases with an accuracy better than $\pm$ 0.1% on the full range (from 1 to 100 bar). Also in this case, we record the pressure values read from gauges as shown in figure 3.9.

3.2.2 Measurements procedure

To obtain the gas transmittance, the procedure is as follows: the central box is heated up to the target of temperature, for example 373 K, while the lateral part is maintained cold. The three chambers are filled with Argon (Ar) at the preset pressure, and the background radiance R(ν) is recorded. We chose the argon as the reference spectrum, because there are no bands in the spectral region of our interest. Afterwards the Ar in the central section is replace by CO_2 at the preset pressure and the radiance with the absorption spectrum S(ν) is recorded. An example of background and sample radiance is shown in figure 3.11.

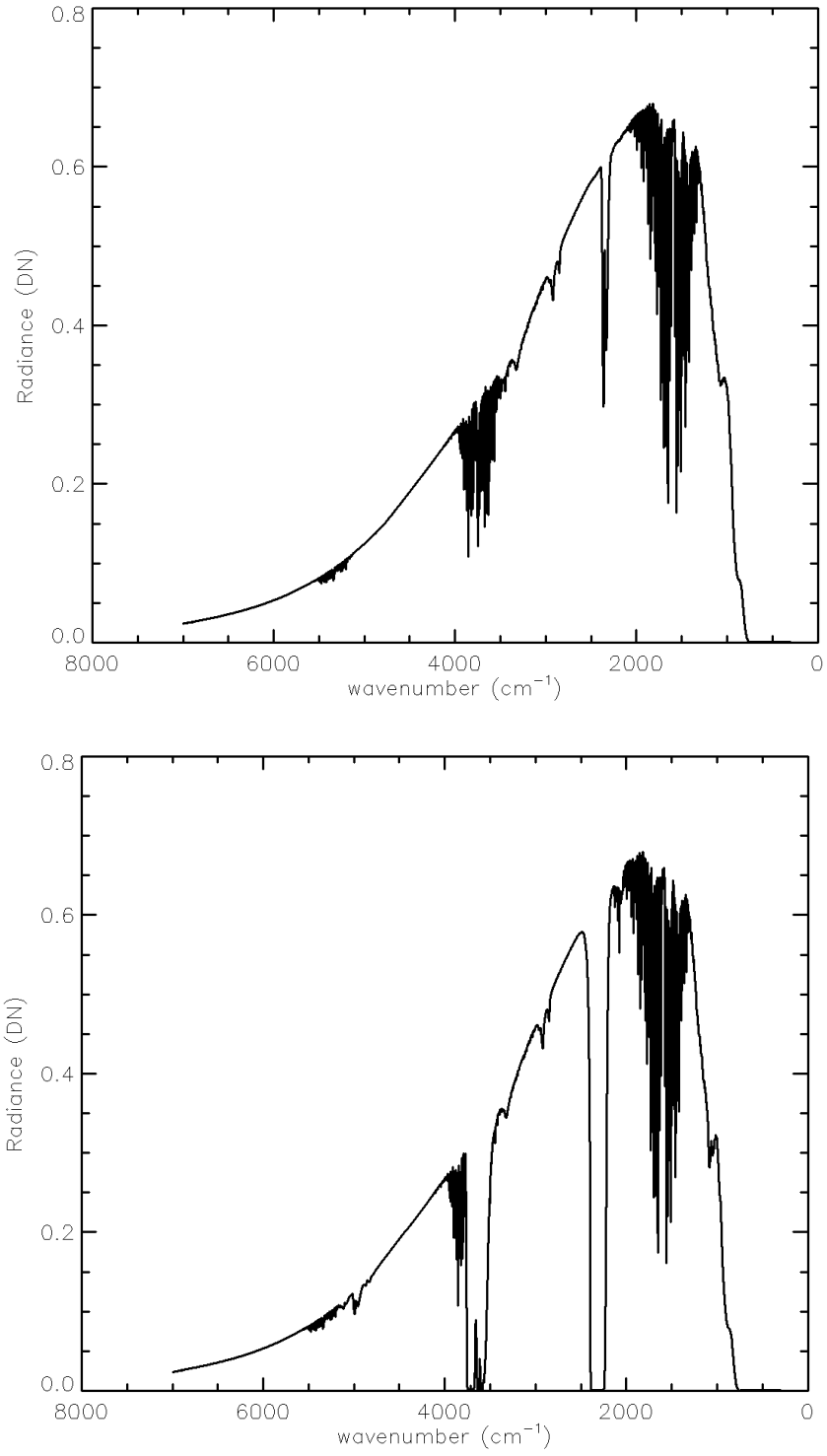

Figure 3.11: *Background and absorption spectrum radiance (from the top down to the bottom) recorded with a resolution of 2 cm^{-1} and Ar and CO_2 at p∼11 bar and T∼513K respectively.*

The transmittance T(ν) is obtained such as ratio between S(ν) and R(ν) as shown in the following expression:

$$T(\nu) = \frac{S(\nu)}{R(\nu)} \tag{3.4}$$

The same procedure has been applied to all measurements.

In the field of planetary sciences, it is customary to speak of **absorbance** or **absorption coefficients** rather than **transmittance**.Therefore, the CO_2 absorption coefficients, being defined as

$$Absorbance(\nu) = -\frac{\ln(T)}{l}(cm^{-1}) \tag{3.5}$$

where l is the optical path, which in our case is (2±0.03) cm along.

We have optimized this procedure to remove the emission of the water vapour and CO_2 along the optical path of the FT-IR. in addition, working at very high pressures, we must monitoring the pressure gradients that act on the windows of the gas cell.

Chapter 4

Radiative transfer models

In principle, all the measured data (earth based, airborne, from space, in laboratory) would be completely useless without any good theoretical model to convalidate them. The opposite is true as well. A model can be said a good model if it is verified by observations. New scientific knowledge occurs only when those two distinct aspects are in agreement with each other, becoming the same thing.

In this chapter three different models that were used to obtain the synthetic spectra will be described. These were then compared with our experimental data. Comparison and discussion on the results are reported in chapter 5.

The first model is based on the **Atmosphere Radiation Spectrum** (**ARS**). It is a set of routines implementing line by line calculation of gases and aerosol opacity, transmittance, and atmospheric radiance spectra. The second one, named **Solution**, is a line shape models valid at high pressure and takes into account two different mechanisms: *"line mixing"* and *"far wings"*. The last one, called **Line Mixing Model** (**LMM**), is a different approach to the lines interferences due to inter-molecular collisions (or *"line mixing"*) which have a very important influence

on the spectral shape.

4.1 ARS: Model and Software

This code is a set of routines written in fortran 77 and C able to perform computations of several physical quantities and to solve the radiative transfer equation under different conditions. Using different packages separately, the code can compute the opacity of gaseous species and aerosols, the transmittance and the radiance spectra with only LTE [1] conditions [34]. The code was originally created and developed by N.I. Ignatiev (IKI RAN-Moskow) to study the data of the Planetary Fourier Spectrometer (PFS), instrument of the Mars Express mission's, but it's now used for other planetary atmospheres by many research teams. In general the radiative transfer problem can be subdivided in two distinct and independent tasks: computation of physical properties and solution of the radiative transfer equation itself. From a informatics point of view, ARS uses many packages and modules. Every package requires a set of initialization files (*.ini) and as sequential boxes, the output of the previous box is the input of the subsequent one. The main packages can be summarized as follow:

- Arshls : this package extracts spectral lines data from a spectroscopic database and converts them into a reduced format file. It is able to change isotopic ratios and Lorentz line half widths. Moreover it can discard all the lines with intensity lower than a chosen value. Another important option is the line wings cutoff, in order to consider the main contribution of the information only. It

[1] Local Thermodynamical Equilibrium: In thermodynamics, a thermodynamic system is said to be in local thermodynamic equilibrium when it is in thermal, mechanical, radiative and chemical equilibrium

can work with different databases also.

- Arsv : once the lines are extracted, the next important step is the creation of a grid with different resolutions. This package can create uniform or combined wavenumber grid, according to different line parameters (positions, widths, strengths, line shape, etc...) in wavenumber units only. It is possible to have uniform spectral range or combine ranges of different resolution. Because the very different number of lines in different parts of a selected spectral range, this last option can be very useful in order to save computational time.

- Arsk : this module of ARS is the real first step to the radiative quantities calculation. It computes gaseous absorption coefficients on the specified resolution grid using all the spectroscopic parameters calculated by Arshls and interpolates absorption coefficients for any temperature and pressure profile defined by the user. The outputs of this package are used by the next module.

- Arsm :this is the main package of ARS. It handles all the monochromatic quantities calculated by Arsk (and Arshls) and solves the radiative transfer equation under different conditions, as said before. In particular it calculates transmittance, radiance and fluxes inside and outside the atmosphere taking into account both single and multiple scattering. The diffusion and emission of the aerosols and the presence of clouds are taken into account in this step.

After a brief description of the software, the role of each single package and how they work together to obtain the final spectra is presented.

4.1.1 What does the program do

Absorption coefficients

First step is the extraction of important spectroscopic parameters from a database. ARS was designed to work mainly with HITRAN [1]. Basically it's a data archive where information on molecular spectral lines are stored in. Arshls extracts the line data from it and converts it into a reduced format. Moreover, it is possible to work with others HITRAN-like databases, if they have a similar data format. Before extracting line data, the user can define many parameters as line intensity, line width and the shape of the line, the isotopes (if any), a different broadening (non-terrestrial atmosphere), wings line and/or weak lines cut-off. In detail, the quantities taken by Arshls from the database for each single line are:

- ν_0 central position of the line in $[cm^{-1}]$ and atmospheric standard conditions: $T_0 = 296\text{K}$, $p_0 = 1$ atm
- $S(T_0)$: line intensity at Temperature T_0
- $\alpha_{air}(p_0, T_0)$: selected gaseous molecule broadening due to the atmospheric environment
- $\alpha self\ (p_0, T_0)$: selected gaseous molecule broadening due to itself
- E": transition lower state energy in $[cm^{-1}]$
- m: exponential index HWHM (Half Width at Half Maximum) Lorentz's line shape vs. temperature ratio

From those informations, the absorption of gaseous species can be computed. The absorption coefficient is the final output parameter of the Arsk package. It works

on the grid created by the user with Arsv which creates an optimized wavenumber grid according with positions, widths and strengths of the lines. Arsk takes into account different steps before coming to the final gaseous absorption coefficient. The mathematical expression for the line intensity is defined as follow:

$$S(T) = S(T_0)\frac{Q(T_0)}{Q(T)}exp\left[-c_2E''\left(\frac{1}{T}-\frac{1}{T_0}\right)\right]\frac{1-exp\left(\frac{c_2\nu_0}{T}\right)}{1-exp\left(\frac{c_2\nu_0}{T_0}\right)} \tag{4.1}$$

where $S(T_0)$ is the line strength at standard temperature conditions

Q(T) is the full statistical partition sum [2]

T is the air profile temperature defined by the user

and $c_2 = \frac{hc}{K_b}$.

The molecular absorption cross-section in cm^2 per molecule in a spectral line with Voigt line shape is given by the formula :

$$\sigma_\nu = \frac{S_a}{\pi^{\frac{2}{3}}\beta}\int_{-\infty}^{+\infty}\frac{exp{-t^2}dt}{a^2+(x-t)^2} \tag{4.2}$$

with

$$a = \frac{\alpha}{\beta} \quad \text{and} \quad x = \nu - \nu_0 \tag{4.3}$$

where S is the line intensity, ν_0 is the line center, α is the Lorentz half width, β is the doppler half width, defined as

$$\beta = \frac{\nu_0}{c}\sqrt{\frac{2RT}{M}} \tag{4.4}$$

[2]Rotational and vibrational energy contributions are both here included

where R is the universal gas constant, T is the temperature and M is the molecular weight in [g/mole] of gas.

Once (and if) Lorentz half width $\alpha(p_0, T_0)$ at the pressure p_0 and temperature T_0 is known, then for other pressures and temperatures it can be computed by the formula:

$$\alpha(p, T) = \alpha(p_0, T_0)\frac{p}{p_0}\left(\frac{T_0}{T}\right)^m \tag{4.5}$$

where m is a parameter particular for each individual line [3]. It should be noticed that the previous formula for the Lorentz line half width includes both air- and self-broadening, the rigorous expression should be written as:

$$\alpha(p, T) = [\alpha_{air}(p_0, T_0)(p - p_s) + \alpha_{self}(p_0, T_0)p_s]\frac{1}{p_0}\left(\frac{T_0}{T}\right)^m \tag{4.6}$$

Even if this is the right expression one should take into account, the code uses the equation 4.5 for simplicity. The reason lies in the weight that partial pressure has to the final spectra. Especially for trace gases the corrections due to the ps are small so that pressure line shift can be ignored. The line by line computational method sums the contributes of all lines for each wavenumber and the total opacity produced by all the lines is equal to the sum of the individual line opacities:

$$\sigma_\nu = \sum_i \sigma_{\nu i} \tag{4.7}$$

[3] When the collision cross-section does not depend on temperature, the theory gives m = 0.5. In practice, m is slightly different and the difference in the broadening conditions on the Earth and other planets should be taken into account.

from this relation the absorption coefficient can be easily obtained as:

$$k_\nu = \sigma_\nu n \tag{4.8}$$

where $n = p/K_bT$ is the number density coming from the perfect gases law. It is important to notice that the absorption data which are stored by Arsk program in the output file are obtained per unit path length and for 100% pure gas.

4.2 Solution

This software, written by the group of the A.V. Rodin (IKI RAN-Moskow), is a line shape models valid at high pressure, when the shape of spectral lines no longer follows the conventional Lorentzian profile. Two mechanisms are thought to be responsible for this effect: "line mixing" [35], or interference of rotational states when individual rotational lines overlap; and dense, short-pathlengths intermolecular collisions [36], which determine far wings of spectral lines and are believed to reveal non-Poisson statistics.
In this section, the two effects will be treated separately.

4.2.1 Line Mixing effect

When we are in a typical terrestrial conditions, the behavior of gases is well described by the ideal gas law. Vice-versa, when we study the optical properties of gases at high pressure and high temperature, such as those found in the deep atmosphere of Venus, this approximation falls. In this case, we assume that the behavior of the

gas is well described by the Wan der Waals law. From a spectroscopic point of view, we have that the average distances between the molecules are comparable to the molecule size, and molecules spend most of their time interacting with each other. This means that the effective energy levels of an ensemble of molecules overlap. It makes sense to consider the vibrational band profile instead of the line profile. This simplest approximation is the **strong collision approximation**, which suggest that the lifetime does not depend on the rotational state and is averaged over the vibrational band. Referring to the "Petersburg model" [37] and considering what we have just said, let's to calculate the absorption coefficients.

The net spectral absorption coefficient k(ν), is a superposition of the absorption produced by transition between different vibrational states:

$$k(\nu) = \sum_j F\left(\sum_i S_{i,j} f(\nu - \nu_i, \Delta_i^L, \Delta^D)\right) \tag{4.9}$$

where j is the index of sum over the bands, i the index of the rotational transition, Δ^L and Δ^D are the homogeneous (collisional) and inhomogeneous (Doppler) broadening factors and $S_{i,j}$ is the oscillator strength. If we consider molecular absorption of a particular vibrational band, consisting of N ro-vibrational transitions with line strengths for given temperature S_i and wavenumbers ν_i, spontaneous transition rate for each line is:

$$A_i = \frac{S_i}{\nu * (1 - e^{\frac{Kc\nu_i}{KT}})} \tag{4.10}$$

For the entire band, the total probability is:

$$As = \sum_i A_i \tag{4.11}$$

and the mean line Full Width Half Maximum (FWHM) of the band is defined as the reciprocal of the mean lifetime, τ_0, of the state and given by:

$$\Delta^L = \frac{1}{N}\sum_i \Delta_i^L = \tau_0^{-1} \tag{4.12}$$

The interference profile of the band is described by the function:

$$F_T(\nu) = \frac{1}{\pi} Re\left(\frac{U(\nu)}{1 - \frac{\tau_0^{-1} U(\nu)}{A_s}}\right) \tag{4.13}$$

where U is a complex function defined as:

$$U(\nu) = \sum_i \frac{A_i}{\tau_0 + i * (\nu - \nu_i)} \tag{4.14}$$

where "i" is the imaginary unit and A_i is the spontaneous transition rate.
The unperturbed collisional form factor is:

$$F_L(\nu) = \frac{1}{\pi}\sum_i \frac{A_i * \tau_i}{\tau_i^2 + (\nu - \nu_i)^2} \tag{4.15}$$

The mean reorganized form factor in the strong collisions approximation can be expressed as:

$$F(\nu) = \frac{1}{\pi}\sum_i \frac{A_i \tau_0 (1 - \frac{A_i}{As})}{\tau_0^2 (1 - \frac{A_i}{As})^2 + (\nu - \nu_i)^2} \tag{4.16}$$

Finally, using the function 4.14 and 4.13, we obtain the net absorption coefficient normalized respect to the unperturbed form function:

$$k(\nu) = \frac{F_L(\nu) * F_T(\nu) * \nu}{F(\nu)} (1 - e^{\frac{Kc\nu}{KT}}) \tag{4.17}$$

The absorption coefficient of a molecular gas is then obtained by adding absorption values caused by all vibrational bands. Not only bands falling into considered spectral range should be taken into account, but also bands whose centers are far apart. Note that in this approach, individual lines are no longer considered separately, instead, the whole band obeys its own shape. We have to remember that at normal pressures and temperatures, the band profile converges to the classical Lorentz form factor.

4.2.2 Far Wings approximation

As just said in section 4.2.1, under extreme conditions the perfect gas approximation falls and also the broadening of spectral lines is different from the ordinary Lorentz contour. The interference of molecular states is the basic physical effect determining absorption in very dense gases. Also, the main contribution to the absorption is provided by transition between the unperturbed energy levels of an isolated molecule and that the line broadening is formed due to intermolecular collisional interaction. According to the "Tomsk model" [38], we assume that far wing profile is formed in dense collisions and is determined by the rapidly growing region of the potential of the intermolecular interaction. The dependence of form-factor on thermodynamic conditions is determined by a classical statistical problem. Now, let us consider an isolated spectral line at a frequency ν_0, the entire spectral interval is divided into four regions. The Voigt shape is assumed for the inner region, while for the other parts of the band, the line shape is described by the relationship:

$$f = \frac{D_s * \delta * \omega}{R_s(\omega - \omega_0)^{(1+\frac{3}{A_s})}} \int_0^{R_s} \frac{exp(-\epsilon((\frac{\sigma}{r})^{12} - (\frac{\sigma}{r})^6)\frac{hc}{KT}}{\sqrt{R_s^2 - r^2}} r dr \tag{4.18}$$

where

$$R_s = \frac{C_s}{(\omega - \omega_0)^{\frac{1}{A_s}}} \tag{4.19}$$

the constants A_s, C_s and D_s parameterize all quantum-mechanical effects and do not depend on thermodynamical conditions. The important parameters are also ϵ and σ, which occur in the expression for the Lennard Jones potential [39] of the intermolecular interaction and vary with temperature. In particular, ϵ is the depth of the potential well and σ is the finite distance at which the inter-particle potential is zero. The model line profile is schematically shows in figure 4.1.

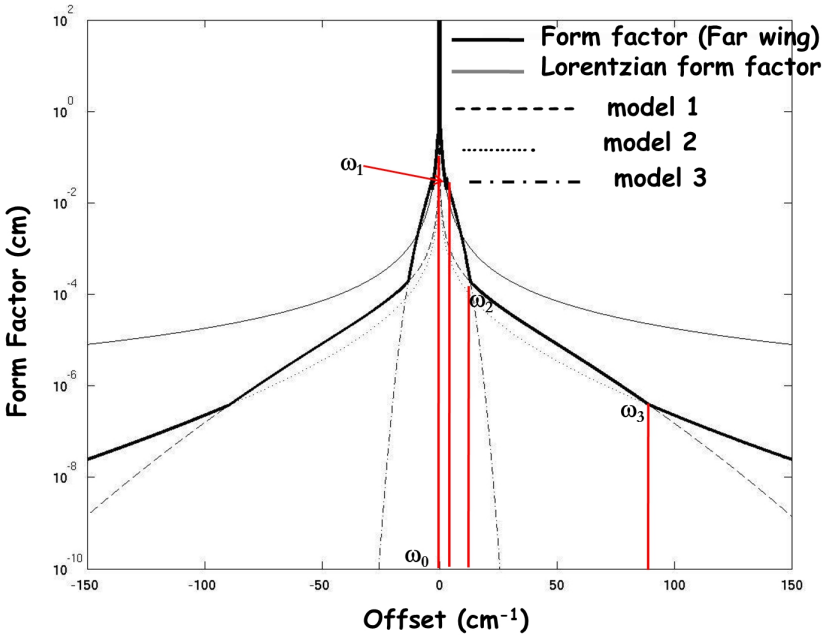

Figure 4.1: *Model spectral line profile*

The most important parameters, necessary to draw the line profile, are the boundaries ω_1,ω_2 and ω_3 of the regions where the behavior of the form factor changes. These values are determined by the condition that the approximation by form factor

corresponding to the next spectral region lies higher than the approximation by the form factor corresponding to the previous region. Thus, ω_1 is an offset from the line center at which equation 4.2.2 for the first region gives the contour higher than the Voigt profile of the central part of the line; ω_2 is the offset at which the second region is higher than the first one and so on.

In order to calculate the shape profile, one needs to know some constants and parameters that depend only on the temperature and pressure.

In table 4.1 and 4.2, values of free parameters and Lennard-Jones constants that we used to obtain synthetics spectra are reported.

Parameter	ω (cm^{-1})	A_s	D_s	C_s
1° range	0.1-3.0	5	0.2	6.5487
2° range	7	8	0.015	6.722
3° range	30	16	0.0053	5.0396

Table 4.1: *Free parameters needed to obtain the synthetic spectra. Values refer to the CO_2 band at 4.3 μm [38]*

Temperature (K)	ϵ	σ
193.0	904.82	3.8940
218.0	859.60	3.9201
296.0	760.00	4.0030
414.0	699.10	4.0945
534.0	718.70	4.1440
540.0	560.70	4.2000
627.0	686.50	4.2185
751.0	682.90	4.2219
920.0	479.90	4.4075

Table 4.2: *CO_2 intermolecular interaction parameters versus temperature*

4.3 LMM model

The present theoretical approach for the calculation of CO_2 absorption coefficients is similar to that used in [40] where more detailed description of the model can be found. The model accounts for the lines interferences due to inter-molecular collisions (or line-mixing), which have a very important influence on the spectral shape, as showen for various systems [41]. Assuming the impact approximation, the absorption coefficient at wave number σ of CO_2 at density N_{CO_2}, due to dipole allowed transitions and accounting for line-mixing (LM) effects is given by:

$$\begin{aligned} \alpha^{LM}(\sigma, N_{CO_2}, T) = N_{CO_2} \frac{8\pi^2\sigma}{3hc} \left[1 - exp\left(-\frac{hc\sigma}{k_b T}\right)\right] \\ \sum_l \sum_k \rho_l(T) d_l d_k Im\left\{\langle\langle l \left\| [\Sigma - L_0 - iN_{CO_2} W(T)]^{-1} \right\| k\rangle\rangle\right\} \end{aligned} \tag{4.20}$$

In this equation, we neglect Doppler effects and the influence of mean velocity and velocity changes induced by collisions. The sums extend over all CO_2 absorption lines l and k; ρ_l and d_l are the relative population of the initial level and the dipole matrix element of line l. Σ,L_0 and W are operators in the Liouville (line) space and $\langle\langle l\|....\|k\rangle\rangle$ designate a matrix element. Σ, L_0 are diagonal and associated with the current wave number and the line position according to this relation:

$$\langle\langle k\|\Sigma\|l\rangle\rangle = \sigma * \delta_{l,k} \text{ and } \langle\langle k\|L_0\|l\rangle\rangle = \sigma_l * \delta_{l,k} \tag{4.21}$$

All the influence of collisions on the spectral shape is contained in the frequency independent relaxation operator W(T), which depends on the considered band and on temperature. Its off-diagonal elements account for interferences between absorption lines, whereas the diagonal terms are the pressure broadening γ_l and shifting δ_l

coefficients of isolates lines, i.e.:

$$\langle\langle l\|W(T)\|l\rangle\rangle = \gamma_l(T) - i\delta_l(T) \tag{4.22}$$

Recall that W satisfies two fundamental properties that are the detailed balance principle:

$$\langle\langle k\|W(T)\|l\rangle\rangle * \rho_l(T) = \langle\langle l\|W(T)\|k\rangle\rangle * \rho_k(T) \tag{4.23}$$

and the sum rule:

$$\sum_l d_k\langle\langle k\|W(T)\|l\rangle\rangle = 0 \text{ i.e} \sum_{k=l} \frac{d_k}{d_l} Re\langle\langle k\|W(T)\|l\rangle\rangle = -\gamma_l(T) \tag{4.24}$$

When line-mixing is neglected, W is diagonal and the usual sum of Lorentzian line contributions is obtained as shown:

$$\alpha^{NoLM}(\sigma, N_{CO_2}, T) = N_{CO_2}^2 * \sum_l \frac{\sigma}{\sigma_l} \frac{S_l(T)\gamma_l(T)}{\pi[\sigma - \sigma_l - N_{CO_2}\delta_l(T)]^2 + [N_{CO_2}\gamma_l(T)]^2} \tag{4.25}$$

where S_l is the integrated intensity of line l and is given by:

$$S_l(T) = \frac{8\pi^3}{3hc}\sigma_l[1 - exp(\frac{-hc\sigma_l}{k_bT})]\rho_l(T)d_l^2 \tag{4.26}$$

4.3.1 Relaxation matrix

The model used in the present work to calculate the relaxation matrix W(T) is the same than that used in previous works devoted to the CO_2/air system [40] and [42] where a detailed description of the model can be found. Within this approach, the relaxation matrix is modelled by the energy corrected sudden scaling law, firstly

introduced by De Pristo and co-workers [43]. Note that line-mixing between lines of different vibrational bands being very small, only interference between lines of the same band is accounted for. The relaxation matrix element describing interference between two lines of a given vibrational band is given by:

$$\langle\langle j_i j_f \| W(T) \| j'_i j'_f \rangle\rangle = (-1)^{l_{2i}+l_{2f}}(2j_i+1)\sqrt{(2j'_f+1)(2j_f+1)}$$
$$\sum_{L_{even}} \begin{pmatrix} j'_i & L & j_i \\ l_{2i} & 0 & -l_{2i} \end{pmatrix} \begin{pmatrix} j'_f & L & j_f \\ -l_{2f} & 0 & l_{2f} \end{pmatrix} \begin{Bmatrix} j'_i & j'_f & 1 \\ j_f & j'_f & L \end{Bmatrix} (2L+1)\frac{\Omega(j_i,T}{\Omega(L,T)}Q(L,T) \tag{4.27}$$

In this expression, j_i, j_f and j'_i, j'_f are the rotational angular momentum quantum number of the initial and final levels of the line l and k, respectively; l_2 is the vibrational angular quantum number. The element matrix inside ( ) and {} are 3J and 6J coefficients [44]. Ω is the adiabacity factor, introduced into the model in order to account for energy corrections and given by

$$\Omega(j,T) = \left\{1 + \frac{1}{24}\left[\frac{\omega_{j,j-2}d_c}{\overline{\nu}(T)}\right]^2\right\}^{-2} \tag{4.28}$$

where $\omega j, j-2$, $\overline{\nu}(T)$ and d_c are the frequency spacing between levels j and j-2, the mean relative velocity in CO_2-CO_2 collisions and the scaling length. The rotational cross sections (or the basic rates) Q(L,T) in eq.4.27 are modelled by the widely used exponential power law

$$Q(L,T) = A(T)[L(L+1)]^{-\lambda(T)}exp\left[-\beta(T)\frac{hc*E_L}{k_b*T}\right] \tag{4.29}$$

In this equation, E_L is the rotational energy of level L. The temperature (and perturbed) dependent quantities d_c, A, λ, β are the parameters of the model. These parameters can be deduced using the sum rule in equation 4.21 and through fits of measured line-broadening coefficients.

4.3.2 Imaginary part of W

The imaginary part of the off-diagonal elements play a role at elevated pressure, as shown in [45], [46]. Taking these imaginary elements into account in the calculation does not significantly change the shape of the band but leads to opposite spectral shifts of the P and R branches when line-mixing is very efficient. Imaginary off-diagonal coupling terms within branches were thus added. They verify the detailed balance principle, have opposite signs for R-R and P-P couplings and decrease with the line separation. Their values were computed, for all bands at all pressures and temperatures, from a single parameter which was adjusted from a high density spectrum at the region of the $2\nu_1 + \nu_3$ band.

4.3.3 Parameters needed to obtain absorption coefficients

The first data needed for the calculations are spectroscopic parameters of isolated lines. Their identification, lower state energy, position, integrated intensity and self-broadening coefficient were taken from the latest version of the HITRAN database [1]. Note that for the temperatures, pressures and path lengths considered in the present work, the use of the HITRAN database is sufficient. For higher temperatures and longer path lengths, one may need to use a more adapted database, such as the HITEMP database [2] and check the intensity cut-off criterion of the used database.

The temperature dependence of the self-broadening was assumed to be the same as that of the air-broadening. This approximation is quite good when comparing measured values in the 1.6 μm region for self- and air-broadened CO_2 [6], [47]. For the self- line-shifting coefficients, there is little data, except for measurements for the $2\nu_1 + \nu_3$, $3\nu_1 + \nu_3$ and $3\nu_3$ bands [6]-[48]. In order to build a line-shift data for all bands, the approach of [49] has been used. The line-shifting coefficient of any ro-vibrational line is thus written, as:

$$\begin{aligned} &\delta[(\nu_1 + \Delta\nu_1, \nu_2 + \Delta\nu_2, \nu_3 + \Delta\nu_3, J_f) \leftarrow (\nu_1, \nu_2\nu_3, Ji)] = \\ &(J_i - J_f)\delta_{rot}(|m|) + (a_1\Delta\nu_1 + a_2\Delta\nu_2 + a_3\Delta\nu_3)\delta_{vib}(|m|) \end{aligned} \tag{4.30}$$

where ν_1, ν_2, ν_3 are the vibrational quantum numbers; $\Delta\nu = \nu' - \nu''$ is the difference of vibrational quantum numbers between the higher and lower states. The a_1, a_2, a_3 parameters and $\delta_{rot}(|m|)$, $\delta_{vib}(|m|)$ functions have been fitted to data measured of the $2\nu_1$+ν_3, $3\nu_1$+ν_3 [50] and $3\nu_3$ [51] bands, assuming that $a_1 = 2a_2$. Note that the parameters of the present approach may be approximate since there are very few data for the $3\nu_3$ band [51]. New measurements of line shifts for pure CO_2 are thus needed in order to improve the accuracy of the a_1, a_2, a_3 parameters and $\delta_{rot}(|m|)$, $\delta_{vib}(|m|)$ functions. The second set of data needed are the parameters for the construction of the relaxation matrix W(T). Parameters d_c, A, λ, β have been determined using the sum rule 4.24. From these value, all off-diagonal elements of the relaxation matrix have been computed using equations 4.27 and 4.29, while the diagonal elements have been fixed to the values of the self -broadening. A re-normalization procedure is then applied in order to satisfy the detailed balance and the sum rule as described by [40].

Chapter 5

Results and Discussions

In this chapter the CO_2 absorption coefficients measured at typical conditions of the deep venusian atmosphere are shown. Comparisons between numerous measured spectra and simulations calculated using three different models will be presented in the second part of the chapter.

5.1 Experimental measurements

We recreate the same conditions found in the deep atmosphere of Venus as from the Venus International Reference Atmosphere (VIRA) [52], which includes the tables of the vertical structure of the venusian atmosphere. The VIRA model uses the following inputs:

- new data on the chemical composition obtained from ground based and Galileo observations of the near IR spectra of the Venus nightside emission. From VEGA 1, 2 UV in situ spectrometry, Venera 15 infrared spectrometry; reanalysis of Venera 11,13,14 spectrometry; Pioneer Venus entry probes and Orbiter

InfraRed sounding (OIR) data,

- vertical temperature and pressure profiles obtained from the VEGA 2 entry probes, IR thermal sounding (Venera 15, Galileo), and from radio-occultation (Venera 15,16, Pioneer Venus and Magellan Orbiters), horizontal T-profiles from the VEGA 1,2 balloons,

- winds and turbulence measurements on the balloons, thermal winds retrieved from T-profiles (Venera 15, Galileo);

- new data on the variability of the cloud structure (Venera 15 IR-spectrometry, VEGA 1,2 entry probes and NIMS observations during the Galileo Venus fly-by)

In order to reproduce the real vertical TP profile, we varied the pressure and temperature of the CO_2 from 1 to 30 bar and from 294 to 650 K respectively. This corresponds to an altitude from about 50 km down to 15 km, as shown in figure 5.1.

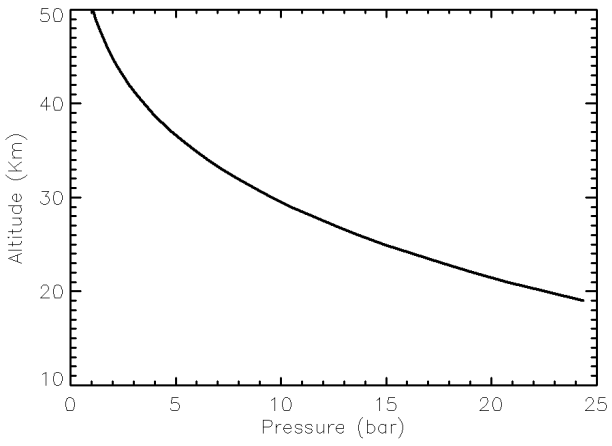

Figure 5.1: *Real vertical profile of the deep atmosphere of Venus used to obtain the CO_2 absorption coefficients .*

Detectors	Beam splitter	Source	Spectral range	Resolution	Number of scans
MCT	KBr	MIR	800-6000 cm^{-1}	2 cm^{-1}	150
InGaAs	CaF_2	NIR	6000-10000 cm^{-1}	2 cm^{-1}	50
Acquisition parameters					
Apodization function			Blackman-Harris		
Phase correction			Mertz		
Zero Filling			2		
Acquisition Mode			Double Sides		

Table 5.1: *Experimental parameters used for each spectrum acquired.*

For the spectral range (6000-10000) cm^{-1} we used the Tungsten lamp, the CaF_2 beam splitter and the InGaAs detector, while the Globar source, the KBr beam splitter and the MCT detector were employed from 750 to 6000 cm^{-1}. All parameters that we used for each acquired spectrum are summarized in the table 5.1.

As mentioned in chapter 3, each spectrum was recorded by a Fourier Transformer InfraRed (FT-IR) interferometer and a special gas cell, integrated inside the sample compartment.

In figures 5.2, 5.3, 5.4 the experimental absorption coefficients of the CO_2 recorded at different pressures and temperatures as from the VIRA vertical profile are shown.

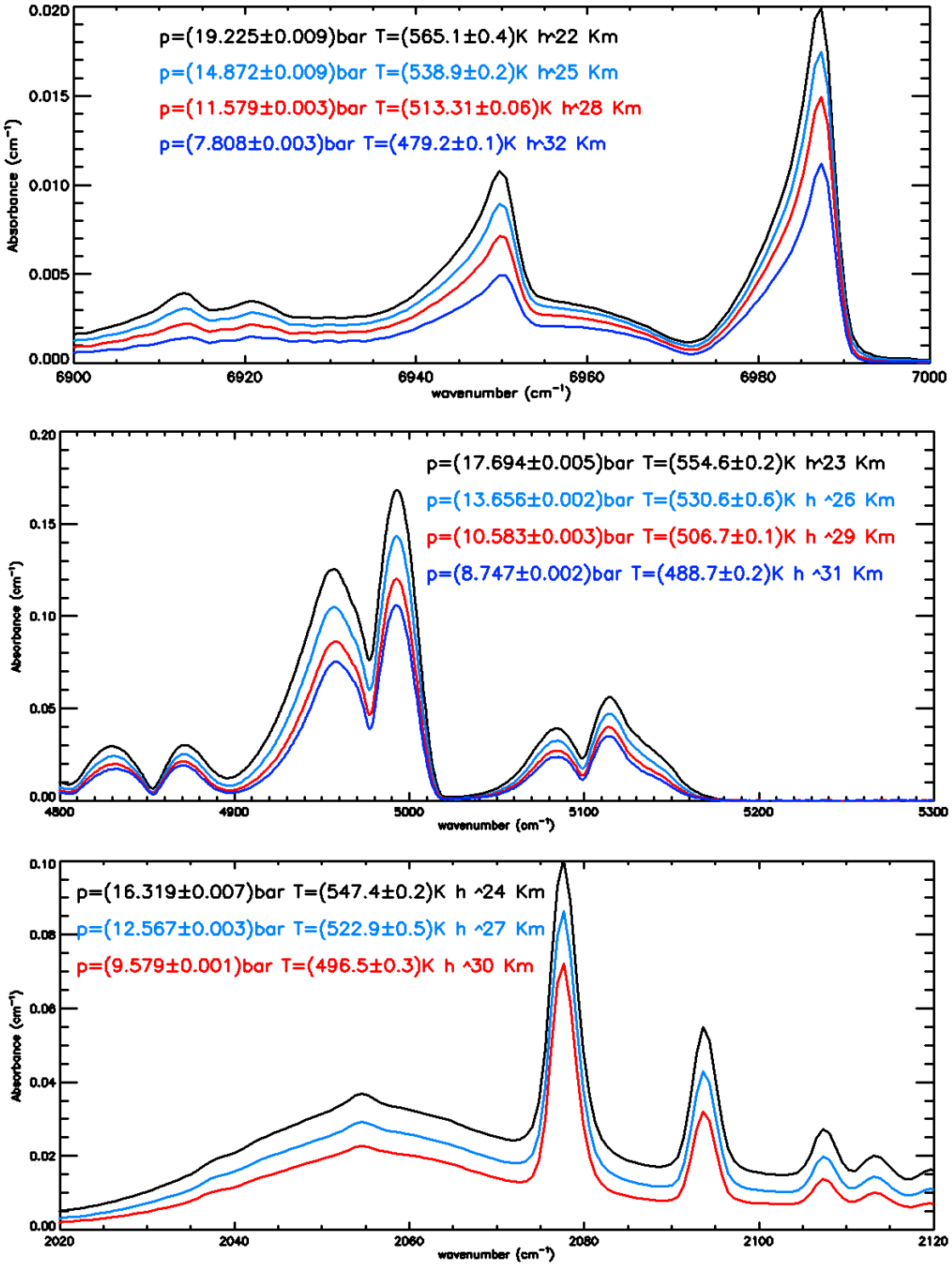

Figure 5.2: *CO_2 absorption coefficients at different pressures and temperatures. These physical conditions correspond to an altitude of 32 km down to 22 km.*

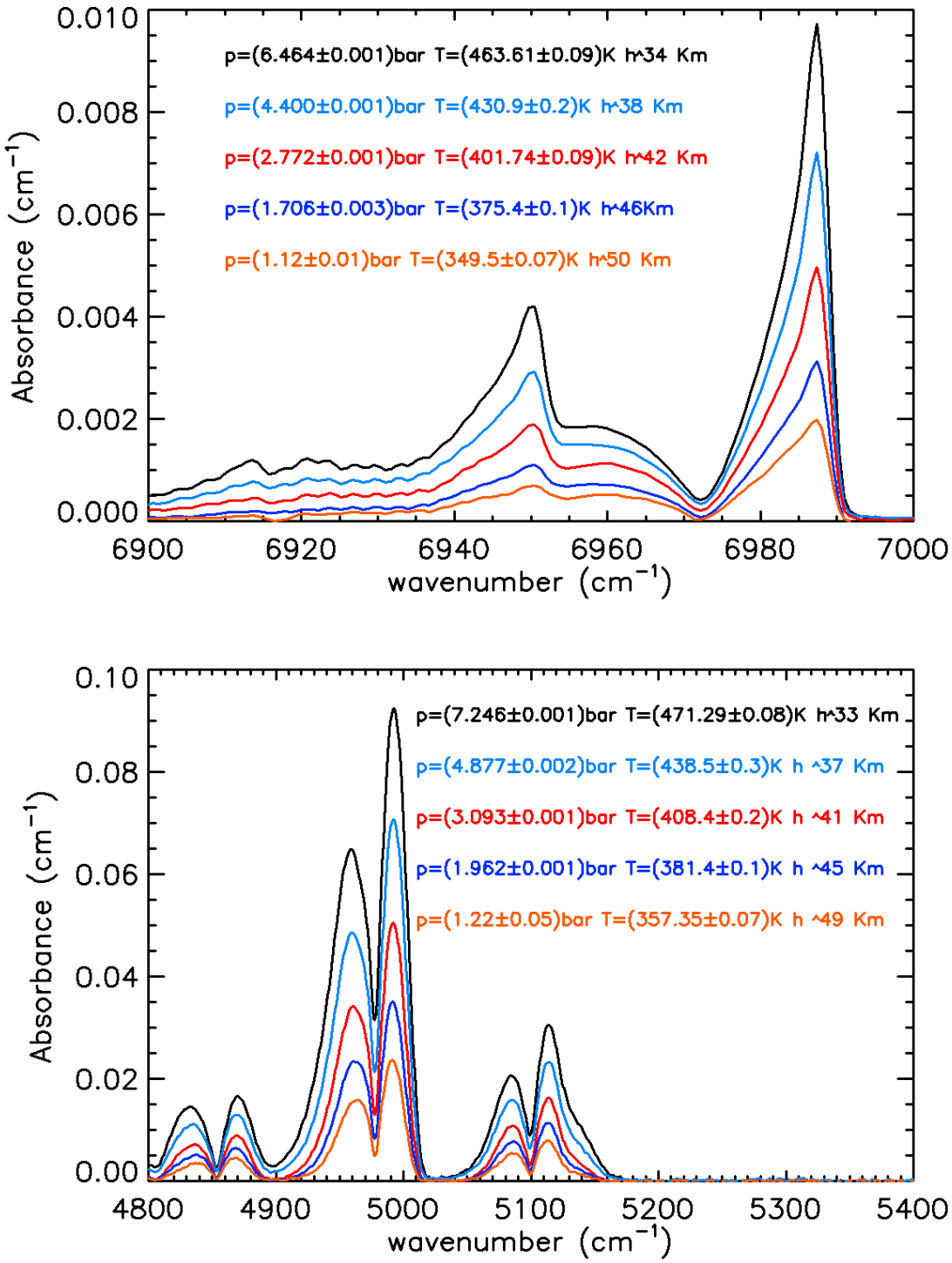

Figure 5.3: *CO_2 absorption coefficients at different pressures and temperatures. These physical conditions correspond to an altitude of 50 km down to 33 km.*

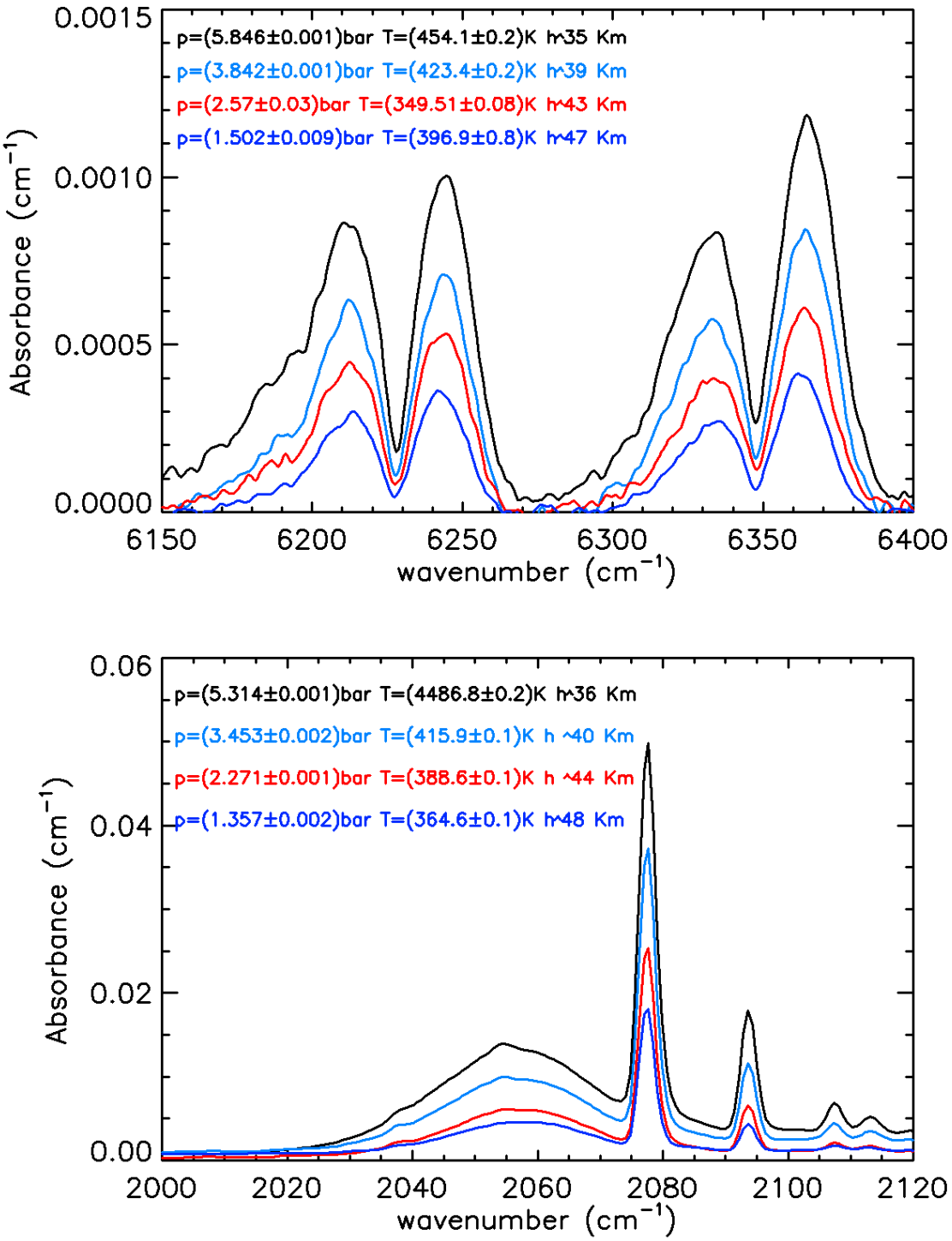

Figure 5.4: *CO_2 absorption coefficients at different pressures and temperatures. These physical conditions correspond to an altitude of 48 km down to 35 km.*

For low pressures (see figure 5.3) and low temperature, we can distinguish the roto-vibrational structures, in the spectral range range [6850-7000] cm^{-1}. These vanish when we increase the pressure, because the collision line width increases with the density as the mean time between collisions decreases. It is due to the modification of molecular potentials, and hence to the energy levels, which take place during each emission or absorption process, and is caused by inelastic as well as elastic collisions between the molecule and the surrounding ones.

In first approximation, the shape of the line is still Lorentzian and the width is proportional to the pressure. In order to quantify this behavior, we have calculated the band integrated area in different spectral regions, and have plotted this values toward the pressure. As shown in figure 5.5, we obtain a linear fit (red curve) with residual fit better than 99%. In figure 5.5 (on bottom) we reported also a polynomial fit, because in this spectral range, the broadening of the CO_2 bands is due to the combined contribution of the pressure and Collision Induced Absorption (CIA), a phenomenon that will be described with more details in the section 5.3.

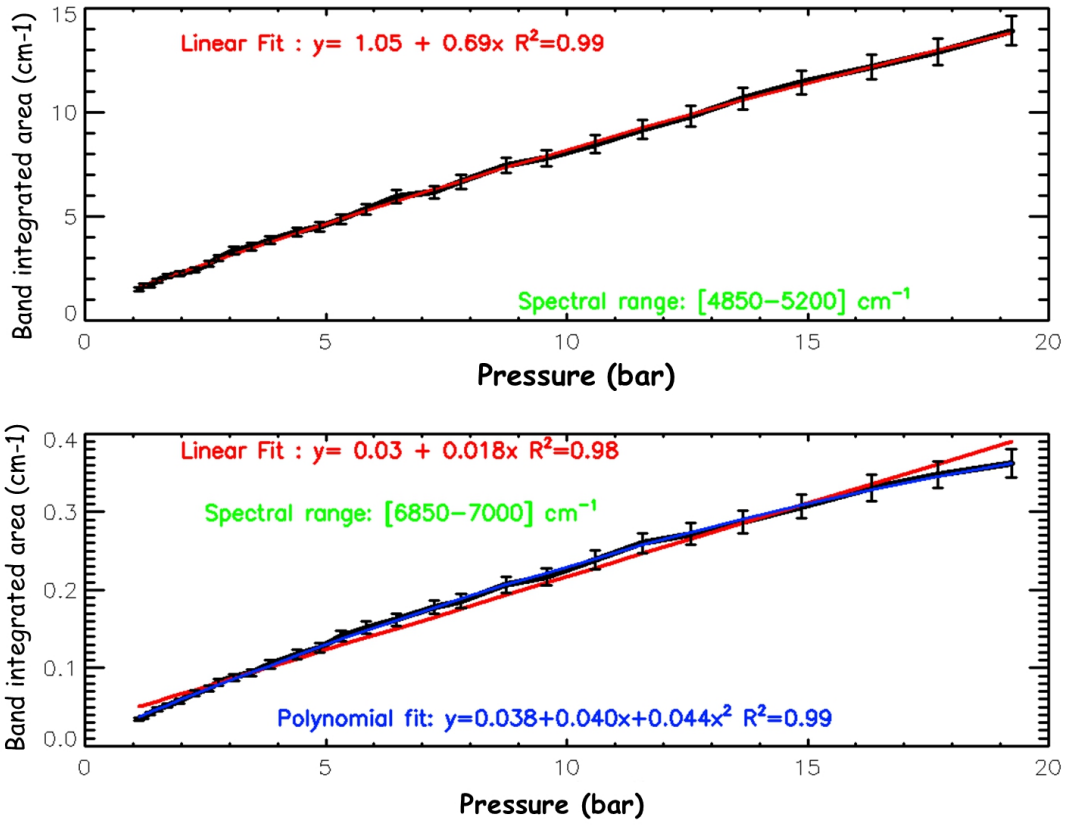

Figure 5.5: *Band integrated area vs pressure (black curve) and best fit (red curve)*

To get the largest number possible of CO_2 absorption coefficients, in order to test the radiative transfer data analysis, we created a grid by the original vertical profile. Initially we calculate, for each P and T value, the number density by solving the Van Der Waals equation, defined as:

$$\left[p + a\left(\frac{n}{V}\right)^2\right]\left(\frac{V}{n} - b\right) = RT \tag{5.1}$$

where a is a constant that provides a correction for the intermolecular forces and b provides a correction for finite molecular size. For the CO_2 we have [53]:

a= 3.96*10^{-1} (Pa m ^{3})

b= 42.69*10^{-6} (m^3mol^{-1})

Increasing and decreasing of 30°C the initial values of temperatures, maintaining the density of the CO_2 constant, we deduced in according to the equation 5.1, the new value of the pressures. In this way, we obtain two new "profiles" of temperature and pressure, as shown in the figure 5.6.

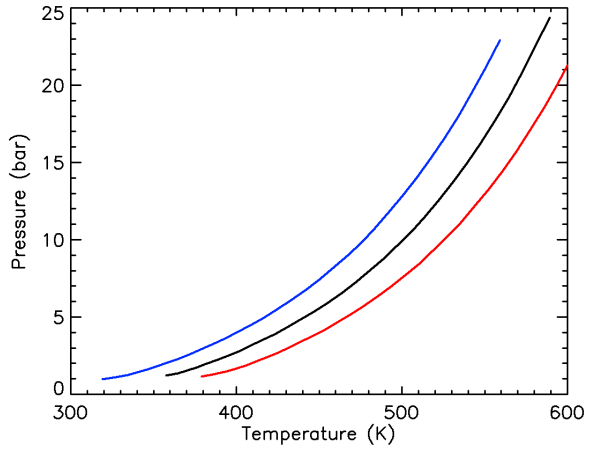

Figure 5.6: *The three profile along we recorded the CO_2 absorption coefficients. The black curve is the real vertical profile, the blue is obtained decreasing the T of 30° C and the red is obtained increasing the T of 30° C.*

For each point of this grid, we obtained the CO_2 absorption coefficients, acquired in the spectral range from 700 to 10000 cm^{-1} and with the same experimental parameters, i.e resolution 2 cm^{-1}, number scans 150.

Measurements errors

There are two potential sources for photometric error in Fourier Transformer InfraRed interferometer: one is due to the linearity and the second one to the "single beam".

The first one and most critical source of photometric error is the non-linear photometric response of the detector and possibly its associated electronics. This effect may occur as a distortion of the spectrum, but in our case we have never encountered such anomaly. Therefore we can say that this source of error can be neglected. The single beam is only a problem if there is a significant change in the system's response in the time frame from the acquisition of a reference to a sample spectrum. This might be due to drifts in the lamp used as source or change in the transmittance of the optical path due to atmospheric water vapour or carbon dioxide. Recording the reference spectrum at the same environmental conditions of the sample, is very important in order to remove, as much as possible, the contribution of the water vapour and CO_2, present along the optical path of the FT-IR off the cell. However, even small variation of the air conditions within the optical path translate into a not perfect compensation and consequently it's seen as a residual in the transmittance affecting the uncertainty. A way to reduce this error is a much as possible, is reduce the time interval between the reference and sample acquisition. For what has been said, we can assert that our measurements are affect by errors due to the drift of the system (lamps, air, detector etc). Therefore, in order to evaluate the uncertainty, we have recorded 10 CO_2 transmittances under the same conditions, calculated the average value, <Transmittance>, and its standard deviation σ. In all cases of interest, we have that the σ_T=**2%** of the spectral range. To obtain the final errors,

we must remember that the figures show the CO_2 absorption coefficients (see for example the figure 5.2); therefore, referring to the equation 3.2.2, and applying the propagation statistical errors rule, we have:

$$\sigma(Absorbance) = \sqrt{\left(\frac{\partial Absorbance}{\partial T}\right)^2 \sigma_T^2 + \left(\frac{\partial Absorbance}{\partial l}\right)^2 \sigma_l^2} \qquad (5.2)$$

The σ_l is not a statistical error but a measurement error. In figure 5.7, an example of the error calculated applying the equation 5.1is shown. In the bottom panel, we reported only the errors without absorption coefficients to show the entity of the errors.

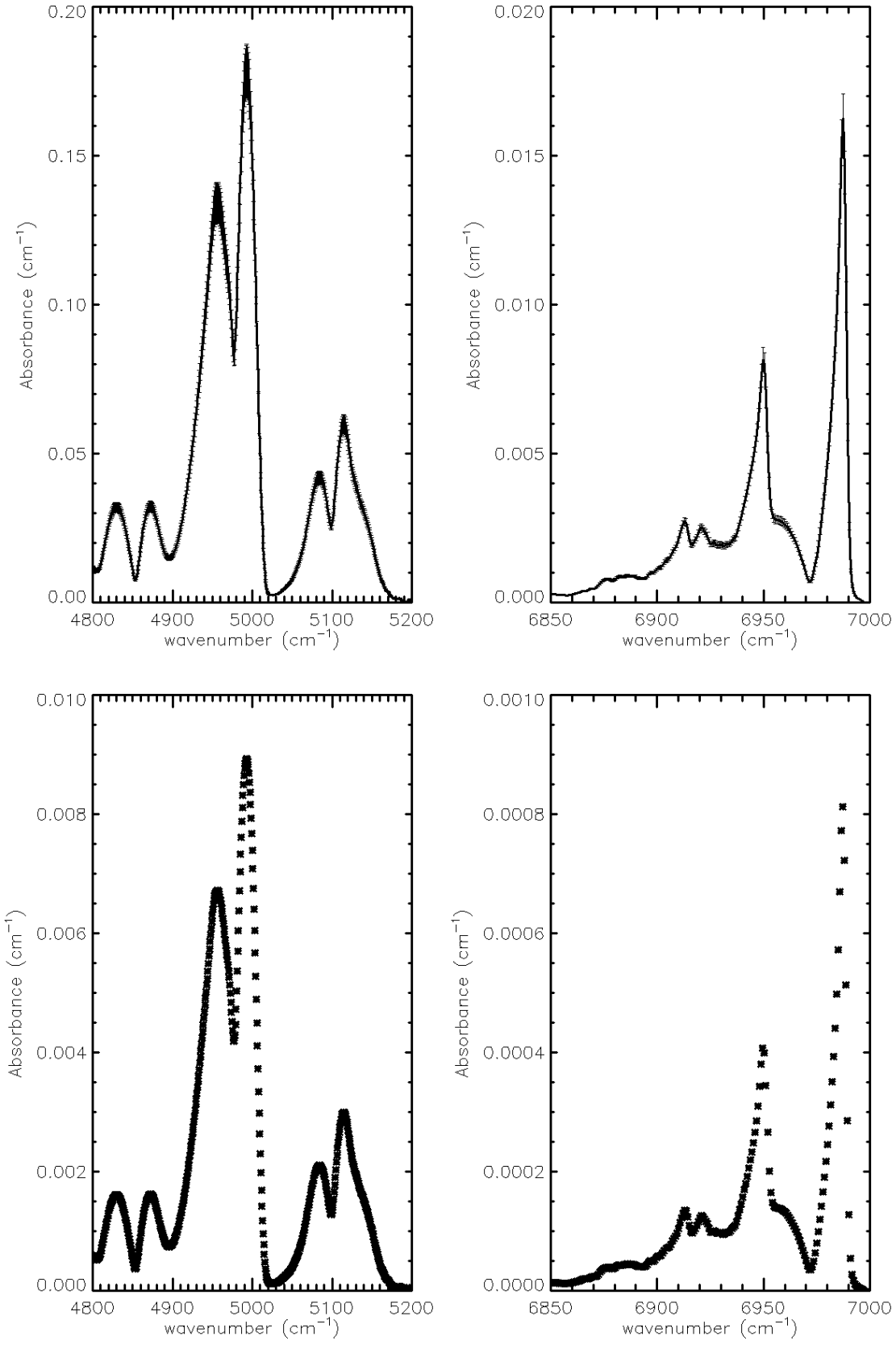

Figure 5.7: *CO_2 absorbtion coefficients at 19bar and T=561K (top on left) and P=13bar T=530K (top on right). The error bar corresponds to the statistical errors calculated by 5.1. In the bottom panel, we report only the errors.*

5.2 Comparison between simulated and measured data

The measurements have been compared with synthetic spectra obtained from the three different models described in chapter 4. The figure 5.8 shows results obtained for the $3\nu_1+\nu 3$ tetrad region at room temperature and 20bar.

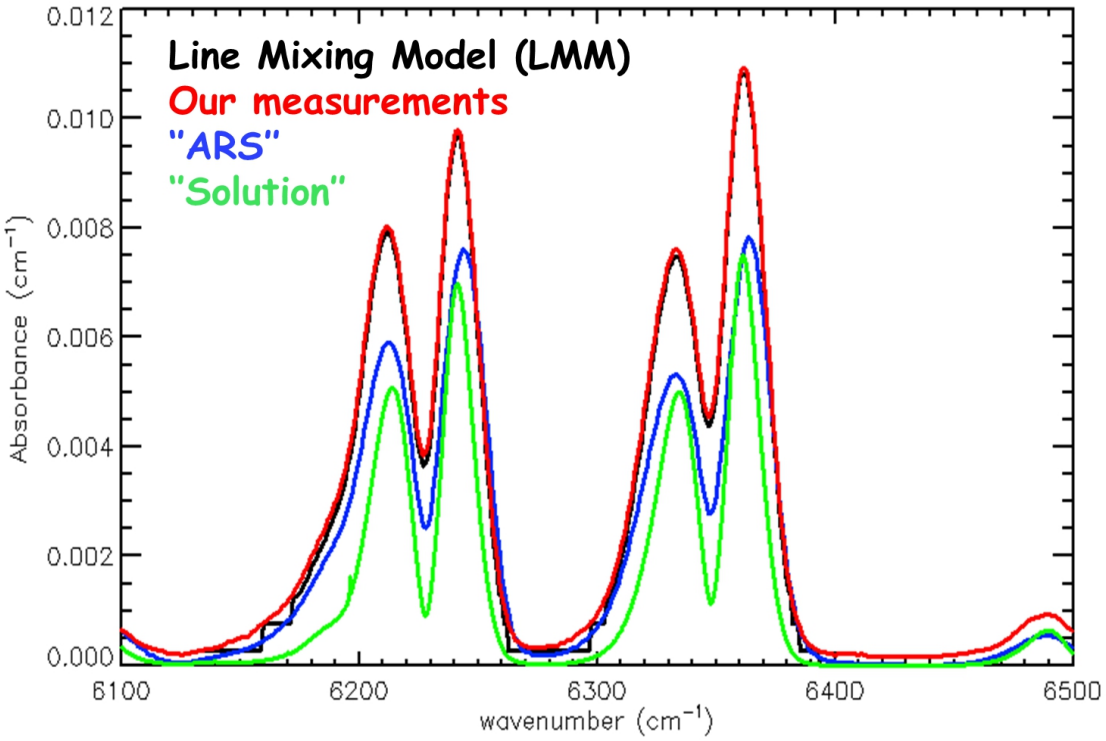

Figure 5.8: *Comparison between measured (red curve) and simulated spectra of CO_2 at room temperature and 20 bar. The black curve is obtained by LMM, the green and blue curves are obtained by Solution and by ARS code respectively.*

These results confirm that Lorentz line shapes are not a good approximation at high pressure and it's necessary take into account the line mixing effect. In fact, as you can see in figure, the blue curve, obtained by ARS code which neglects this effect,

underestimates the absorption in the central part of the band. The same behavior is obtained with Solution code (green curve), which considers the line mixing effect but its models the line shape according to figure 4.1. The differences between spectra simulated using the three different models and measured increase with pressure and temperature, as you can see in figure 5.9.

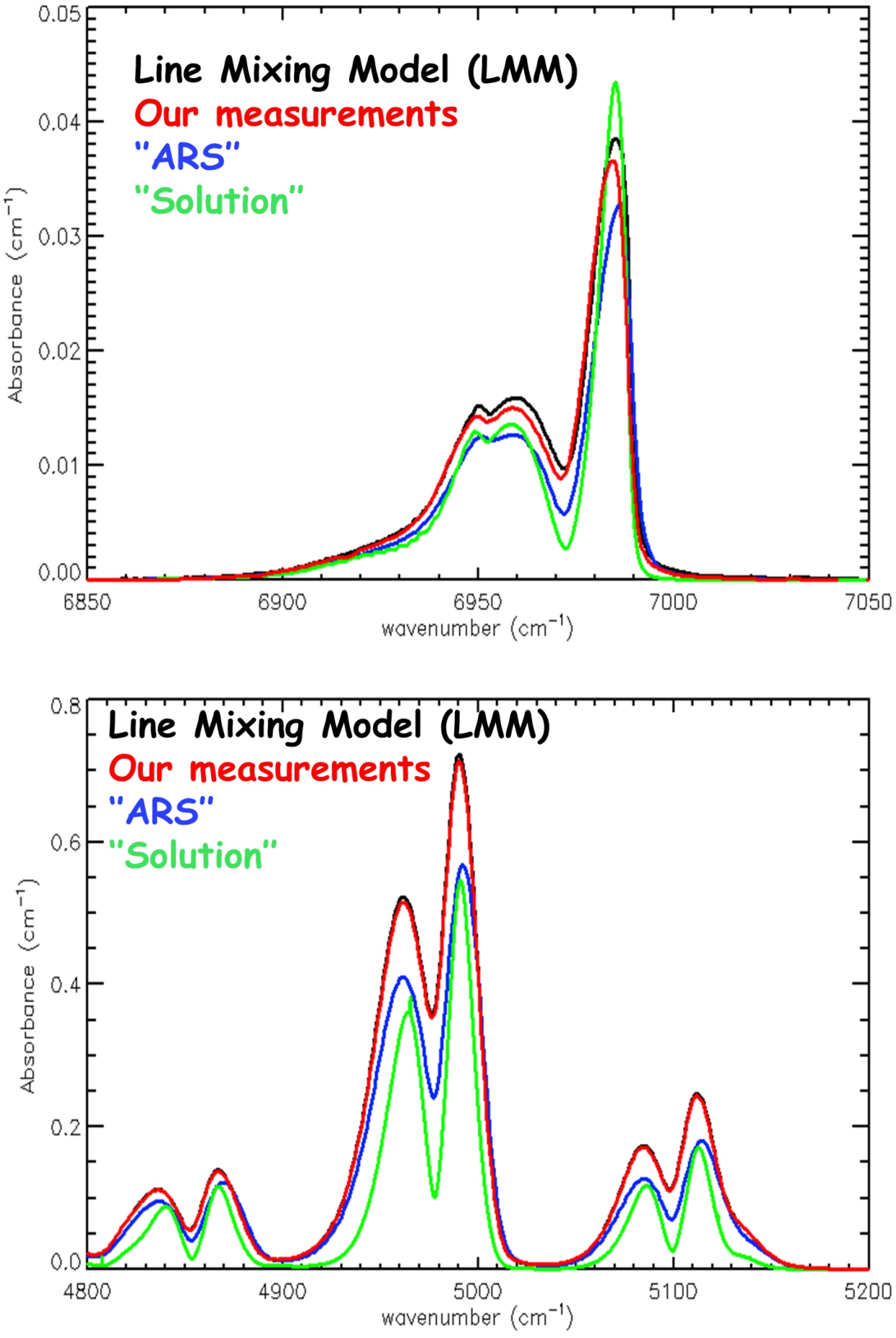

Figure 5.9: *Comparison between measured (red curve) and simulated spectra of CO_2 at 20 bar and 373 K (on top) and 40 bar 473 K (on bottom). The black curve obtained by line LMM, the green and blue curves are obtained by Solution and ARS code respectively.*

In order to quantify the matching between simulated and measured spectra, we calculated the integrated band area in different spectral range and evaluated the difference between experimental and synthetic spectra. We have chosen this method in order to estimate the goodness of the models, because it allows us to evaluate with greater accuracy also the less intense absorptions. Moreover, as shown in figure, we can select every range of interest carefully.

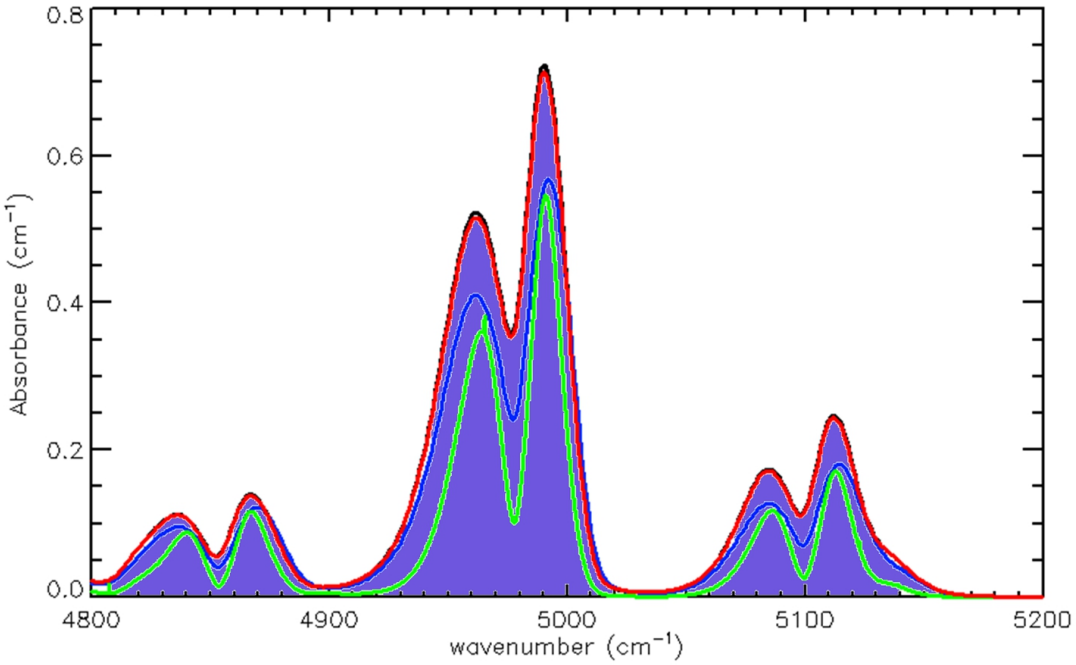

Figure 5.10: *Example of the band integrated area method. A straight line is drawn between the two frequency limits and the area is calculated.*

Results are reported in table 5.2. As you can see we have the match fit with the "LMM" on all the measured spectral ranges, in fact differences between our data and synthetic spectra are smaller respect to the other models.

$\frac{\Delta(M-LMM)}{LMM}$	$\frac{\Delta(M-Sol)}{Sol}$	$\frac{\Delta(M-ARS)}{ARS}$	Spectral Range cm^{-1}	p (bar) T (K)
0.03	0.3	0.08	2115-2025	10 bar 294 K
0.004	0.4	0.2	7050-6880	20 bar 294 K
0.02	0.6	0.5	8350-8150	40 bar 294 K
$9.2*10^{-4}$	0.1	0.2	4800-5200	40bar 373 K
0.06	0.3	0.3	6100-6500	40 bar 373 K
0.002	0.3	0.2	6850-7050	40 bar 373 K

Table 5.2: *Difference between integrated band area of the experimental and simulated spectra. M refer to the "measurements", LMM, Sol and ARS refer to "Line Mixing Model", Solution and ARS Code respectively.*

These results lead us to conclude that for gases under extreme conditions, the shape of the spectral lines no longer follows the conventional Lorentzian form and that it is mandatory to take into account the line mixing effect to reduce the discrepancy.

In the remainder of this chapter, we will then report only the results obtained using the mixing-line model, analyzing the far wings region. This part of the spectrum is very important to improve the remote sensing data analysis for better interpreter the data coming from the space missions, in particular from VIRTIS instrument on board of Venus Express mission.

Far wings region

Results obtained in the high frequency wing of the ν_2 and ν_3 bands for different temperatures are presented in figures 5.11 and 5.12 respectively. In this figure the normalized absorption was calculated in $cm^{-1}\text{Amagat}^{-2}$. Amagat is a practical unit of number density, defined as the number of ideal gas molecules per unit volume at 1 atm (= 101.325 kPa) and 0 °C (= 273.15 K) [54]. In order to have a comparison between simulated and measured data a low temperature, in figure 5.11 (panel a open circle), we show results at 258 K obtained by [55].

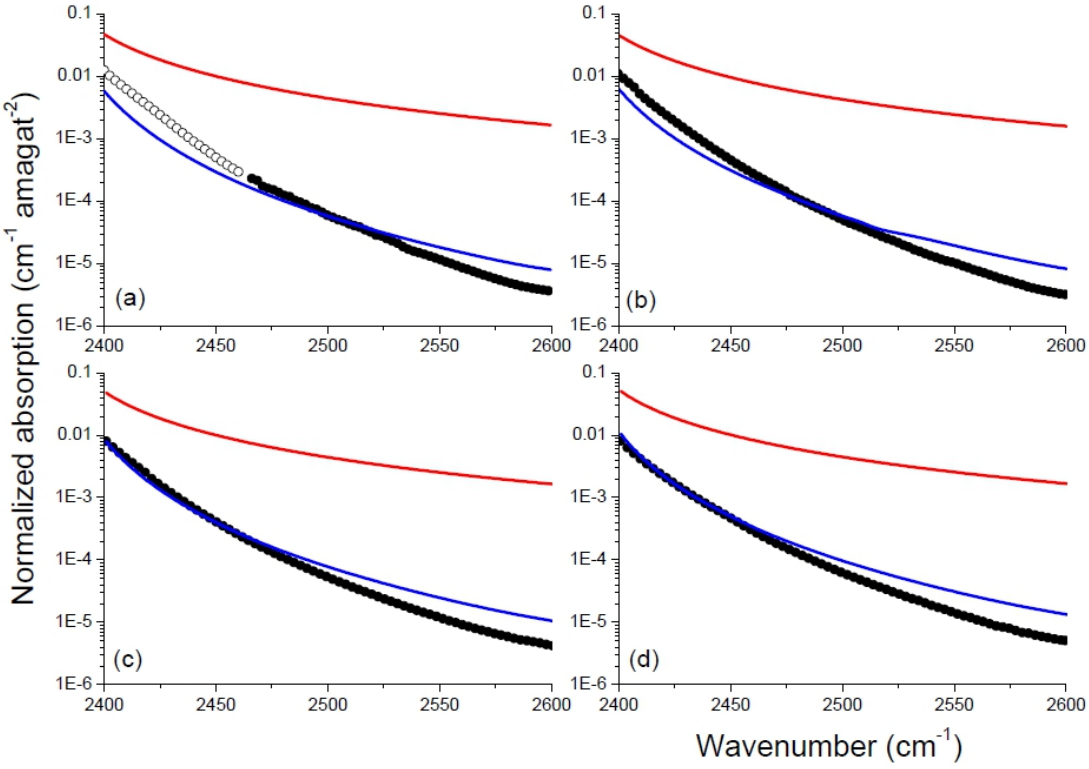

Figure 5.11: *Normalized absorption in the high-frequency wing of the ν_3 band region of pure CO_2 at (a) 260 K; (b) 296 K; (c) 373 K; (d) 473 K and N_{CO_2}=23 Amagat. (•) are the present measured values, blue and red curves are normalized absorptions calculated using our LMM and the Lorentz shape, respectively. Values in open circle in (a) are data measured at 258 K by [55] (on top)*

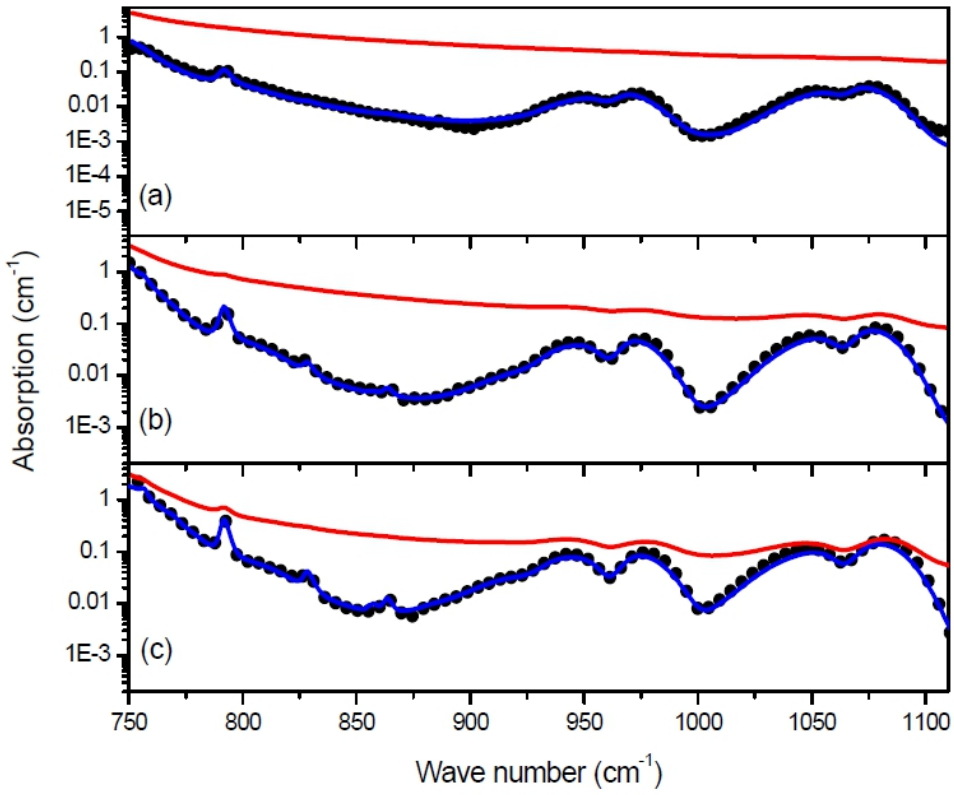

Figure 5.12: *Absorption in the high-frequency wing of the ν_2 band region of pure CO_2 for (a) T = 294 K,N_{CO_2}=51.28 Amagat; (b) T=373 K, N_{CO_2}=31.93 Amagat; (c) T=473 K, N_{CO_2}=23.63 Amagat. (•) are the experimental values, blue and red curves are absorptions calculated with and without taking into account line-mixing effects, respectively.*

As expected, Lorentzian line shapes strongly overestimate absorption in these regions. When the LMM is used, satisfactory agreement with measurements is obtained for the ν_2 band wing (5.11), contrary to the ν_3 band (5.12). In fact, in addition to the contribution of the ν_2 band wing, there are several allowed absorption bands centered at the considered region. Their local contributions, which are accurately calculated with the LMM is dominant, mask the eventual discrepancies in the modelling of the ν_2 wing. On the opposite, absorption in the high-frequency

side of the ν_3 band is almost entirely due to far wing of this band lines for which the impact approach breaks down. Similar results are obtained for the high-frequency wings of the $\nu_1+\nu_3$ and $2\nu_1+\nu_3$ bands.

For an accurate description of far wing contributions, the widely used empirical correction to the Lorentz line shape has thus been used. Within this approach, the absorption for pure CO_2 is expressed by:

$$\alpha^{wing}(\sigma, N_{CO_2}, T) = N_{CO_2} \sum_l exp\left[h\frac{(\sigma-\sigma_l}{2K_BT}\right]\frac{\sigma}{\sigma_l} * \frac{S_l(T)\gamma_l(T)}{\pi[\sigma-\sigma_l-N_{CO_2}\delta_l(T)]^2+[N_{CO_2}\gamma_l(T)]^2} * \chi(T,|\sigma-\sigma_l|) \tag{5.3}$$

The line shape correction factor χ is assumed independent of the transition. The exponential term in equation 5.3 is due to the initial correlations and results in an asymmetry of the far wing [56], [57]. A set of χ factors for pure CO_2 in the ν_3 band head region and for a wide range of temperature [220-750 K] was constructed in [58]. In [59] the high-frequency wings of the ν_3, $\nu_1+\nu_3$ and $3\nu_3$ bands were investigated at 296 and 431 K. Apart from these studies, most others are devoted to the ν_3 band and/or for room temperature. Note that, to our knowledge, no data are available for the ν_2 band wing despite its importance. In this work, three new sets of χ factors have been constructed for the ν_2, ν_3 and $\nu_1+\nu_3$ band wings by fitting measured data at different temperature through using equation 5.3.

The corresponding expressions of the χ factors are given in table 5.3:

χ(T,$\Delta\sigma$)	$\Delta\sigma$
1	$0<\Delta\sigma<\sigma_1$; σ_1=3 for ν_2, ν_3, $\nu_1+\nu_3$
Exp[-B_i(|$\Delta\sigma$|- σ_1)]	$\sigma_1<\Delta\sigma<\sigma_2$ σ_2=30 for ν_2, ν_3, $\sigma_2$3=150 for $\nu_1+\nu_3$
Exp[-B_1(σ_2-σ_1)-B_2(|$\Delta\sigma$|-σ_2)]	$\sigma_2<\Delta\sigma<\sigma_3$ σ_3=150 for ν_2, ν_3, σ_3=300 for $\nu_1+\nu_3$
Exp[-B_1(σ_2-σ_1)- B_2(σ_3-σ_2)-B_3(|$\Delta\sigma$|-σ_3)]	$\Delta\sigma>\sigma_3$

Table 5.3: *Analytical expression of χ factors*

The parameters B_i [see tab. 5.3] of the χ factors are modelled as function of temperature by the following analytical expression:

$$B_i(T) = \alpha_i + \beta_i exp(-\gamma_i T) \tag{5.4}$$

The values of α_i, β_i and γ_i have been deduced from measurements at the high frequency band wing for each region. For the ν_3 and ν_1+ν_3 bands regions, these parameters are fitted using respectively data in the 2400-2600 cm^{-1} and 3750-3950 cm^{-1} interval, and at five temperatures 230, 260, 295, 373 and 473 K. For the ν_2 region, measured data are available only for three temperatures 294, 373 and 474 K. However, as demonstrated at the beginning of this section, the line mixing impact approach accurately calculates the far wing of this region, hence absorption for other temperatures have been simulated using our model. The 750-950 cm^{-1} spectra region of these simulated data are used together with measured data in order to determine the χ factor parameters. The values of these parameters are reported in table 5.4.

The relationship 5.3 being valid for far wings, only absorption of the main band (ν_2,ν_3 and ν_1+ν_3) is calculated by this equation, the contributions of local weak

	ν_2 Band			ν_3 Band			$\nu_1 + \nu_3$ Band		
	α	β	γ	α	β	γ	α	β	γ
B_1	0.1034	1.962	0.0203	0.0727	-0.3830	0.0105	0.03	-0.3507	0.01804
B_2	0.0145	0	0	0.0229	0.1355	0.0109	0.0156	2174.3	0.0575
B_3	0.0099	0	0	0.0231	0	0	0.0082	0	0

Table 5.4: *Values of the χ factors parameters deduced from experiments.*

bands are calculated using the LMM as described in the section 4.3. A comparison between measured and calculated values for the ν_3 band wings regions is presented in figure 5.13 at 295 K and 473 K.

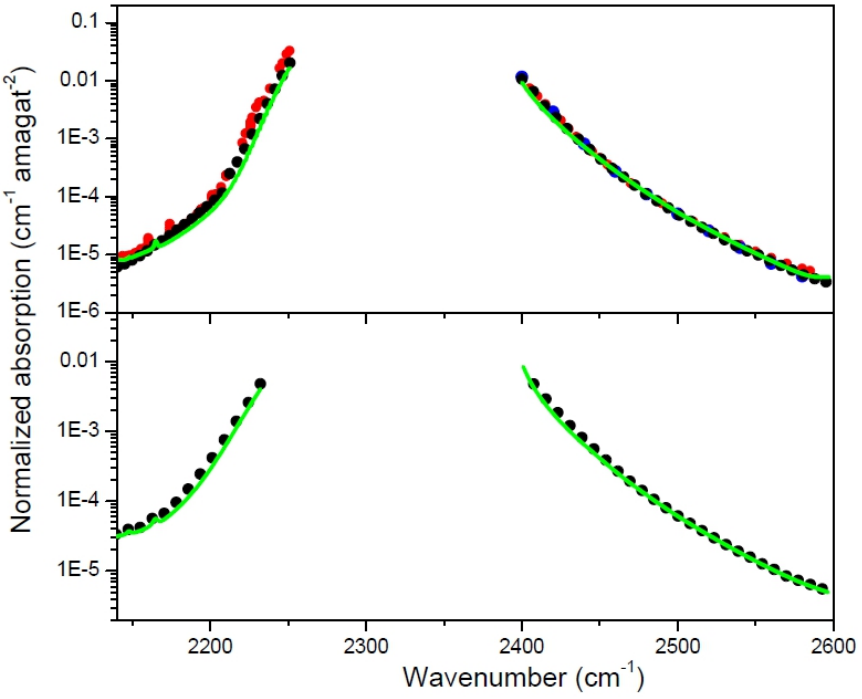

Figure 5.13: *Pure CO_2 normalized absorption coefficients at the ν_3 band wing regions for T = 295 K (top); T = 473 K (bottom) and N_{CO2}=17.6 Amagat. (•) and green curve are respectively measured and calculated values. Measured data at room temperature (top) of previous studies are also reported for comparison: the red dotted curve are values of [60] in the left and [55] in the right, the green dotted curve are values from [58]*

Note that accounting for the initial correlation [exponential term in equation 5.3]

allows an accurate description of both the low and high-frequency sides. Similar results are obtained for 230 K, 260 K and 373 K. Several tests show that using the present χ factors parameters leads to better agreements with measurements compared to results obtained using those of [58], which were determined using the spectroscopic parameters available in the 90's. In order to verify the consistency of the χ factors parameters, previously reported, a comparison between absorption calculated using the present χ factors parameters and measurements at a wider range of temperature has been performed. Comparison between calculated and measured spectra at various temperatures for the high-frequency wing region of the $\nu_1+\nu_3$ bands is presented in figure 5.14. A good agreement between measured data and calculated values is also obtained at the low-frequency side of these bands using the same set of χ factors. For other windows at higher wavenumber, the far wing could be measured only at room temperature, while measurements at other temperature are limited by our experimental conditions. This because, our gas cell is only 2 cm long and, to study this region of the spectrum it's necessary to reach very long optical path. Future measurements at various temperatures are thus needed in order to establish similar sets of χ factor for those regions.

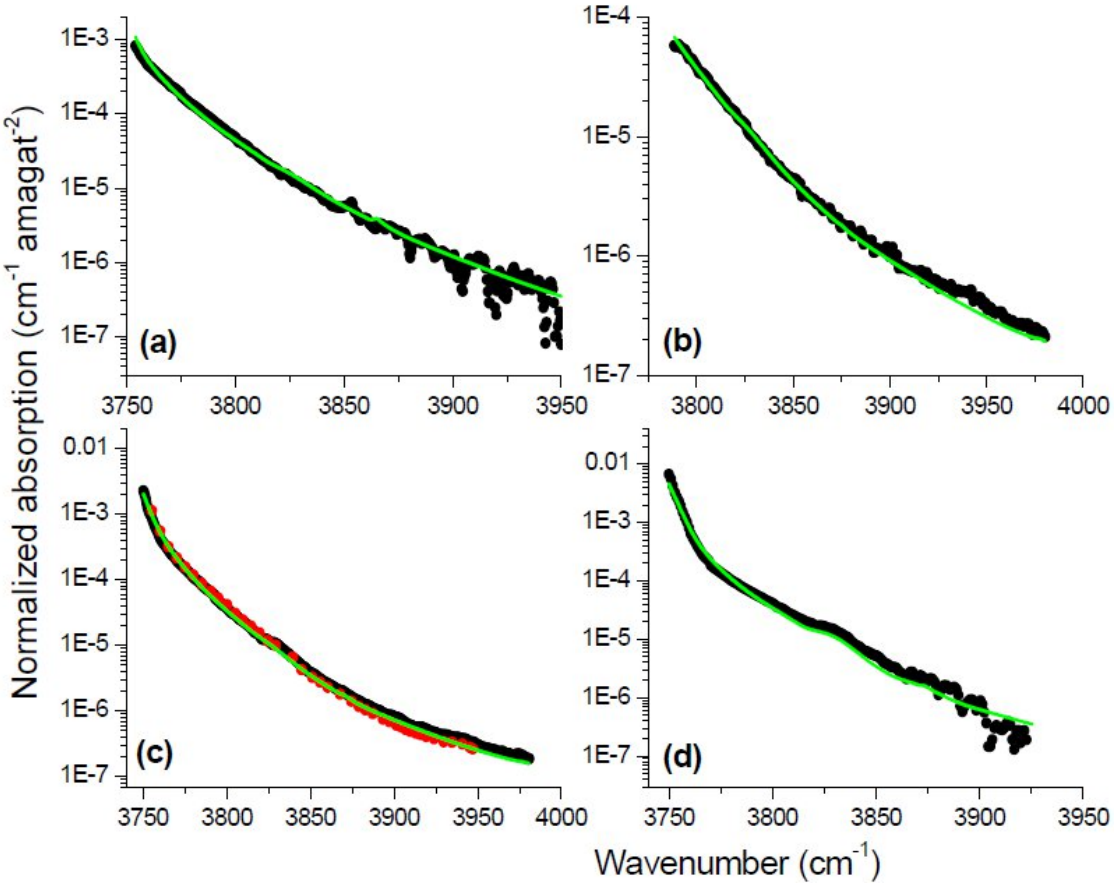

Figure 5.14: *Pure CO_2 normalized absorption coefficients at the high frequency wing side of the $\nu_1+\nu_3$ band for N_{CO_2}= 23 Amagat and (a) T = 230 K; (b) T=260 K; (c) T=295 K and (d) T =373 K. (•) and green curve are respectively measured and calculated values. At room temperature (c), data of [61] the dotted red curve is also reported for comparison.*

After an extensive discussion on the very good results obtained with the LMM, in figures 5.15, we show some comparison between our experimental data, measured as a from the VIRA profile and synthetic spectra obtained with this model. As you can see, the two curves superposed in all spectral range and at very different physical conditions. Also in this case, to test the goodness of the best fit between simulated and measured data, we calculated the band integrated area and the difference. As you can see in table 5.5, we have a matching better than 98% for most cases of interest.

Errors indicated in table 5.5 are statistical errors evaluated as standard deviation of the fluctuation of the pressure and temperature values during the acquisition of the spectra.

The values indicated with * refer to the comparison shown in figure 5.15.

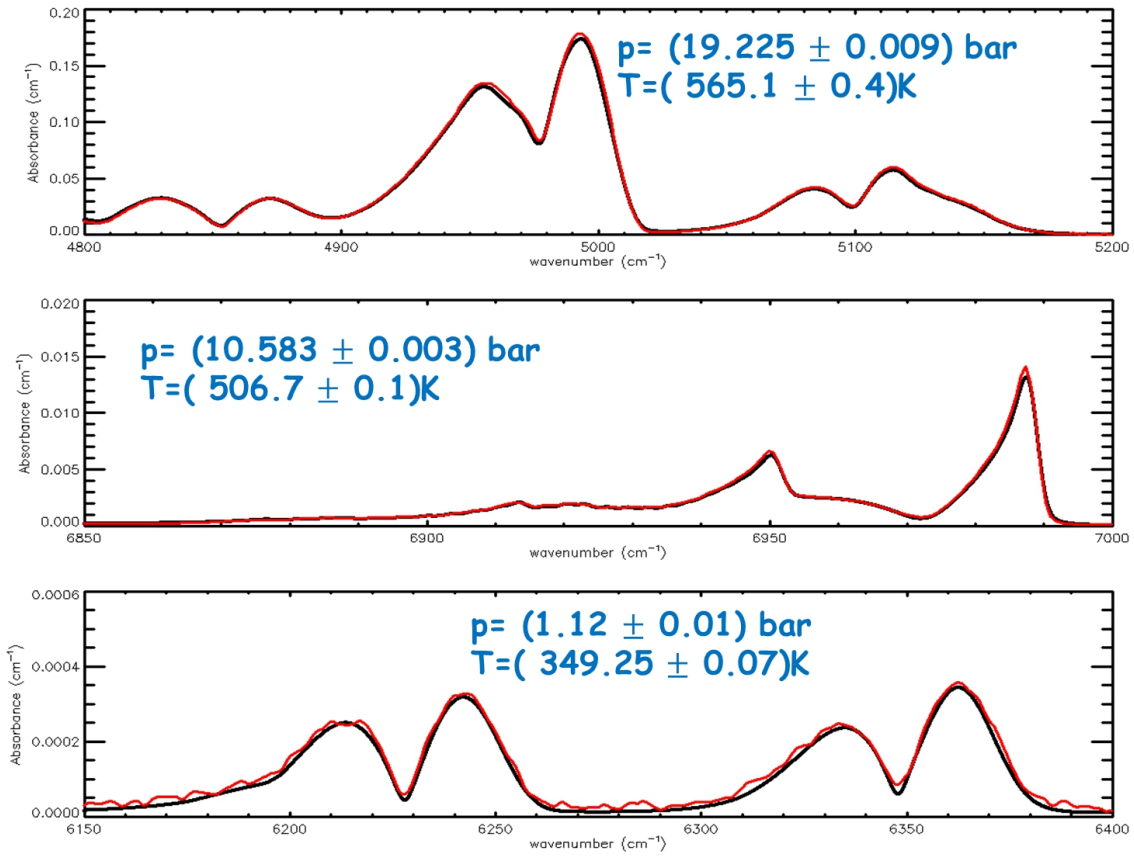

Figure 5.15: *Comparison between measured (red curve) and simulated (black curve) data by LMM.*

Spectral range 6850-7000 cm^{-1}				
Altitude (Km)	pressure (bar) Temperature (K)	M	LMM	$\frac{\Delta(M-LMM)}{LMM}$
50	1.12 ± 0.01 348.9 ± 0.6	0.0351	0.0336	0.04
47	1.502 ± 0.009 370.13 ± 0.04	0.0472	0.0459	0.03
46	1.708 ± 0.003 375.9 ± 0.2	0.052	0.0507	0.025
43	2.57 ± 0.03 395.3 ± 0.2	0.074	0.0698	0.06
42	2.772 ± 0.001 401.85 ± 0.08	0.082	0.0815	0.006
40	3.453 ± 0.002 415.4 ± 0.1	0.094	0.0936	0.004
38	4.400 ± 0.001 430.7 ± 0.1	0.118	0.0117	0.002
37	4.877 ± 0.002 438.9 ± 0.3	0.126	0.125	0.004
35	5.842 ± 0.001 455.1 ± 0.1	0.152	0.147	0.036
33	7.246 ± 0.001 471.3 ± 0.05	0.178	0.174	0.025
32	7.808 ± 0.003 478.3 ± 0.1	0.186	0.179	0.04
29	10.583 ± 0.003 506.3 ± 0.2	0.239	0.238	0.0002 *
27	12.567 ± 0.003 521.9 ± 0.1	0.272	0.257	0.06
26	13.656 ± 0.002 530.5 ± 0.1	0.287	0.286	0.001
24	16.319 ± 0.007 546.9 ± 0.4	0.331	0.329	0.004
22	19.225 ± 0.009 565.2 ± 0.4	0.362	0.361	0.002
Spectral range 4800-5200 cm^{-1}				
Altitude (Km)	pressure (bar) Temperature (K)	Measured	LMM	$\frac{\Delta(M-LMM)}{LMM}$
50	1.12 ± 0.01 348.9 ± 0.6	1.495	1.371	0.09
47	1.502 ± 0.009 370.13 ± 0.04	1.91	1.785	0.07
46	1.708 ± 0.003 375.9 ± 0.2	2.137	2.016	0.06
43	2.57 ± 0.03 395.3 ± 0.2	2.71	2.593	0.045
42	2.772 ± 0.001 401.85 ± 0.08	2.999	2.827	0.061
40	3.453 ± 0.002 415.4 ± 0.1	3.558	3.526	0.009
38	4.400 ± 0.001 430.7 ± 0.1	4.262	4.059	0.05
37	4.877 ± 0.002 438.9 ± 0.3	4.501	4.167	0.08
35	5.842 ± 0.001 455.1 ± 0.1	5.342	5.321	0.004
33	7.246 ± 0.001 471.3 ± 0.05	6.161	6.155	0.001
32	7.808 ± 0.003 478.3 ± 0.1	6.673	6.613	0.009
29	10.583 ± 0.003 506.3 ± 0.2	8.465	8.462	0.0003
27	12.567 ± 0.003 521.9 ± 0.1	9.816	9.174	0.07
26	13.656 ± 0.002 530.5 ± 0.1	10.669	10.065	0.06
24	16.319 ± 0.007 546.9 ± 0.4	12.177	12.080	0.008
22	19.225 ± 0.009 565.2 ± 0.4	13.92	13.919	0.0001*

Table 5.5: *Integrated band area of the experimental and simulated spectra. M refer to the band integrated area of "measurements", LMM refer to Line Mixing Model. In the first column we reported the altitude (z) which are referenced to the Venus's radius (∼6.052 km)*

5.3 Collision Induced Absorption

The carbon dioxide is a linear triatomic molecule that has 3x3-5=4 normal modes of vibration [9]. In the first mode the carbon nucleus is stationary while the two oxygen nuclei oscillate symmetrically. Because this symmetric motion does not generate a dipole moment, infrared transition to this state are forbidden. In the second and third modes the molecule bends in two, orthogonal planes. The second and third modes are, therefore, degenerate. The last mode has the carbon nucleus moving alternately toward one and then the other of the two oxygen nuclei.

The normal modes are conventionally labelled ν_1, ν_2 and ν_3, with ν_2 referring to the combination of the two degenerate bending modes. This is the behavior of the CO_2 at standard condition, but even when the pressure is only a few bar, we have observed the CO_2 Collisional Induced Absorption (CIA) forbidden bands for the symmetric $^{16}O^{12}C^{16}$O molecule. The interaction of the molecules with their neighbors induces indeed a dipole moment which yields to pressure-induced-absorption bands.

The $^{16}O^{12}C^{18}$O bands have been observed with coarse resolution by Eggers and Arends [62] from samples enriched in ^{18}O. Welsh, Crawford and Locke [63] and Sandiford [64] have observed the pressure induces bands in samples at high pressure and short paths for wich the intrinsic absorption was negligible. More recently, Mannik et al. [65] have observed an intrinsic-absorption component in natural CO_2 with no enriched isotopes that they scribe to the $^{16}O^{12}C^{16}$O molecules.

By employing our experimental set-up, we observed several absorption bands due to the CIA, in different spectral range as you can see in figure 5.16.

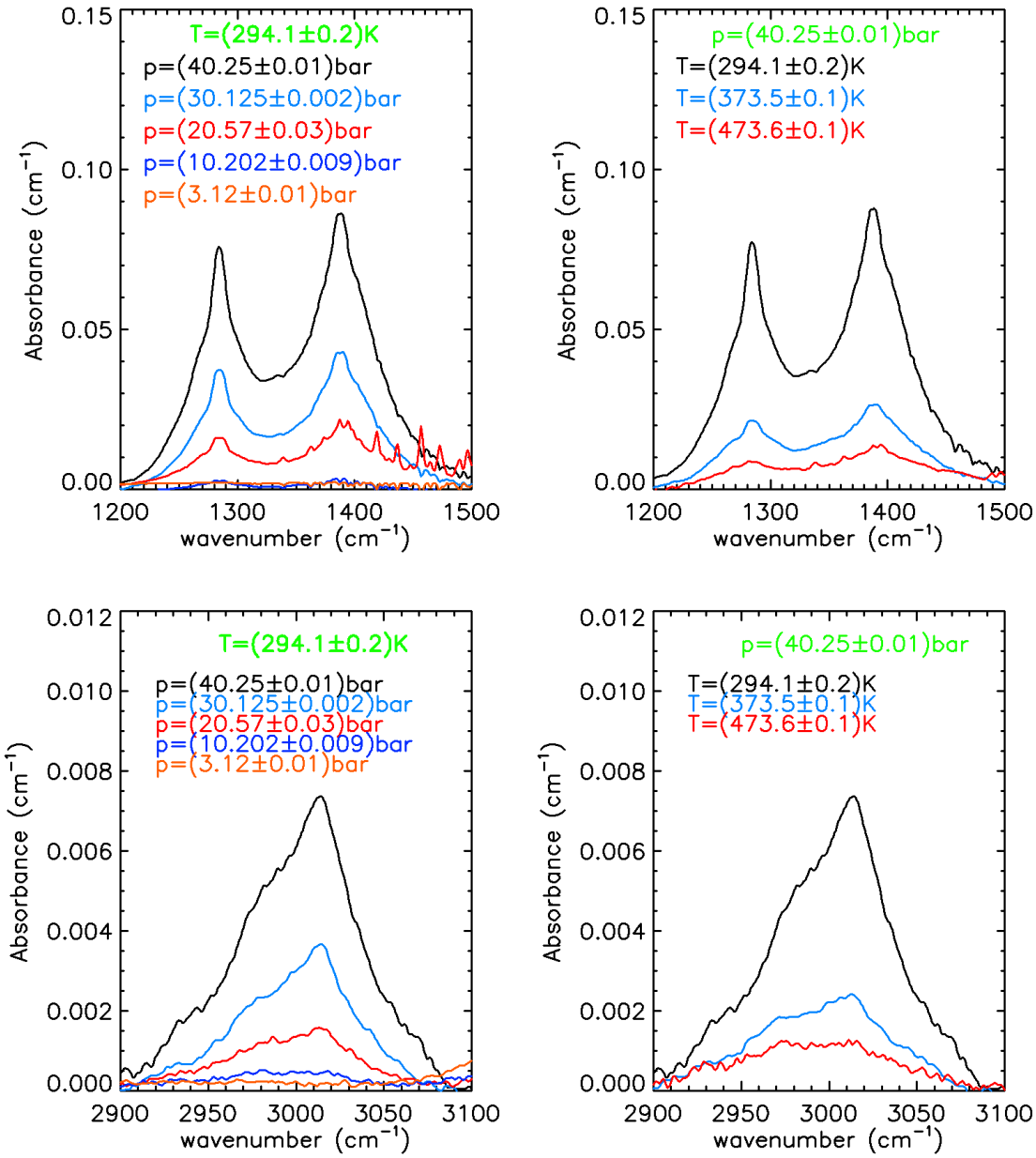

Figure 5.16: *Collision Induced Absorption (CIA) bands observed at room temperature and different pressures (top panels) and different temperatures (low panels) with $p \simeq 40$ bar*

The observed bands integrated intensities show a quadratic dependence versus density , as you can see in figure 5.17, in violation of the Beer's law [28]. The observed quadratic dependence suggest an absorption by pairs of molecules; Beer's law, au the contrary, attempts to describe absorption by individual molecules.

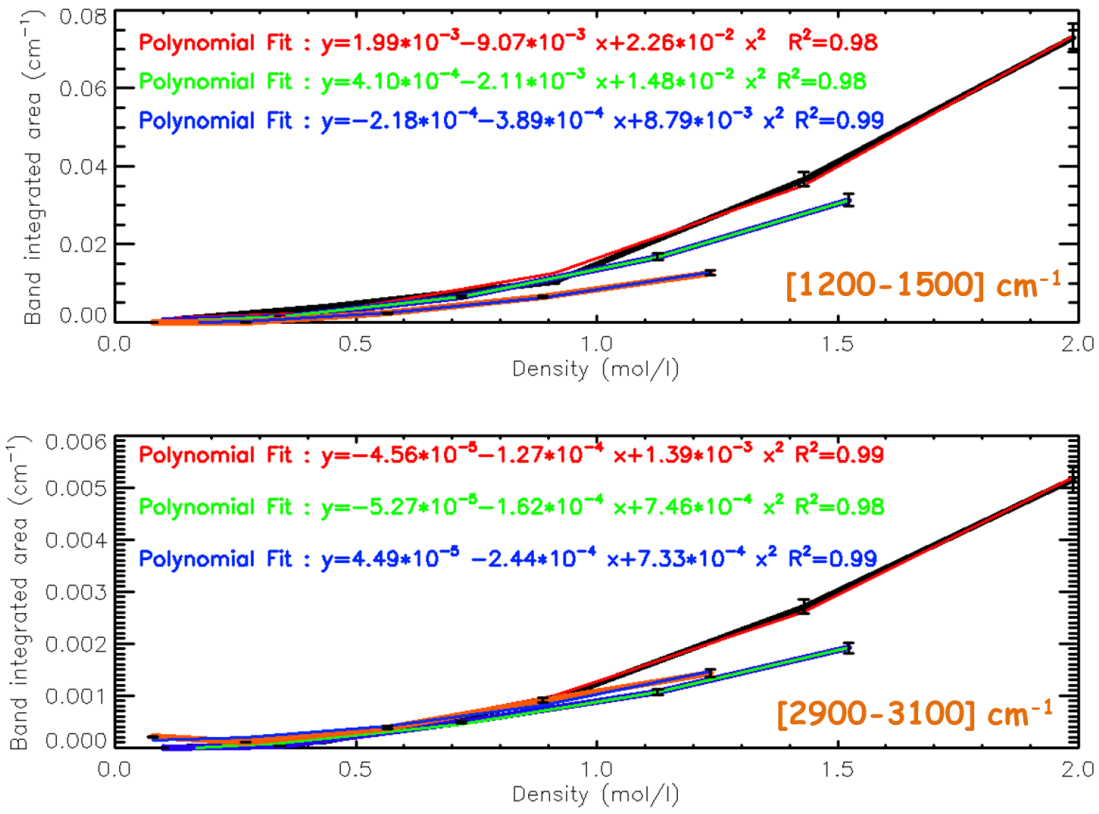

Figure 5.17: *The band integrated area vs density evaluated for the spectral range [1500-1200]cm^{-1} (left panels) and for [3100-2900] cm^{-1} (right panels). The red, green and blue curves correspond to the polynomial fit.*

According to [66], where an extensive study of the Collision Induced Absorption bands has been treated, we can confirm that the band observed in the spectral range [1400-1200] cm^{-1} is due to the strong Fermi-coupled doublet (ν_1, 2 ν_2). The spectrum consist of two bands, one at about 1282 cm^{-1} and the second one at about

1390 cm^{-1}. These bands represent the pronounced Q branches surrounded by P- and R-like branches. Interestingly, the peak intensities of R- exceed those of P branches. This result is comparable with that found in [67] by high-resolution CARS probings in free expanding jet. This work assigned definitely a peak at 1284.73 cm^{-1} to carbon dioxide dimer.

The peak intensity increases with the pressure, as shown in figure 5.16 (on left), and decrease with the temperature. This is probably due to the dissociation energy of dimers, determined in [68] as the thermally excited state-selected energy statistically averaged over an ensemble of quansidiatomic molecules at equilibrium. Under harmonic oscillator approximation, the effective dissociation energy is expressed by:

$$\langle D_0 \rangle = D_0 - 2T \frac{1 - \left[1 + \frac{D_0}{T} + \frac{1}{2}\left(\frac{D_0}{T}\right)^2\right] exp\left(\frac{-D_0}{T}\right)}{1 - \left(1 + \frac{D_0}{T}\right) exp\left(\frac{-D_0}{T}\right)} \tag{5.5}$$

where D_0 is expressed in K. You can note that the terminal value of the thermally averaged dissociation energy at T$\rightarrow \infty$ is equal to $D_0/3$. The intermolecular potential well depth for the $(CO_2)_2$ dimer is about 700K. Presupposing four intermolecular vibrations to have a mean frequency about ν=35 cm^{-1}, the zero point vibrational energy can be estimated to be of the order of 100K. Hence, the dissociation energy of $(CO_2)_2$ dimer is about D_0=600K.

It should be noted that the absorption by CO_2 is relatively weak (0.10 cm^{-1} or less at 40 bar, as shown in figure 5.16) throughout the 1100-1835 cm^{-1} region and has not been studied as in the other part of the electromagnetic spectrum. The CO_2 absorption is negligible in the earth's atmosphere except for very long optical paths, but plays an important role in the radiative transfer in atmospheres of planets such as Venus that contain vast amounts of CO_2 (about 96 %).

5.4 Study of the continuum

The interpretation of emission/absorption spectra from the Venus' atmosphere presents a challenge to the scientific community. Indeed, due to the high values of the pressure and CO_2 volume mixing ratio, the contributions of complex phenomena such as Collision-Induced Absorption, line mixing and far wings absorption, must be accurately taken into account. The cumulative set of this effects (known or unknown) is simply named *Continuum*. This consists of a set of very weak absorption line and in order to distinguish each contribution it's necessary to work at high densities with very long optical paths. Our experimental setup does not allow to reach large optical path, because the gas cell is only 2 cm long. To overcome this limitation, the Cavity Ring Down (CRD) spectroscopy can be used. A typically experimental setup is shown in figure 5.18.

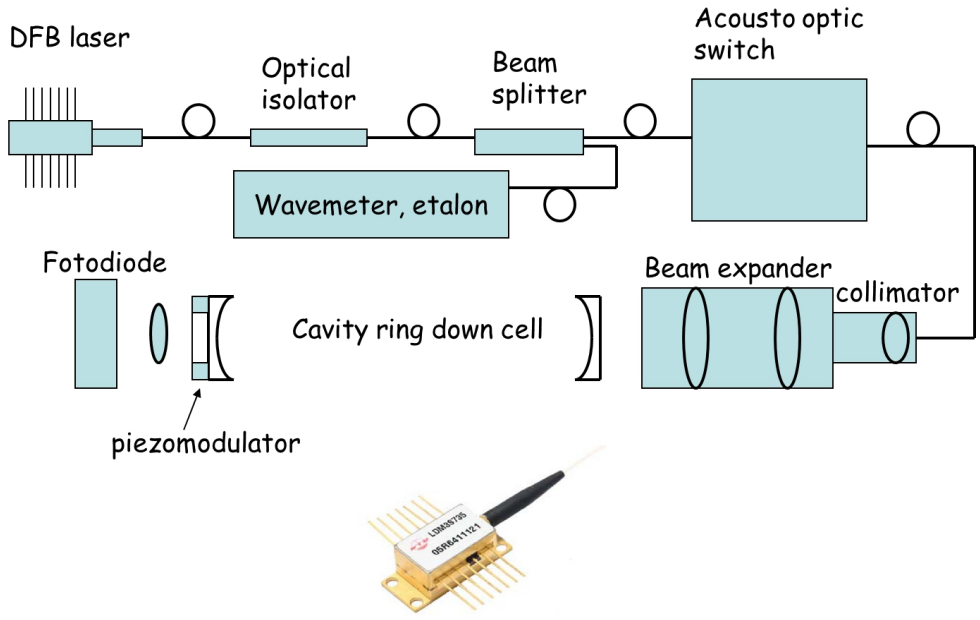

Figure 5.18: *Cavity Ring Down (CRD) experimental setup. This consist of a laser(DFB), optical components, a collimator, a resonant cavity and a fotodiode as detector.*

It's consists of a laser that is used to illuminate a stable optical cavity, formed by two highly reflecting plano-concave mirrors. The laser is used as a source, because is monochromatic, extremely bright and both spatially and temporally coherent. The fraction of light entering the cavity on one side 'rings' back and forth many times between the two mirrors. The time behavior of the light intensity inside the cavity I_{CRD}(t), can be monitored by the small fraction of light that is transmitted through the other mirror.

If the only loss factor in the cavity is the reflectivity loss of the mirrors, one can show that the light intensity inside the cavity decays exponentially in time with a decay constant τ, the *ring down time*, given by:

$$\tau = \frac{d}{c(|lnR|)}. \tag{5.6}$$

Here d is the optical path length between the mirrors, c is the speed of light and R is the reflectivity of the mirrors.

If there is additional loss inside the cavity due to the presence of absorber such as CO_2, the light intensity inside the cavity will still decay exponentially in time provided the absorption follows Beer's law. One can be shown that the product of the frequency dependent absorption cross-section with the number density $N_i(x)$ is commonly expressed as the absorption coefficient $k_i(\nu, \mathrm{x})$. For a detailed description refer to [69]. Thanks to this technique, we can analyze also the less abundant isotopic carbon dioxide species, temperature dependence of absorption and broadening parameters, as well as different phenomena such as Collision Induced Absorption.

Although this technique has many advantages, it also has many restrictions. One in particular is due to the narrow range in which lasers operate. In fact, although

tunable, this source may cover up to 100nm as a maximum. In order to characterize the optical properties of gases in a wide spectral range, several lasers are needed and are often very expensive. In addition to that, many cavities are also needed because, the mirrors used, cannot be adapted throughout in all spectral ranges of interest.

For the current study, we used a FT-IR to cover a wide spectral range in order to test the tools of simulation

Conclusions

In this thesis we presented a new experimental setup able to characterize the optical properties of gases at typically planetary conditions, in particular high pressure and high temperature. We prefixed two scientific objectives: to measure CO_2 absorption coefficients in order to expand the available spectroscopic databases to better match the broadening and line mixing effect; to update the commonly used tools of radiative transfer calculation in order to improve the accuracy of remote sensing data analysis. In light of the results presented in this work, many experimental data are now available obtained at real vertical venusian physical conditions, especially at low altitude, for a wide range of temperature, pressure and spectral domain (from 750 to 10000 cm^{-1}).

The comparison between measured and simulated data by using three different models (ARS,Solution, LMM), leads us to conclude that LMM reproduces the laboratory spectra excellently, for all pressures and temperatures investigated. Contrary to the widely used Lorentz shape, the LMM leads to have a good agreement with the experimental data in the central and near wing regions of the vibrational bands.

Experimental data has been to used to test the LMM and calculate the χ form factor and B coefficients in order to better reproduced the line shape of the CO_2 at high pressure and high temperature. Models that do not take into account the line

mixing and far wings effects have shown to be inadequate to reproduce satisfactory the carbon dioxide absorption in the deep Venusian atmosphere below the clouds. For the far wing region where these two approaches fail, correction factors have been determined to model the spectral shape. Sets of temperature dependent factors have been constructed for the ν_2, ν_3 and $\nu_1+\nu_3$ bands wing regions. Comparison between spectra calculated using these data and measured values show good agreement for a wide range of temperature. For the ν_2 band region, the LMM is sufficient to correctly describe the band, from its center to the far wing. For the ν_3 and $\nu_1 + \nu_3$ bands, the center and near wing region (from the band center to about 50 cm^{-1}) should be calculated by the impact LM model and the far wing by applying the correction factors.

Concerning Collision-Induced Absorption (CIA), it's found to be proportional to the square of the density, decreases with temperature, consistently with the collisional nature of this phenomenon.

More work has to be exploited in this direction, especially to include this effect in the radiative transfer calculation.

Acknowledgements

First of all, I would like to thank my super-visor Giuseppe Piccioni. He is and will be a reference for me, teaching me so many things: technically, scientifically and human. It's a great pleasure work with him.

I would like to thank Marcel Snels, Davide Grassi and Nikolay which have opened me a new world thanks to their outstanding knowledge in the field of experimental techniques, spectroscopy, planetary sciences and so on.

I would like to thank Pasquale Palumbo, the tutor of this thesis, who helped me and supported during this three years.

I would also like to thank the "Venusian" Team in Rome: Alessandra (much more than a colleague) and Romolo (the man of the "Night of the research") who have supported me from the very beginning.

A particular acknowledgement to two colleagues, Sasha and Ha, whom hosted me in your institute , working together for a week, thanks this collaboration, I have the opportunity to write a chapter of this thesis.

I would like to thank to Agenzia Spaziale Italiana (Italian Space Agency) to having supported my work by an ASI grant (nr. 513/07).

A special thanks to " Fantastic 3" (without me) through which I spent some wonderful moments at work an during our numerous "little recall". I'm wating for a

new incredible new adventure of. We should add to this group the Blond's family.
I had also the opportunity to meet a new friends, the Plab's guys: Eleonora, Sergio, Frankie, Tatiana e Cristian.
I can not forget those who sponsored me: a special thanks to my grandmother, my aunt, my uncle and my cousins.
I want to finish with the most important acknowledgement. I want to express all my love and gratitude to my fantastic family (my mother, my father and my brother Michele) that I have always taken with me, giving me support and help in every single step of this long route.

Bibliography

[1] Rothman LS et al. *The HITRAN 2008 molecular spectroscopic database. Journal of Quantitative Spectroscopy and Radiative Transfer , 110:533-72*, 2009.

[2] Rothmana LS; Gordon IE et all. *HITEMP, the high temperature molecular spectroscopic database. Journal of Quantitative Spectroscopy and Radiative Transfer, 111: 2139-50.*, 2010.

[3] Tashkun S.A.; Perevalov V.I. *Carbon Dioxide Spectroscopic Databank. NATO Security through Science Series,161-169*, 2006.

[4] Piccioni G. et al. *VIRTIS: the Visible and Infrared Thermal Imaging Spectrometer. Eur. Space Agency Spec. Publ., ESA SP-1295*, 2007.

[5] Marcq E.; Bézard B. et al. *A latitudinal survey of CO, OCS, H_2O and SO2 in the lower atmosphere of Venus: Spectroscopic studies using VIRTIS-H. . (J Geophys Res ; 113: E00B07*, 2008.

[6] Predoi-Cross A; McKellar ARW et all. *Temperature dependences for air-broadened Lorentz half-width and pressure shift coefficients in the 30013←00001 and 30012←00001 bands of CO_2 near 1600 nm. Can J Phys, 87: 517-35*, 2009.

[7] Winters BH; Silverman S; Benedict WS. *Line shape in the beyond the band head*

of the 4.3 μm band of CO_2. Journal of Quantative Spectroscopy and Radiative Transfer, 4: 527-37, 1964.

[8] John Houghton. *The physics of Atmospheres. Cambridge University Press third edition*, 2002.

[9] Hanel R.A; Jannings D.E; Conrath B.J.; Samuelson R.E. *Exploration of the Solar System by infrared remote sensing. Cambridge University Press*, 1992.

[10] J. Michael Hollas. *High Resolution Spectroscopy. John Wiley And Sons Second edition*, 1998.

[11] Piccioni G; Amici S et al. *Efficiency Measurements of the VIRTIS-M Grating. Planet Space Sci 48 (5), 411-417*, 2000.

[12] Taylor F.W et al. *Venus before Venus Express. Planetary and Space Science Vol 54, Issues 13-14, Pp 1249-1262*, 2006.

[13] Drossart P.; Piccioni G. et al. *Scientific goals for the observation of Venus by VIRTIS on ESA/Venus express mission . (Planetary and Space Science, Vol 55, Issue 12, p. 1653-1672*, 2007.

[14] Collard AD; Taylor FW; Calcutt SB et al. *Latitudinal Distribution of Carbon Monoxide in the Deep Atmosphere of Venus. Planet. Space Sci. 41, 487-494*, 1993.

[15] Drossart P; Bezard B; Encrenanz TH et al. *Search of Spatial Variations of the H_2O Abundance in the Lower Atmosphere of Venus from NIMS Galileo. Planet. Space Sci. 41, 495-504*, 1993.

[16] Irwin P. G. J.; de Kok R. et al. *Spatial variability of carbon monoxide in Venus' mesosphere from Venus Express/Visible and Infrared Thermal Imaging Spectrometer measurements . JOURNAL OF GEOPHYSICAL RESEARCH, VOL. 113, E00B01, 11 PP.*, 2008.

[17] Migliorini A.; Altieri F. et al. *Oxygen airglow emission on Venus and Mars as seen by VIRTIS/VEX and OMEGA/MEX imaging spectrometers. Planetary and Space Science, Volume 59, Issue 10, p. 981-987*, 2011.

[18] Moissl R.; Khatuntsev I. et al. *Venus cloud top winds from tracking UV features in Venus Monitoring Camera images. JOURNAL OF GEOPHYSICAL RESEARCH, VOL. 114, E00B31, 13 PP.*, 2009.

[19] Widemanna T.;Lelloucha E. et al. *Venus Doppler winds at cloud tops observed with ESPaDOnS at CFHT. Planetary and Space Science Volume 56, Issue 10, Pages 1320-1334*, 2008.

[20] Roos M; Drossart P; Encrenanz TH et al. *The Upper Clouds of Venus: Determination of the Scale Height from NIMS-Galileo Infrared Data. Planet. Space Sci. 41, 505-514*, 1993.

[21] Roldan C; Lòpez-Valverde MA; Encrenanz TH et al. *Non-LTE Infrared Emissions of CO_2 in the Atmosphere of Venus. Icarus, 147, 11-25*, 2000.

[22] López-Valverdea M.A.;López-Puertasa M. et al. *Modeling the atmospheric limb emission of CO_2 at 4.3 μm in the terrestrial planets. Planetary and Space Science Volume 59, Issue 10,Pages 988-998*, 2011.

[23] Artur J;Lognonné P and Ballac E. *Normal Modes Modeling of Post-Seismic Ionospheric Oscillations. Geophys. Res. Letters, 28, 697*, 2000.

[24] Smrekar S.E.;Stofan E.R. et al. *Recent Hotspot Volcanism on Venus from VIRTIS Emissivity Data. Science Vol.328, 5978, pp.605-608*, 2010.

[25] Mills F.P.; Esposito L.W. *Atmospheric Composition, Chemistry, and Clouds. Mendeley (Exploring Venus as Terrestrial Planet), pp.73-100*, 2007.

[26] Houghton J.T; Taylor F.W. and Rodgers C.D. *One Remote Sensing of Atmospheres. Canbridge University Press*, 1984.

[27] Seiff A.; In Bougher S.W; Hunten D.M and Phillips R.J editors. *Thermal Structure of the Atmosphere Of Venus. Venus Space Science Series, pp 215-279. University of Arizona Press*, 1983.

[28] Lothar Frommhold. *Collision-induced Absorption in Gases. Cambridge monographs on atomic, molecular and chemical Physics*, 1993.

[29] Bruker Optics. *VERTEX 80. User Manual*, 2006.

[30] Harris F.J. *On the use of windows for harmonic analysis with the Discrete Fourier Transform . Proceedings of the IEEE, vol 66 pp 51-83*, 1978.

[31] CHASE D.B. *Phase Correction in FT-IR . Applied Spectroscopy, Vol 36 number 3*, 1982.

[32] AABSPEC. *High Temperature and High Pressure Advanced Gas Cell. User Manual*, 2004.

[33] AABSPEC. *DTC-1 and DTC-2 Digital Temperature Controllers. User Manual*, 2004.

[34] Ignatiev N. et al. *Planetary Fourier spectrometer data analysis: Fast radiative transfer models. Planetary and Space Science 53, 1035-1042)*, 2005.

[35] Afanasenko T. S.; Rodin A. V. *The Effect of Collisional Line Broadening on the Spectrum and Fluxes of Thermal Radiation in the Lower Atmosphere of Venus. Solar System Research, vol 39, Issue 3, pp.187-189.*, 2005.

[36] Afanasenko T. S.; Rodin A. V. *Interference of spectral lines in thermal radiation from the lower atmosphere of Venus. Astronomy Letters, vol 33, Issue 3, pp.203-210.*, 2007.

[37] Burch D.F; Gryvnak D.A. *Absorption of infrared radiant energy by CO_2 and H_2O. Absorption by CO_2 between 1100 and 1835 cm^{-1} (9.1-5.5 μm). J.Opt.Soc.Amer, Vol. 61, nr.4., p. 499-503.*, 1971.

[38] Nesmelova L.I.; Rodimova O. B. *Spectral behavior of the absorption coefficient in the 4.3-micron CO_2 band over a wide range of temperatures and pressures. Optika Atmosfery i Okeana (ISSN 0869-5695), Vol. 5, nr. 9, p. 939-946.*, 1992.

[39] Lothar Frommhold. *Collision Induced Absorption in Gases. Cambridge Monographs on atomic, molecular amd chemical physics*, 1993.

[40] Niro F.; Boulet C.; Hartmann JM. *Spectra calulations in central and wing regions of CO_2 IR bands between 10 and 20 μm I:model and laboratiry measurements. Journal of Quantitative Spectroscopy and Radiative Transfer, 88, pp.483-498*, 2004.

[41] Hartmann JM; Boulet C; Robert D. *Collisional Effects on Molecular Spectra. Laboratory experiments and models, consequences for applications. Amsterdam: Elsevier*, 2008.

[42] Rodrigues R; Jucks KW; Lacome N et al. *Model, software and database for computation of line-mixing effects in infrared Q branches of atmospheric CO_2. I. Symmetric isotopomers. Journal of Quantitative Spectroscopy and Radiative Transfer, 61:153-84*, 1999.

[43] DePristo AE; Augustin ST; Ramaswamy R; Rabitz H. *Quantum number and energy scaling for non reactive collisions. J Chem Phys, 71: 850-65*, 1979.

[44] Edmonds; A. R. *Angular momentum in Quantum Mechanics. Princeton Univ. Press., Princeton , NJ edited by R. Hofstadter*, 1974.

[45] Lamouroux J; Tran H; Laraia AL et all. *Updated database plus software for line-mixing in CO_2 infrared spectra and their test using laboratory spectra in the 1.5-2.3 μm region. Journal of Quantitative Spectroscopy and Radiative Transfer 111: 2321-31*, 2010.

[46] Rodrigues R; Boulet C; Bonamy L; Hartmann JM. *Temperature, pressure and perturber denpendencies of line-mixing effects in CO_2 infrared spectra. Rotational angular momentum relaxation and spectral shift in $\Sigma \leftarrow \Sigma$ bands. J Chem Phys 109: 3037-47*, 1998.

[47] Predoi-Cross A; Liu W; Murphy R; Povey C et all. *Measurements and computations for temperature dependences of self-broadened carbon dioxide transitions in the 30012←00001 and 30012←00001 bands. Journal of Quantitative Spectroscopy and Radiative Transfer 111: 1065-79*, 2010.

[48] Predoi-Cross A; Unni AV; Liu W; Schofield I et all. *Line shape parameters measurements and computations for self-broadened carbon dioxide transitions in the*

30012← 00001 and 30013← 00001 bands, line mixing, and speed dependence. J Mol Spectrosc, 245: 34-51, 2007.

[49] Predoi-Cross A; Unni AV; Liu W; Schofield I et all. *A simple model for the collisional spectral shift of air-broadened CO_2 lines. Journal of Quantitative Spectroscopy and Radiative Transfer 110: 2019-26.*, 2009.

[50] Toth RA; Brown LR; Miller CE; Devi VM; Benner DC. *Self-broadened widths and shifts of $^{12}C^{16}O_2$: 4750-7000 cm^{-1} . J Mol Spectrosc 239: 243-71*, 2006.

[51] Thibault F; Boissoles J; Le Doucen R; Bouanich JP; Arcas P; Boulet C. *Pressure induced shifts of CO_2 lines. Measurements in the 0000-0003 band and theoretical analysis. . J Chem Phys, 96: 4945-53.*, 1992.

[52] Moroz V.I.;Zasova L.V. *VIRA-2: a review of inputs for updating the Venus international Reference Atmosphere. Advances in Space Research, vol. 19, Issue 8, pp 1191-1201*, 1997.

[53] Weast R.C. *Handbook of Chemistry and Physics (53rd Edn.). Cleveland-Chemical Rubber Co.*, 1972.

[54] Hirschfelder Joseph O.; Curtiss Charles F et al. Molecular Theory of Gases and Liquids (Corrected printing ed.). *Molecular Theory of Gases and Liquids (Corrected printing ed.). John Wiley and Sons, Inc.*, 1967.

[55] Le Doucen R; Cousin C et al. *Temperature dependence of the absorption beyond the 4.3-μm band head of CO_2. 1: Pure CO_2case. Appl Opt 24:897-905*, 1985.

[56] Hartmann JM; Boulet C. *Line-mixing and finite duration of collision effects*

in effects in pure CO_2 infrared spectra: Fitting and scaling analysis. J Chem Phys, 94: 6406-19., 1991.

[57] Boulet C; Boissoles J; Robert D. *Collisionally induced population transfer effect in infrared absorption spectra. I. A line-by-line coupling theory from resonances to the far wings. . J Chem Phys, 89: 625-34*, 1988.

[58] Perrin MY; Hartmann JM. *Temperature dependence measurements and modelling of absorption by CO_2-N_2 mixtures in the far line-wings of the 4.3 μm CO_2 band. . JQRST, 42: 311-17*, 1989.

[59] Burch DE;Gryvnak DA et al. *Absorption of infrared radiant energy by CO2 and H2O. IV. Shapes of collision-broadened CO_2 lines. J Opt Soc Am, 59:267-80*, 1969.

[60] Menoux V; Le Doucen R; Boulet C. *Line shape in the low frequency wing of selfbroadened CO_2 lines. Appl Opt 26:554-61*, 1987.

[61] Tonkov MV; Filippov NN; Bertsev VV et al. *Measurements and empirical modelling of pure CO_2 absorption in the 2.3 μm region at room temperature: far wings, allowed and collision-induced bands. Appl Opt 35:4863-70*, 1996.

[62] Eggers F.; Arends Jr and C.B. *Absorption of Infrared Radiant Energy by CO_2 and H_2O, V. Absorption by CO_2 between 1100 and 1835 cm^{-1} (9.1-5.5 μm). J. Cheme. Phys., 27, 1405*, 1967.

[63] Crawford M.F. Welsh H.L. *Theory of induced infra-red absorption . Phys. Rev. 76,580*, 1949.

[64] Sandiford F.J. . *Thesis, University of Toronto*, 1952.

[65] Mannik L; McKellar A.R.W. et al. *An Infrared Spectrum of CO_2 Dimers in the "Locked" Configuration . Can. J. Phys. 48,95*, 1970.

[66] Baranov Y.I and Vigasin A.A. *Collision-Induced Absorption by CO_2 in the Region of ν_1, $2\nu_2$. Journal of Molecular Spectroscopy 193, 319-325*, 1999.

[67] Vigasin A.A.; A.A. Ilyukhin et al. *Intensity and Bandshapes of Collision-Induced Absorption by CO_2 in the Region of the Fermi Doublet. Journal of Molecular Spectroscopy 200, 89-95*, 1996.

[68] Vigasin A.A. *Thermally averaged effective dissociation energy of dimers. Chemical Physics Letters 242, 33-38*, 1995.

[69] Giel B.; Ruby P. et al. *Cavity Ring-Down Spectroscopy: Technique and Applications. Int. Reviews in Physical Chemistry, Vol. 19, No.4, pp. 565-607*, 2000.

Bibliography

List of Figures

List of Tables